國 立 交 通 大 學

機械工程學系

碩士論文

熱風爐之燃燒、流場與熱傳數值模擬分析

The Numerical Simulation Analyses of Combustion, Flow Field and Heat Transfer for Hot-Blast Stove

研究生：楊宏一

指導教授：陳俊勳　教授

中 華 民 國 九 十 七 年 六 月

熱風爐之燃燒、流場與熱傳數值模擬分析

The Numerical Simulation Analyses of Combustion, Flow Field and Heat Transfer for Hot-Blast Stove

研究生　：楊宏一　　Student：Hung-Yi Yang

指導教授：陳俊勳　　Advisor：Chiun-Hsun Chen

國立交通大學

機械工程學系

碩士論文

A Thesis

Submitted to Department of Mechanical Engineering

College of Engineering

National Chiao Tung University

In Partial Fulfiillment of the Requirements

For the Degree of

Master of Science

In Mechanical Engineering

June 2008

Hsinchu, Taiwan, Republic of China

中華民國九十七年六月

熱風爐之燃燒、流場與熱傳數值模擬分析

學生:楊宏一　　指導教授:陳俊勳

國立交通大學機械工程學系

摘要

本研究係以商業套裝模擬軟體 FLUENT 來模擬熱風爐操作之一系列運作過程，其中包括燃燒、切換和送風三個過程。燃燒部分使用 finite-rate 之燃燒模組，蓄熱磚部分使用多孔性介質來做近似。數值模擬所得之計算結果著重於廢氣出口與熱風出口溫度值。在參考案例中，廢氣出口與熱風出口溫度隨時間變化之趨勢在模擬與實驗中皆相同，且廢氣出口與熱風出口溫度之模擬與實驗值的均方根誤差(RMSE)分別為 2.0 %及 1.2 %。

針對燃氣熱值、燃氣流量以及過剩空氣比等參數對於熱風爐操作的影響做一系列之研究，結果顯示可選擇如下方案以節省操作成本，並可穩定進行熱風爐之運作: (1) 減少混合燃氣中 COG 之使用量 30 %，過剩空氣比維持 1.03 (2) 減少混合燃氣總流量 5 %，過剩空氣比維持 1.03。

關鍵字: 熱風爐; 燃燒過程; 送風過程; 蓄熱磚

The Numerical Simulation Analyses of Combustion, Flow Field and Heat Transfer for Hot-Blast Stove

Student: Hung-Yi Yang Advisor: Prof. Chiun-Hsun Chen

Institute of Mechanical Engineering

National Chiao Tung University

ABSTRACT

This study applies a commercial package software FLUENT to simulate a series of hot-blast stove's operation processes. The operation process consists of on-gas, stove-change and on-blast cycles. The finite-rate combustion model and porous media approximation are adopted here. The simulation results focus on the waste gas and hot blast temperatures. In the reference case, the trends of experimental and simulated temperatures of waste gas and hot blast varying with time are the same, and the RMSE of waste gas and hot blast temperature between simulation and experiment are 2.0 and 1.2 % respectively.

From a series of parametric studies consisting of the heating value and volume flow rate of mixed fuel gas and the excess air ratio, the results indicated that it can use the following cases to reduce the cost of hot-blast stove's operation: (1) The quantity of COG in mixed fuel gas decreases 30 %, and the excess air ratio maintains 1.03. (2) The volume flow rate of mixed fuel gas decreases 5 %, and the excess air ratio maintains 1.03.

Keywords: hot-blast stove; on-gas cycle; on-blast cycle; checker brick

誌謝

一晃眼，兩年的碩班生活就要過去了，在這兩年裡，承蒙吾師 陳俊勳教授的諄諄教誨與耳提面命，使學生在學問及做人處事上，都有了成長，在此要對老師獻上為限的感激與敬意。此外，還要感謝口試委員的指正與建議，使我獲益良多。

在兩年的研究生活中，感謝彥成、家維、榮貴及遠達學長在軟體使用上的研究與指導。 文耀、成陽、維義、振忠、俊翔、塘原及耀文學長在碩班生活上也提供了許多寶貴的意見，讓我受益匪淺。 同學 彥佐、靖山、昇宏及仁浩，感謝你們這兩年來在生活及課業上的扶持與幫忙，讓我的研究生活更加順遂。 學弟金輝、智欽、致瑋、振稼、長青及育祈，感謝你們適時在生活中搞笑，讓我的研究生活增添了不少的樂趣。感謝惠文總是在我慌亂無助的時刻，幫我加油與打氣，讓我能夠一路堅持下去把論文完成。

謝謝姐姐 如容與妹妹 婷婷，總是適時地給我一些生活上的建議與關心，讓我感受到家人的溫暖。最後，我要感謝我最愛的爸爸 尚義與媽媽 素美，謝謝您們時時刻刻對我的感懷與照顧，讓我能夠無後顧之憂地在新竹求學，謝謝您們。

CONTENTS

LIST OF TABLES

LIST OF FIGURES

NOMENCLATURE

C_p	Heat capacity at constant pressure
$D_{i,j}, D$	Mass diffusion coefficient
E	Total energy, activation energy
$\vec{F}$	Force vector
$\vec{g}$	Gravitational acceleration
H	Total enthalpy
h	Species enthalpy
J	Diffusion flux
k	Thermal conductivity
M_w	Molecular weight
p	Pressure
Pr	Prandtl number
S	Total entropy
Sc	Schmidt number
T	Temperature
u, v, w	Velocity components in the (x, y, z) system of coordinates
Y	Mass fraction

Greek Symbols

ρ	Density
$\bar{\bar{\tau}}$	Stress Tensor
τ	Shear stress
β	Coefficient of thermal expansion
γ	Porosity

δ	Delta function
ε	Turbulent dissipation rate
η', η''	Rate exponents for reactants, products
μ	Dynamic viscosity
ν	Kinetic viscosity
ν', ν''	Stoichiometric coefficients for reactants, products

CHAPTER 1
INTRODUCTION

1.1 Background

The modern steel mill is mainly comprised of charging equipment, blast furnace, hot-blast stove, wind-blowing equipment, dust-removing equipment, and so on. The equipments of iron-smelting process include cast house, cold blast system, hot blast system, blast furnace gas cleaning system, cooling water system, blast furnace instrumentation control and measuring equipment, auxiliary fuel injection system, blast furnace pulverized coal injection system, torpedo car, pig casting machine, dust-collecting equipments of stock house and cast house, stove stone granulation equipment, etc.

Among them, the function of hot blast system is to provide stable hot blast continuously to blast furnace, therefore, a blast furnace system typically is designed to operate with three or four hot-blast stoves that can alternatively produce hot blast. Each of these stoves go through heating and cooling cycles periodically, called on-gas and on-blast cycles, respectively. The hot-blast stove is filled with thermal regenerators, mainly comprised of refractory, used to provide hot blast to the blast furnace. Under four stoves lap parallel operations, the hot blast average temperature shall be 1,200 ℃ at a blast wind volume of 4,500 Nm^3/min for a continuous period of two days. The detailed operation process of hot-blast stove can be seen in Fig. 1-1. The hot-blast stove is heated by

the combustion of mixed gaseous fuels in the combustion chamber during the on-gas cycle. The combustion products, or waste gases, enter the dome at the top of hot-blast stove and then descend down to go through the beehive regenerative bricks, referred as the checker bricks, and transfer energy to these bricks simultaneously. Hot blast is produced during the on-blast cycle. The cold blast air enters the bottom of hot-blast stove, and is heated as it passes upward through the checker bricks into the dome. After that, the cold blast proceeds into the combustion chamber before it exhausts from the hot-blast stove through the hot blast valve. After leaving the hot-blast stove, the hot blast will mix with the cold blast to achieve the required hot blast temperature for the blast furnace.

The main gaseous fuels used in hot-blast stove are the carbon monoxide and hydrogen, which are contained in the gas coming from the blast furnace (BFG). In order to achieve the required hot blast temperature, the mixed gaseous fuel is typically enriched by the fuel gas with a higher net calorific value, such as coke oven gas (COG) or natural gas. Coke oven gas enrichment is used in No. 2 blast furnace of hot-blast stoves in the China Steel Cooperation. Because COG is more valuable than BFG, one of the keys to reduce the operating cost of hot-blast stove is to minimize the usage of coke oven gas.

From the brief introduction above, it can be known that the main function of hot-blast stove is to provide stable hot blast, served as a heat source for blast furnace continuously in the iron-smelting process. Therefore, the better efficiency of hot blast formation is, the better overall efficiency of iron-smelting process is. The main goal of this study is to investigate the related combustion process with chemical reaction of

mixed gaseous fuel of BFG and COG, and attempt to obtain the best proportion between BFG and COG that can generate the highest energy for the blast furnace.

1.2 Literature Review

For the conventional annular ceramic burner, the flame length is so long that makes part of the gas to be burnt in the upper part of the checker in stove and results in damage of refractory materials. By using computer simulation to analyze the turbulent diffusion flame in the combustion chamber, it is expected that some suitable results can be achieved via a parametric study. The combustion process of the blunt burner was simulated by Zhang et al. [1]. The calculated results showed that the design of the blunt burner improves the mixing of the gas and air significantly and shortens the length of the flame to achieve the purpose of optimizing burner design.

Chen et al. [2] built a combustion model and simulated the burning process for a hot-blast stove with ceramic-grid burner. The result showed that the flame length in the ceramic-grid burner reaches the basic requirement of flame length in the hot-blast stove: 6~8 times the length of the diameter of combustion chamber. On the base of simulation, it has been testified by prototype burner and shown that the burner indeed has excellent combustion characteristics.

Kenneth et al. [3] established a detailed heat transfer model for model-based control of the hot-blast stoves. They performed the analysis by considering the variations in the physical and operating properties,

radiative heat transfer, radial and axial conduction in the checker bricks. The assumptions adopted here are that the cold blast and waste gases are treated as ideal gases, and there are no radial variation of the gas temperature and no axial variation of the heat conduction. The heat capacity and thermal conductivity for the checker bricks are specified as polynomial functions of temperature by the hot-blast stove manufacturer. Heat losses to the environment are neglected. The result of this study is a stove model capable of predicting accurately the temperature of the stove during the thermal regenerative cycles.

In the recovery combustion systems used in the steel industry, energy is provided by burning residual gases of blast furnace and coke oven. To help understand combustion of the particular type of fuels, a numerical study was conducted by Olivier et al. [4], which the major chemical properties of steel gas flames were collected. From the studies, some combustion characteristics for BFG and COG could be obtained. The high equilibrium temperature is occurred in the case of high proportion of COG in the mixture. It is of the order of 2200 K. With BFG, lower temperature levels found are of the order of 1500 K. The temperature is thus a direct function of BFG fraction in the fuel.

Zhu et al. [5] presented three kinds of method to improve the hot-blast stove's theoretical combustion temperature on the basis of quantitative analysis. These methods are: (1) Preheating of combustion air and fuel gas; (2) Enriching blast furnace gas with coke oven gas; (3) Reducing moisture of fuel gas. These provide the basis for optimal combustion techniques of hot-blast stoves in a certain iron-making plant.

Zhang et al. [6] conducted the numerical simulations of gas

combustion and flow in Kalugin hot-blast stove by using CFD software, and the distributions of pressure, temperature, gas velocity and concentration of CO at the exit of the combustion chamber are obtained. The thermal test is also conducted, including tests of temperature, pressure, concentration of CO at the exit of combustion chamber. The result showed that a low gas temperature occurs at the top of the combustion chamber and the complete combustion has been achieved.

In the metallurgical plant, gases are available from the coke production (COG) and the basic oxygen furnace (BOF) process. These two gases are rich of species like CO, H_2 and CH_4. Andahazy et al. [7] conducted a numerical simulation, and the result showed that the earlier ignition of the COG/BOF gas mixture in comparison to the COG can be ascribed to a higher excess air ratio, in spite of the better ignition propensity of COG. The higher net calorific value of COG results in the higher combustion temperatures, implicating a higher thermal strain on the tuyere. The higher gas velocity is resulted from the higher mean temperature. In addition, the greater amounts of CO and H_2 in the raceway are resulted from the COG combustion.

Ellul et al. [8] numerically investigated that the combustion characteristics and pollutant formation from BFG and COG diffusion flames with highly preheated air. The results showed that the maximum flame temperature obtained for COG is 2472 K whereas 1820 K for BFG. COG is a hydrocarbon gas with a high content of hydrogen, which has a very fast diffusion rate when ignited. Hence, the reaction rate is catalyzed with a very rapid O_2 consumption rate and high flame temperatures at high flame temperature conditions. This can ultimately dictate the

extinction limits and the mode of ignition to be used in practical high temperature regenerative burners.

Sun et al. [9] presented a method using Case-Based Reasoning as an effective estimating tool and based on the statistical data (not real-time data) during the on-gas cycle of hot-blast stove. Case-based reasoning (CBR) is a method that compares the present problem with previous ones and applies the problem solution of the past to the present one. In other words, the problem solving technique that was used in the past can be reused and applied to the present problem. For this reason, many researchers have found CBR to be a good alternative method for solving problems, such as knowledge acquisition since CBR method suggests automatic learning through reuse in the process of solving problems.

Case-based reasoning has been used to solve problems in diverse areas including decision support, help desk support, product cataloguing and maintenance support, etc. A novel CBR based real time controller was proposed and named CBRTC (Case-Based Real-Time Controller) by Sun et al. [10]. CBRTC may be looked as a kind of direct expert controller, but it applies case-based rather than rule-based reasoning methodology to make control decisions. A CBRTC is defined as a real-time controller, which deploys case-based reasoning methodology for making its control decisions. The CBRTC's architecture is very similar to a direct expert controller. The main difference between them only lies in the correspondent reasoning method. A CBRTC's control decision is made on the basis of case-based reasoning, yet an expert controller's decision is reasoned out based on ruled-based reasoning. CBRTC has been put into operation for combustion control of hot-blast

stoves in some in-situ applications. It is shown with the applications that CBRTC may be a powerful tool for dealing with the control problems of complicated industrial processes.

Liu and Xie [11] conducted a working process simulation of PM engine using a single-zone combustion model. Porous medium was installed into combustion chamber as the heat recuperator. An energy equation that incorporated a heat transfer model of porous medium was developed based on the first law of thermodynamics. Influences of operating parameters, such as compression ratio, equivalence ratio, temperature and volumetric heat transfer coefficient of the porous medium, on combustion process of the PM engine were analyzed. Comparison between PM and convectional engines showed that PM can decrease the variation of in-cylinder temperature and pressure, and is favorable to gas mixture ignition and NO_x reduction.

Zhao and Xie [12] conducted a numerical study on the combustion process of a porous medium internal combustion engine. Combustion and working processes of the PM engine with natural gas as fuel were simulated by an improved CFD software KIVA-3V. The effects of initial temperature and structure characteristics of the porous medium on the performance of the PM engine were discussed. Computational results showed that the initial temperature of PM is the important factor in determining the compressed mixture ignitability at a specified compression ratio. The structure characteristics of the PM can directly affect the convective heat transfer between the gas and solid as well as the dispersion effect of the PM, resulting in substantial impact on the in-cylinder gas temperature distribution and the average temperature of

the porous solid phase.

Wang and Sun [13] investigated gas combustion process in an inverting porous medium installed in combustion chamber. One dimension numerical model for the premixed gas combustion in inert porous media was developed based on the hypothesis of local thermal non-equilibrium. The influences of low velocity, equivalent ratio and absorb coefficient of the porous media on flame peak temperature were investigated. The results showed that the existence of the porous media improves heat transfer in the chamber, enhances preheating of fresh coming gas mixture, and increases the efficiency of combustion chamber.

Fu et al. [14] investigated forced convection heat transfer of a porous medium in a laminar channel flow numerically. The porous medium with random porosities was used to enhance heat transfer, and the random porosities were derived by the Kinderman-Ramage procedure. The results showed that when the mean porosity is larger than 0.5, the average Nusselt numbers are enhanced and better than those in solid block case. Therefore, a porous medium with larger porosity and proper bead diameter could provide more heat dissipation.

1.3 Scope of Present Study

This study established a hot-blast stove model to simulate on-gas and on-blast cycles of the hot-blast stove and found out the best mixing proportion between BFG and COG to promote the hot-blast stove efficiency and minimize the use of COG. Due to the limitation of simulation software and the pore distribution in checkers of hot-blast

stove being uniform, this study used porous media approximation to simulate the checkers.

In order to achieve the goal mentioned above, it is important to establish the optimization operation technique of hot-blast stove. During this technology development process, it is necessary to determine the mixing and burning characteristics of BFG and COG, heat transfer of solids and gases between regenerative bricks, cold blast and waste gas. Then it can establish the internal flow field and thermal field to identify the control mechanism of every parameter in the hot blast generation process completely. Basically, the main purpose of this technical research and development is to provide the theoretical fundament of optimization operation technique and reduce the experimental times in the scene of hot-blast stove operation. In addition, it can use this model to appraise the advanced combustion technology in the future, for example, the feasibility of rich oxygen combustion or bio-fuel application to the hot-blast stove.

CHAPTER 2

MATHEMATICAL MODEL

2.1 Domain Description

The hot-blast stove of the China Steel Cooperation is illustrated in Fig. 2-1. The hot-blast stove is a heat exchange equipment constructed from two cylindrical refractory shells filled with checker bricks and refractory materials. Its architecture can be divided into four parts (see Fig. 2-2): combustion chamber, checker chamber, dome and burner. Inlet1 is the inlet of mixed fuel gas of BFG and COG, inlet2 is the one of combustion air, inlet3 is the inlet of cold blast, outlet1 and outlet2 are the exits of waste gases and outlet3 is the exit of hot blast.

On gas cycle, the mixed fuel gas of BFG and COG burns with the combustion air. The combustion products, or waste gases, ascend through the dome, and then descends down through the checker bricks, transferring energy to them. Finally, the waste gas arrives at the bottom of checker chamber. This on-gas cycle is about fifty minutes and enables the checker bricks to reach the required temperature, and then the hot-blast stove stops providing the mixed fuel gas and the combustion air. Then the on-gas stage changes to the stage of stove change, whose transition is about ten minutes. Subsequently, the hot-blast stove changes to the on-blast cycle. The cold blast starts to enter the bottom of hot-blast stove, and it is heated as passing up through the checker bricks into the dome, and then proceeds into the combustion chamber before exiting the hot-blast stove through the hot blast valve. Eventually, the hot blast leaves the hot-blast

stove and is mixed with the cold blast to achieve the required hot blast temperature of blast furnace. The on-blast cycle is about sixty minutes. When this hot-blast stove changes to the on-gas cycle, another stove provides the prepared hot blast to the blast furnace.

This study simulates the condition of mixed fuel gas of BFG and COG to burn with combustion air in the hot-blast stove and the heat transfer between gas and solid. From the simulation, this study intends to find out the best proportion between BFG and COG in the mixed fuel gas to increase the thermal efficiency of hot-blast stove.

2.2 Governing Equations

In order to make the physical problem more tractable and simplified, some assumptions are made as follows:

1. All gaseous mixtures are regarded as the ideal gases.
2. Specific heat capacity for each checker is constant.
3. Conductivity for each checker is piece-wise linear.
4. Neglect the radiation heat transfer.
5. One-step global reactions of hydrogen, carbon monoxide, methane and ethylene with air are adopted to represent the chemical reaction (combustion) of mixed fuel gas of BFG and COG.
6. Use porous media approximation to simulate the checkers.

Based on the assumptions mentioned above, the governing equations are given in the following:

2.2.1 The Continuity and Momentum Equation

Turbulent flows are characterized by fluctuating velocity field. In Reynolds averaging, the solution variables in the instantaneous (exact) Navier-Stokes equations are decomposed into the mean (ensemble-averaged or time-averaged) and fluctuating components. For the velocity components:

$$u_i = \overline{u_i} + u_i' \tag{2-1}$$

where $\overline{u_i}$ and u_i' are the mean and fluctuating velocity components (i=1, 2, 3).

Likewise, for pressure and other scalar quantities:

$$\phi = \overline{\phi} + \phi' \tag{2-2}$$

where φ denotes a scalar such as pressure, energy, or species concentration. Substituting expressions of this form for the flow variables into the instantaneous continuity and momentum equations and taking a time (or ensemble) average (and dropping the overbar on the mean velocity, $\overline{u}$) yields the ensemble-averaged momentum equations. They can be written in Cartesian tensor form as:

$$\frac{\partial \rho}{\partial t} + \frac{\partial}{\partial x_i}(\rho u_i) = 0 \tag{2-3}$$

$$\frac{\partial}{\partial t}(\rho u_i) + \frac{\partial}{\partial x_j}(\rho u_i u_j) = -\frac{\partial P}{\partial x_i} + \frac{\partial}{\partial x_j}\left[\mu\left(\frac{\partial u_i}{\partial x_j} + \frac{\partial u_j}{\partial x_i} - \frac{2}{3}\delta_{ij}\frac{\partial u_l}{\partial x_l}\right)\right] + \frac{\partial}{\partial x_j}\left(-\rho\overline{u_i' u_j'}\right) \tag{2-4}$$

Equations (2-3) and (2-4) are called Reynolds-averaged Navier-Stokes (RANS) equations. They have the same general form as the instantaneous Navier-Stokes equations, with the velocities and other solution variables now representing ensemble-averaged (or time-averaged)

values. Additional terms now appear that represent the effects of turbulence. These Reynolds stresses, $-\rho\overline{u_i' u_j'}$, must be modeled in order to close Equation (2-4).

For variable-density flows, Equations (2-3) and (2-4) can be interpreted as Favre-averaged Navier-Stokes equations, with the velocities representing mass-averaged values. As such, Equations 2-3 and 2-4 can be applied to density-varying flows.

The Reynolds-averaged approach to turbulence modeling requires that the Reynolds stresses in Equation 2-4 be appropriately modeled. A common method employs the Boussinesq hypothesis to relate the Reynolds stresses to the mean velocity gradients:

$$-\overline{\rho u_i' u_j'} = \mu_t\left(\frac{\partial u_i}{\partial x_j}+\frac{\partial u_j}{\partial x_i}\right)-\frac{2}{3}\left(\rho k+\mu_t\frac{\partial u_i}{\partial x_i}\right)\delta_{ij} \qquad (2\text{-}5)$$

2.2.2 The Energy Conservation Equation

In FLUENT, turbulent heat transport is modeled using the concept of Reynolds' analogy to turbulent momentum transfer. The “modeled” energy equation is thus given by the following:

$$\frac{\partial}{\partial t}(\rho E)+\frac{\partial}{\partial x_i}\left[u_i(\rho E+p)\right]=\frac{\partial}{\partial x_j}\left(k_{eff}\frac{\partial T}{\partial x_j}+u_i(\tau_{ij})_{eff}\right)+S_h \qquad (2\text{-}6)$$

where E is the total energy, k_{eff} is the effective thermal conductivity, and $(\tau_{ij})_{eff}$ is the deviatoric stress tensor, defined as

$$(\tau_{ij})_{eff}=\mu_{eff}\left(\frac{\partial u_j}{\partial x_i}+\frac{\partial u_i}{\partial x_j}\right)-\frac{2}{3}\mu_{eff}\frac{\partial u_i}{\partial x_i}\delta_{ij} \qquad (2\text{-}7)$$

The term involving $(\tau_{ij})_{eff}$ represents the viscous heating, and is always computed in the coupled solvers. It is not computed by default in the segregated solver, but it can be enabled in the Viscous Model panel.

For the standard $k-\varepsilon$ models, the effective thermal conductivity is given by

$$k_{eff} = k + \frac{c_p \mu_t}{\mathrm{Pr}_t} \tag{2-8}$$

where k, in this case, is the thermal conductivity. The default value of the turbulent Prandtl number is 0.85. You can change the value of the turbulent Prandtl number in the Viscous Model panel. S_h includes the heat of chemical reaction, and any other volumetric heat sources you have defined.

In Equation (2-6), $E = h - \frac{p}{\rho} + \frac{v^2}{2}$ (2-9)

where sensible enthalpy h is defined for ideal gases as

$$h = \sum_j Y_j h_j \tag{2-10}$$

In Equation (2-10), Y_j is the mass fraction of species j and

$$h_j = \int_{T_{ref}}^{T} c_{p,j} dT \tag{2-11}$$

where T_{ref} is 298.15 K.

Sources of energy, S_h, in Equation (2-6) include the source of energy due to chemical reaction:

$$S_{h,rxn} = -\sum_j \frac{h_j^0}{M_j} R_j \tag{2-12}$$

where h_j^0 is the enthalpy of formation of species j and R_j is the

volumetric rate of creation of species j.

2.2.3 Momentum Equation in Porous Media

Porous media are modeled by an addition of a momentum source term (S_i) to the standard fluid flow equations. The source term is composed of two parts: a viscous loss term (Darcy law, the first term on the right-hand side of Equation 2-13) and an inertial loss term (the second term on the right-hand side of Equation 2-13).

$$S_i = -\left(\sum_{j=1}^{3} D_{ij} \mu v_j + \sum_{j=1}^{3} C_{ij} \frac{1}{2} \rho v_{mag} v_j \right) \tag{2-13}$$

where S_i is the source term for the i_{th} (x, y, or z) momentum equation, and D and C are prescribed matrices. This momentum sink contributes to the pressure gradient in the porous cell, creating a pressure drop that is proportional to the fluid velocity (or velocity squared) in the cell.

2.2.4 Energy Equation in Porous Media

FLUENT solves the standard energy transport equation in porous media regions with modifications to the conduction flux and the transient terms only. In the porous medium, the conduction flux uses an effective conductivity and the transient term includes the thermal inertia of the solid region on the medium described as follows:

$$\frac{\partial}{\partial t}\left(\gamma \rho_f E_f + (1-\gamma)\rho_s E_s\right) + \nabla \cdot \left(\vec{v}(\rho_f E_f + p)\right) = \nabla \cdot \left[k_{eff} \nabla T - \left(\sum_i h_i J_i \right) + (\vec{\tau} \cdot \vec{v}) \right] + S_f^h \tag{2-14}$$

where

E_f = total fluid energy

E_s = total solid medium energy

γ = porosity of the medium

k_{eff} = effective thermal conductivity of the medium

S_f^h = fluid enthalpy source term

The effective thermal conductivity in the porous medium, k_{eff}, is computed by FLUENT as the volumetric average of the fluid conductivity and the solid conductivity, which is in form of

$$k_{eff} = \gamma k_f + (1-\gamma)k_s \tag{2-15}$$

where γ is the porosity of the medium, k_f is the fluid phase thermal conductivity and k_s is the solid medium thermal conductivity.

2.2.5 The Species Transport Equation

When choosing to solve conservation equations for chemical species, FLUENT predicts the local mass fraction of each species, Y_i, through the solution of a convection-diffusion equation for the *ith* species. This conservation equation takes the following general form:

$$\frac{\partial}{\partial t}(\rho Y_i) + \nabla \cdot (\rho \vec{v} Y_i) = -\nabla \cdot \vec{J}_i + R_i + S_i \tag{2-16}$$

where R_i is the net rate of production of species i by chemical reaction (described later in the Section 2.2.6) and S_i is the rate of creation by addition from the dispersed phase plus any user-defined sources. An

equation of this form will be solved for N - 1 species where N is the total number of fluid phase chemical species present in the system. Since the mass fraction of the species must sum to unity, the Nth mass fraction is determined as one minus the sum of the N - 1 solved mass fractions. To minimize numerical error, the Nth species should be selected as that species with the overall largest mass fraction, such as N_2 when the oxidizer is air.

In turbulent flows, FLUENT computes the mass diffusion in the following form:

$$\vec{J}_j = -(\rho D_{i,m} + \frac{\mu_t}{Sc_t})\nabla Y_i \qquad (2\text{-}17)$$

where Sc_t is the turbulent Schmidt number ($\frac{\mu_t}{\rho D_t}$ where μ_t is the turbulent viscosity and D_t is the turbulent diffusivity). The default Sc_t is 0.7. Note that turbulent diffusion generally overwhelms laminar diffusion, and the specification of detailed laminar diffusion properties in turbulent flows is generally not warranted.

2.2.6 The Finite-Rate/Eddy-Dissipation Model

The reaction rates that appear as source terms in the species transport equation (2-15) are computed as follows. To consider the turbulent chemistry model, based on the work of Magnussen and Hjertager (1976), called the Finite-Rate/Eddy-Dissipation model. The finite-rate model computes the chemical source terms using Arrhenius expressions, ignoring the effects of turbulent fluctuations. The net source of the chemical species i due to reaction R_i, is computed as the sum of the

Arrhenius reaction sources over the N_r reactions in which the species participate:

$$R_i = M_{w,i} \sum_{r=1}^{N_r} \hat{R}_{i,r} \tag{2-18}$$

where $M_{w,i}$ is the molecular weight of species i and $\hat{R}_{i,r}$ is the Arrhenius molar rate of creation/destruction of species i in reaction r is given by:

$$\hat{R}_{i,r} = \Gamma(\nu''_{i,r} - \nu'_{i,r}) \left(k_{f,r} \prod_{j=1}^{N_r} [C_{j,r}]^{\eta'_{j,r}} - k_{b,r} \prod_{j=1}^{N_r} [C_{j,r}]^{\eta''_{j,r}} \right) \tag{2-19}$$

where

N_r = number of chemical species in reaction r

$C_{j,r}$ = molar concentration of each reactant and product species j in reaction r (kgmol/m^3)

$\eta'_{j,r}$ = forward rate exponent for each reactant and product species j in reaction r

$\eta''_{j,r}$ = backward rate exponent for each reactant and product species j in reaction r

Γ represents the net effect of third bodies on the reaction rate. This term is given by

$$\Gamma = \sum_{j}^{N_r} \gamma_{j,r} C_j \tag{2-20}$$

where $\gamma_{j,r}$ is the third body efficiency of the jth in the rth reaction. By default, FLUENT does not include third-body effects in the reaction

rate calculation.

The forward rate constant for reaction r, $k_{f,r}$, is computed using the Arrhenius expression

$$k_{f,r} = A_r T^{\beta_r} e^{-E_r / RT} \tag{2-21}$$

where

A_r = pre-exponential factor (consistent units)

β_r = temperature exponent (dimensionless)

E_r = activation energy for the reaction (J/kgmol)

R = universal gas constant (J/kgmol-K)

Here one step global reactions of hydrogen, carbon monoxide, methane and ethylene are adopted, the rate exponent, pre-exponential factor, temperature exponent and activation energy is described as follows:

(1)Hydrogen combustion reaction:

$$H_2 + 0.5O_2 \rightarrow H_2O \tag{2-22}$$

with reaction rate expression:

$$\frac{d[H_2]}{dt} = -(9.87 \times 10^8) \exp(-3.1 \times 10^7 / RT)[H_2][O_2] \tag{2-23}$$

(2)Carbon monoxide combustion reaction:

$$CO + 0.5O_2 \rightarrow CO_2 \tag{2-24}$$

with reaction rate expression:

$$\frac{d[CO]}{dt} = -(2.239 \times 10^{12}) \exp(-1.7 \times 10^8 / RT)[CO][O_2]^{0.25}[H_2O]^{0.5} \tag{2-25}$$

(3)Methane combustion reaction

$$CH_4 + 2O_2 \rightarrow CO_2 + 2H_2O \tag{2-26}$$

with reaction rate expression:

$$\frac{d[CH_4]}{dt} = -(2.119\times10^{11})\exp(-2.027\times10^{8}/RT)[CH_4]^{0.2}[O_2]^{1.3} \tag{2-27}$$

(4)Ethylene combustion reaction

$$C_2H_4 + 3O_2 \rightarrow 2CO_2 + 2H_2O \tag{2-28}$$

with reaction rate expression:

$$\frac{d[C_2H_4]}{dt} = -(1.125\times10^{10})\exp(-1.256\times10^{8}/RT)[C_2H_4]^{0.1}[O_2]^{1.65} \tag{2-29}$$

2.2.7 The Standard $k-\varepsilon$ Model

The standard $k-\varepsilon$ model is a semi-empirical model based on model transport equations for the turbulence kinetic energy (k) and its dissipation rate (ε). The model transport equation for k is derived from the exact equation, while the model transport equation for ε was obtained using physical reasoning and bears little resemblance to its mathematically exact counterpart.

In the derivation of the $k-\varepsilon$ model, it was assumed that the flow is fully turbulent, and the effects of molecular viscosity are negligible. The standard $k-\varepsilon$ model is therefore valid only for fully turbulent flows.

The standard $k-\varepsilon$ model in FLUENT falls within this class of turbulence model and has become the workhorse of practical engineering flow calculations in the time since it was proposed by Launder and Spalding (1972). Robustness, economy, and reasonable accuracy for a wide range of turbulent flows explain its popularity in industrial flow and heat transfer simulations. It is a semi-empirical model, and the derivation

of the model equations relies on phenomenological considerations and empiricism.

Standard Wall Functions

The standard wall functions in FLUENT are based on the proposal of Launder and Spalding (1974), and have been most widely used for industrial flows.

Momentum

The law-of-the-wall for mean velocity yields

$$U^* = \frac{1}{k}\ln(Ey^*) \tag{2-30}$$

where

$$U^* \equiv \frac{U_p C_\mu^{1/4} k_p^{1/2}}{\tau_w / \rho} \tag{2-31}$$

$$y^* \equiv \frac{\rho C_\mu^{1/4} k_p^{1/2} y_p}{\mu} \tag{2-32}$$

In which

k = von Karman constant (=0.487)

E = empirical constant (=9.793)

U_p = mean velocity of the fluid at point P

k_p = turbulent kinetic energy at point P

y_p = distance from point P to the wall

μ = dynamic viscosity of the fluid

Energy

Reynolds' analogy between momentum and energy transport gives a similar logarithmic law for mean temperature. As in the law-of-the-wall for mean velocity, the law-of-the-wall for temperature employed in FLUENT comprises the following two different laws:

- Linear law for the thermal conduction sublayer where conduction is important.
- Logarithmic law for the turbulent region where effects of turbulence dominate conduction.

The thickness of the thermal conduction layer is, in general, different from the thickness of the (momentum) viscous sublayer, and changes from fluid to fluid. For example, the thickness of the thermal sublayer for a high-Prandtl-number fluid (e.g., oil) is much less than its momentum sublayer thickness. For fluids of low Prandtl numbers (e.g., liquid metal), on the contrary, it is much larger than the momentum sublayer thickness.

In highly compressible flows, the temperature distribution in the near-wall region can be significantly different from that of low subsonic flows, due to the heating by viscous dissipation. In FLUENT, the temperature wall functions include the contribution from the viscous heating.

The law-of-the-wall implemented in FLUENT has the following composite form:

$$T^* \equiv \frac{(T_w - T_p)\rho C_p C_\mu^{1/4} k_p^{1/2}}{\dot{q}}$$

$$= \Pr y^* + \frac{1}{2}\rho \Pr \frac{C_\mu^{1/4} k_p^{1/2}}{\dot{q}} U_p^2 \qquad (y^* < y_T^*)$$

$$= \mathrm{Pr}_t \left[\frac{1}{k} \ln(Ey^*) + P \right] + \frac{1}{2} \rho \frac{C_\mu^{1/4} k_p^{1/2}}{\dot{q}} \left\{ \mathrm{Pr}_t U_p^2 + (\mathrm{Pr} - \mathrm{Pr}_t) U_c^2 \right\} \quad (y^* > y_T^*) \qquad (2\text{-}33)$$

where P is computed by using the formula given by Jayatilleke (1969):

$$P = 9.24 \left[\left(\frac{\mathrm{Pr}}{\mathrm{Pr}_t} \right)^{3/4} - 1 \right] \left[1 + 0.28\, e^{-0.007\, \mathrm{Pr}/\, \mathrm{Pr}_t} \right] \qquad (2\text{-}34)$$

and

k_p = turbulent kinetic energy at point P

ρ = density of fluid

C_p = specific heat of fluid

$\dot{q}$ = wall heat flux

T_p = temperature at the cell adjacent to wall

T_w = temperature at wall

Pr = molecular Prandtl number $(\mu C_p / k_f)$

Pr_t = turbulent Prandtl number (0.85 at the wall)

A = Van Driest constant (=26)

U_c = mean velocity magnitude at $y^* = y_T^*$

Note that, for the segregated solver, the terms

$$\frac{1}{2} \rho \mathrm{Pr} \frac{C_\mu^{1/4} k_p^{1/2}}{\dot{q}} U_p^2$$

and

$$\frac{1}{2} \rho \frac{C_\mu^{1/4} k_p^{1/2}}{\dot{q}} \left\{ \mathrm{Pr}_t U_p^2 + (\mathrm{Pr} - \mathrm{Pr}_t) U_c^2 \right\}$$

will be included in Equation 2-33 only for compressible flow calculations.

The non-dimensional thermal sublayer thickness, y_T^* , in Equation 2-33 is computed as the y^* value at which the linear law and the logarithmic law intersect, given the molecular Prandtl number of the fluid being modeled.

The procedure of applying the law-of-the-wall for temperature is as follows. Once the physical properties of the fluid being modeled are specified, its molecular Prandtl number is computed. Then, given the molecular Prandtl number, the thermal sublayer thickness, y_T^* , is computed from the intersection of the linear and logarithmic profiles, and stored.

During the iteration, depending on the y_T^* value at the near-wall cell, either the linear or the logarithmic profile in Equation 2-33 is applied to compute the wall temperature T_w or heat flux $\dot{q}$ (depending on the type of the thermal boundary conditions).

The function for P given by Equation 2-34 is relevant for the smooth walls. For the rough walls, however, this function is modified as follows:

$$P_{rough} = 3.15\,\mathrm{Pr}^{0.695}\left(\frac{1}{E'}-\frac{1}{E}\right)^{0.359}+\left(\frac{E'}{E}\right)^{0.6}P \qquad (2\text{-}35)$$

where E' is wall function constant modified for the rough walls.

Species

When using wall functions for species transport, FLUENT assumes that species transport behaves analogously to heat transfer. Similarly to Equation 2-33, the law-of-the-wall for species can be expressed for constant property flow with no viscous dissipation as

$$Y^* \equiv \frac{(Y_{i,w} - Y_i)\rho C_\mu^{1/4} k_p^{1/2}}{J_{i,w}}$$

$$= Scy^* \qquad (y^* < y_c^*)$$

$$= Sc_t\left[\frac{1}{k}\ln(Ey^*) + P_c\right] \qquad (y^* > y_c^*) \tag{2-36}$$

where Y_i is the local species mass fraction, S_c and Sc_t are molecular and turbulent Schmidt numbers, and $J_{i,w}$ is the diffusion flux of species i at the wall. Note that P_c and y_c^* are calculated in a similar way as P and y_c^*, with the difference being that the Prandtl numbers are always replaced by the corresponding Schmidt numbers.

Turbulence

In the $k-\varepsilon$ models, the k equation is solved in the whole domain including the wall-adjacent cells. The boundary condition for k imposed at the wall is

$$\frac{\partial k}{\partial n} = 0 \tag{2-37}$$

where n is the local coordinate normal to the wall.

The production of kinetic energy, G_k, and its dissipation rate, ε, at the wall-adjacent cells, which are the source terms in the k equation, are computed on the basis of the local equilibrium hypothesis. Under this assumption, the production of k and its dissipation rate are assumed to be equal in the wall-adjacent control volume.

Thus, the production of k is computed from

$$G_k \approx \tau_w \frac{\partial U}{\partial y} = \tau_w \frac{\tau_w}{k\rho C_\mu^{1/4} k_p^{1/2} y_p} \tag{2-38}$$

and ε is computed from

$$\varepsilon_p = \frac{C_\mu^{3/4} k_p^{3/2}}{k y_p} \tag{2-39}$$

The ε equation is not solved at the wall-adjacent cells, but instead is computed using Equation 2-39.

2.2.7.1 Transport Equations for the Standard $k-\varepsilon$ Model

The turbulence kinetic energy, k , and its rate of dissipation, ε , are obtained from the following transport equations:

$$\frac{\partial}{\partial t}(\rho k) + \frac{\partial}{\partial x_i}(\rho k u_i) = \frac{\partial}{\partial x_j}\left[(\mu + \frac{\mu_t}{\sigma_k})\frac{\partial k}{\partial x_j}\right] + G_k + G_b - \rho\varepsilon - Y_M + S_k \tag{2-40}$$

and

$$\frac{\partial}{\partial t}(\rho \varepsilon) + \frac{\partial}{\partial x_i}(\rho \varepsilon u_i) = \frac{\partial}{\partial x_j}\left[(\mu + \frac{\mu_t}{\sigma_\varepsilon})\frac{\partial \varepsilon}{\partial x_j}\right] + C_{1\varepsilon}\frac{\varepsilon}{k}(G_k + C_{3\varepsilon}G_b) - C_{2\varepsilon}\rho\frac{\varepsilon^2}{k} + S_\varepsilon \tag{2-41}$$

In these equations, G_k represents the generation of turbulence kinetic energy due to the mean velocity gradients, calculated as described in Section 2.2.7.1.1: Modeling Turbulent Production in the $k-\varepsilon$ Models. G_b is the generation of turbulence kinetic energy due to buoyancy, calculated as described in Section 2.2.7.1.2: Effects of Buoyancy on Turbulence in the $k-\varepsilon$ Models. Y_M represents the contribution of the fluctuating dilatation in compressible turbulence to the overall dissipation rate, calculated as described in Section 2.2.7.1.3: Effects of

Compressibility on Turbulence in the $k-\varepsilon$ Models. $C_{1\varepsilon}$, $C_{2\varepsilon}$ and $C_{3\varepsilon}$ are constants. σ_k and σ_ε are the turbulent Prandtl numbers for k and ε, respectively. S_k and S_ε are user-defined source terms.

Modeling the Turbulent Viscosity

The turbulent (or eddy) viscosity, μ_t, is computed by combining k and ε as follows:

$$\mu_t = \rho C_\mu \frac{k^2}{\varepsilon} \tag{2-42}$$

where C_μ is a constant.

Model Constants

The model constants $C_{1\varepsilon}$; $C_{2\varepsilon}$; C_μ; σ_k, and σ_ε have the following default values:

$C_{1\varepsilon}$=1.44, $C_{2\varepsilon}$=1.92, C_μ=0.09, σ_k=1.0, σ_ε=1.3

These default values have been determined from experiments with air and water for fundamental turbulent shear flows including homogeneous shear flows and decaying isotropic grid turbulence. They have been found to work fairly well for a wide range of wall-bounded and free shear flows.

Although the default values of the model constants are the standard ones most widely accepted, you can change them (if needed) in the Viscous Model panel.

2.2.7.1.1 Modeling Turbulent Production in the $k-\varepsilon$ Models

The term G_k, representing the production of turbulence kinetic energy, is modeled identically for the standard $k-\varepsilon$ models. From the exact equation for the transport of k, this term may be defined as

$$G_k = -\rho\overline{u_i' u_j'}\frac{\partial u_j}{\partial x_i} \tag{2-43}$$

To evaluate G_k in a manner consistent with the Boussinesq hypothesis,

$$G_k = \mu_t S^2 \tag{2-44}$$

where S is the modulus of the mean rate-of-strain tensor, defined as

$$S \equiv \sqrt{2S_{ij}S_{ij}} \tag{2-45}$$

2.2.7.1.2 Effects of Buoyancy on Turbulence in the $k-\varepsilon$ Models

When a non-zero gravity field and temperature gradient are present simultaneously, the $k-\varepsilon$ models in FLUENT account for the generation of k due to buoyancy(G_b in Equation 2-40), and the corresponding contribution to the production of ε in Equation 2-41.

The generation of turbulence due to buoyancy is given by

$$G_b = \beta g_i \frac{\mu_t}{\mathrm{Pr}_t}\frac{\partial T}{\partial x_i} \tag{2-46}$$

where Pr_t is the turbulent Prandtl number for energy and g_i is the component of the gravitational vector in the *ith* direction. For the standard $k-\varepsilon$ models, the default value of Pr_t is 0.85. The coefficient of thermal expansion, β, is defined as

$$\beta = -\frac{1}{\rho}(\frac{\partial \rho}{\partial T})_p \tag{2-47}$$

For ideal gases, Equation (2-46) reduces to

$$G_b = -g_i \frac{\mu_t}{\rho \Pr_t} \frac{\partial \rho}{\partial x_i} \tag{2-48}$$

It can be seen from the transport equation for k (Equation 2-40) that turbulence kinetic energy tends to be augmented $(G_b > 0)$ in unstable stratification. For stable stratification, buoyancy tends to suppress the turbulence $(G_b < 0)$. In FLUENT, the effects of buoyancy on the generation of k are always included when you have both a non-zero gravity field and a non-zero temperature (or density) gradient.

While the buoyancy effects on the generation of k are relatively well understood, the effect on ε is less clear. In FLUENT, by default, the buoyancy effects on ε are neglected simply by setting G_b to zero in the transport equation for ε (Equation 2-41).

However, it can include the buoyancy effects on ε in the Viscous Model panel. In this case, the value of G_b given by Equation 2-48 is used in the transport equation for ε (Equation 2-41).

The degree to which ε is affected by the buoyancy is determined by the constant $C_{3\varepsilon}$. In FLUENT, $C_{3\varepsilon}$ is not specified, but is instead calculated according to the following relation:

$$C_{3\varepsilon} = \tanh\left|\frac{v}{u}\right| \tag{2-49}$$

where v is the component of the flow velocity parallel to the gravitational vector and u is the component of the flow velocity perpendicular to the gravitational vector. In this way, $C_{3\varepsilon}$ will become 1

for buoyant shear layers for which the main flow direction is aligned with the direction of gravity. For buoyant shear layers that are perpendicular to the gravitational vector, $C_{3\varepsilon}$ will become zero.

2.2.7.1.3 Effects of Compressibility on Turbulence in the $k-\varepsilon$ Models

For high-Mach-number flows, compressibility affects turbulence through so-called dilatation dissipation, which is normally neglected in the modeling of incompressible flows. Neglecting the dilatation dissipation fails to predict the observed decrease in spreading rate with increasing Mach number for compressible mixing and other free shear layers. To account for these effects in the $k-\varepsilon$ models in FLUENT, the dilatation dissipation term, Y_M , is included in the k equation. This term is modeled according to a proposal by Sarkar (1990):

$$Y_M = 2\rho\varepsilon M_t^2 \tag{2-50}$$

where M_t is the turbulent Mach number, defined as

$$M_t = \sqrt{\frac{k}{a^2}} \tag{2-51}$$

where $a(\equiv\sqrt{\gamma RT})$ is the speed of sound. This compressibility modification always takes effect when the compressible form of the ideal gas law is used.

2.3 Setting up Two Cycle Simulation Procedures

Under maintaining the actual configuration of hot-blast stove

geometry, it is advisable to reset the mixing proportion between BFG and COG in the mixed fuel gas to increase the thermal efficiency of hot-blast stove.

The actual operation of hot-blast stove is divided into on-gas and on-blast cycles. Therefore, this study divides the simulation procedure into on-gas and on-blast cycles. They are described in the following:

1. On-Gas Cycle

The hot-blast stove is heated by the combustion gases in the combustion chamber during the on-gas cycle. The combustion products, or waste gases, enter the dome at the top of hot-blast stove and then descend down through the regenerative bricks, referred to as the checker bricks, transferring energy to these bricks.

2. On-Blast Cycle

Hot blast is produced during the on-blast cycle. The cold blast enters the bottom of the hot-blast stove, and it is heated as passing up through the checkers into the dome, and then proceeds into the combustion chamber before exiting the hot-blast stove through the hot blast valve. Then the hot blast leaves the hot-blast stove, and mixes with the cold blast to achieve the required hot blast temperature of the blast furnace.

2.4 Initial Conditions and Boundary Conditions

2.4.1 Initial Conditions

Step1. Initialize the flow field

The velocities in x, y and z directions equal to zero are taken to be the initial flow field of on-gas, stove-change and on-blast cycles in this

study.

Step2. Initialize the thermal field

The temperatures of checker (CRN130) and checker support in the first minute of on-gas cycle provided by CSC are adopted to calculate the initial temperature profiles in each checker. Use such profiles as the initial conditions of checker chamber and simulate the on-gas cycle by Eddy-Dissipation combustion model. Through the simulation of on-gas cycle, the temperature profile of whole hot-blast stove in the end of on-gas cycle is obtained, and it is applied to be the initial conditions for stove-change cycle. The temperature profile of hot-blast stove in the end of stove-change cycle simulation is used to be the initial conditions of on-blast cycle. Eventually, the temperature profile of hot-blast stove in the end of on-blast cycle now is utilized to really be the initial conditions of on-gas cycle in this study.

2.4.2 Boundary Conditions

The establishment of boundary conditions is based on the data provided by the China Steel Cooperation.

In the model domain, the boundary conditions are specified as the following: three inlets, three outlets, solid, gas, and wall boundary conditions.

An example involved with the calculation methods and steps for the setting of boundary conditions are given in detail as following.

Operation Conditions:

The operating pressure of hot-blast stove is set to be 101325 Pascal

and the gravity is set to be -9.8 m/s^2 in y-direction.

The Inlet Boundary Conditions

There are three inlet boundaries. Inlet1 supplies the mixed fuel gas, inlet2 supplies the combustion air, and inlet3 supplies the cold blast.

1. Mixed Fuel Gas Inlet Boundary Conditions of Hot-Blast Stove

The boundary conditions here demand for velocity, temperature, and species mass fraction.

Step1. Decide velocity and temperature:

The boundary conditions of velocity and temperature in the inlet of mixed fuel gas are given from the data provided by the China Steel Cooperation.

Step2. Set specie compositions and mass fraction of mixed fuel gas:

The boundary conditions of species compositions and mass fraction in the inlet of mixed fuel gas are given from the data provided by the China Steel Cooperation.

2. Combustion Air Inlet Boundary Conditions of Hot-Blast Stove

The boundary conditions here demand for velocity, temperature, and species mass fraction.

Step1. Decide velocity and temperature:

The boundary conditions of velocity and temperature in the inlet of combustion air are given from the data provided by the China Steel Cooperation.

Step2. Set species compositions and mass fraction of mixed fuel gas:

The boundary conditions of specie compositions and mass fraction in the inlet of combustion air are given from the data provided by the China Steel Cooperation.

3. Cold Blast Inlet Boundary Conditions of Hot-Blast Stove

The boundary conditions here demand for velocity, temperature, and species mass fraction.

Step1. Decide velocity and temperature:

The boundary conditions of velocity and temperature in the inlet of cold blast are given from the data provided by the China Steel Cooperation.

Step2. Set specie compositions and mass fraction of mixed fuel gas:

The boundary conditions of specie compositions and mass fraction in the inlet of cold blast are given from the data provided by the China Steel Cooperation.

.

The Outlet Boundary Conditions

There are three outlet boundaries. Outlet1 and outlet2 discharge the waste gas, outlet3 discharges the hot blast.

The boundary conditions here demand for pressure only, and the pressure here is set to be 101325 Pascal.

Wall Boundary Conditions

Excepting the inlet and outlet boundaries, the remaining geometry is all wall boundaries, which are the no-slip boundary conditions (u, v, w=0) for velocity and adiabatic.

Porous Media

The top view of real checkers in the hot-blast stove is shown in Fig. 2-3. The porosity of every checkers is 0.225, obtained by following formula.

Porosity = wetted volume of fluid / total volume of checker region

$$= 4296 \times \pi \times (55/2)^2 / \pi \times (7600/2)^2 = 0.225$$

In Fluent, the porous media model can be used for a wide variety of problems, including flows through packed beds, filter papers, perforated plates, flow distributors, and tube banks. Due to the limitation of simulation software and the uniform pore distribution requirement of checkers in hot-blast stove, this study applied porous media approximation to simulate the checkers.

The materials and heights for each layer of checkers in the hot-blast stove are shown in Fig. 2-4 schematically, and their corresponding thermal properties used for simulation are listed in Table 2-1. The specific heats are maintained constant for each layer of checkers. As to the conductivities, the linear interpolations are applied for the temperature range in the simulation.

Table 2-1 Thermal properties of checkers for simulation

Thermal property / Material	Specific heat capacity (J/kg-K)	Thermal conductivity (W/m-K)		
S21	1,180	273K	973K	2000K
		1.40	1.57	2.00
CRN130	1,180	273K	973K	2000K
		2.21	2.04	1.98
SF125	1,050	273K	973K	2000K
		1.28	1.35	1.40
SF120	1,050	273K	973K	2000K
		1.28	1.35	1.40
SF115	1,050	273K	973K	2000K
		1.28	1.35	1.40

CHAPTER 3

INTRODUCTION TO NUMERICAL ALGORITHM

3.1 Introduction to FLUENT Software

FLUENT is a state-of-the-art computer program for modeling fluid flow and heat transfer in complex geometries. It provides complete mesh flexibility, including the ability to solve the flow problems using unstructured meshes that can be generated about complex geometries with relative ease. Supported mesh types include 2D triangular/quadrilateral, 3D tetrahedral/hexahedral/pyramid, and mixed (hybrid) meshes. FLUENT also allows to refine or coarsen grid based on the flow solution.

FLUENT is written in the C computer language and makes full use of the flexibility and power offered by the language. Consequently, true dynamic memory allocation, efficient data structures, and flexible solver control are all possible. In addition, FLUENT uses a client/server architecture, which allows it to run as separate simultaneous processes on client desktop workstations and powerful compute servers. This architecture allows for efficient execution, interactive control, and complete flexibility between different types of machines or operating systems.

All functions required to compute a solution and display the results are accessible in FLUENT through an interactive, menu-driven interface.

3.2 Numerical Method for FLUENT

FLUENT uses Segregated Solver method to solve the governing integral equations for the conservation of mass and momentum, and (when appropriate) for energy and other scalars such as turbulence and chemical species. In case a control-volume-based technique is used that consists of:

- Division of the domain into discrete control volumes using a computational grid.
- Integration of the governing equations on the individual control volumes to construct algebraic equations for the discrete dependent variables such as velocities, pressure, temperature, and conserved scalars.
- Linearization of the discretized equations and solution of the resultant linear equation system to yield updated values of the dependent variables.

3.2.1 Segregated Solution Method

Using this approach, the governing equations are solved sequentially (i.e., segregated from one another). Because the governing equations are non-linear (and coupled), several iterations of the solution loop must be performed before a converged solution is obtained. Each iteration consists of the steps illustrated in Fig. 3-1 and outlined below:

1. Fluid properties are updated, based on the current solution. (If the calculation has just begun, the fluid properties will be updated based on the initialized solution.)
2. The u, v, and w momentum equations are each solved in turn using

current values for pressure and face mass fluxes, in order to update the velocity field.

3. Since the velocities obtained in Step 2 may not satisfy the continuity equation locally, a Poisson-type equation for the pressure correction is derived from the continuity equation and the linearized momentum equations. This pressure correction equation is then solved to obtain the necessary corrections to the pressure and velocity fields and the face mass fluxes such that continuity is satisfied.
4. Where appropriate equations for scalars such as turbulence, energy, species, and radiation are solved using the previously updated values of the other variables.
5. When interphase coupling is to be included, the source terms in the appropriate continuous phase equations may be updated with a discrete phase trajectory calculation.
6. A check for convergence of the equation set is made.

These steps are continued until the convergence criteria are met.

3.2.2 Linearization: Implicit

In the segregated solution method the discrete, non-linear governing equations are linearized to produce a system of equations for the dependent variables in every computational cell. The resultant linear system is then solved to yield an updated flow-field solution.

The manner in which the governing equations are linearized may take an implicit form with respect to the dependent variable (or set of variables) of interest.

The implicit form is described in the following:

- Implicit: For a given variable, the unknown value in each cell is computed using a relation that includes both existing and unknown values from neighboring cells. Therefore each unknown will appear in more than one equation in the system, and these equations must be solved simultaneously to give the unknown quantities.

In the segregated solution method each discrete governing equation is linearized implicitly with respect to that equation's dependent variable. This will result in a system of linear equations with one equation for each cell in the domain. Because there is only one equation per cell, this is sometimes called a scalar system of equations. A point implicit (Gauss-Seidel) linear equation solver is used in conjunction with an algebraic multigrid (AMG) method to solve the resultant scalar system of equations for the dependent variable in each cell. For example, the x-momentum equation is linearized to produce a system of equations in which u velocity is the unknown. Simultaneous solution of this equation system (using the scalar AMG solver) yields an updated u-velocity field.

In summary, the segregated approach solves for a single variable field (e.g., p) by considering all cells at the same time. It then solves for the next variable field by again considering all cells at the same time, and so on. There is no explicit option for the segregated solver.

3.2.3 Discretization

FLUENT uses a control-volume-based technique to convert the governing equations to algebraic equations that can be solved numerically. This control volume technique consists of integrating the governing equations about each control volume, yielding discrete equations that

conserve each quantity on a control-volume basis.

Discretization of the governing equations can be illustrated most easily by considering the steady-state conservation equation for transport of a scalar quantity ϕ. This is demonstrated by the following equation written in integral form for an arbitrary control volume V as follows:

$$\oint \rho\phi\vec{v} \cdot d\vec{A} = \oint \Gamma_\phi \nabla\phi \cdot d\vec{A} + \int_V S_\phi dV \tag{3-1}$$

where

ρ = density

$\vec{v}$ = velocity vector

$\vec{A}$ = surface area vector

Γ_ϕ = diffusion coefficient for ϕ

∇_ϕ = gradient of ϕ

S_ϕ = source of ϕ per unit volume

Equation (3-1) is applied to each control volume, or cell, in the computational domain. The two-dimension, triangular cell shown in Fig. 3-2 is an example of such a control volume. Discretization of Equation 3-1on a given cell yields

$$\sum_f^{N_{faces}} \rho_f \vec{v}_f \phi_f \cdot \vec{A}_f = \sum_f^{N_{faces}} \Gamma_\phi (\nabla\phi)_n \cdot \vec{A}_f + S_\phi V \tag{3-2}$$

where

N_{faces} = number of faces enclosing cell

ϕ_f = value of ϕ convected through face f

$\rho_f \vec{v}_f \cdot \vec{A}_f$ = mass flux through the face

$\vec{A}_f$ = area of face f

$(\nabla\phi)_n$ = magnitude of $\nabla\phi$ normal to face f

V = cell volume

The equations solved by FLUENT take the same general form as the one given above and apply readily to multi-dimension, unstructured meshes composed of arbitrary polyhedral.

By default, FLUENT stores discrete values of the scalar ϕ at the cell center (c0 and c1 in Fig. 3-2). However, face values ϕ_f are required for the convection terms in Equation 3-2 and must be interpolated from the cell center values. This is accomplished using an upwind scheme.

3.2.3.1 First-Order Upwind Scheme

When first-order accuracy is desired, quantities at cell faces are determined by assuming that the cell-center values of any field variable represent a cell-average value and hold throughout the entire cell; the face quantities are identical to the cell quantities. Thus when first-order upwind is selected, the face value φ_f is set equal to the cell-center value of φ in the upstream cell.

3.2.4 SIMPLE Algorithm

The SIMPLE algorithm uses a relationship between velocity and pressure corrections to enforce mass conservation and to obtain the pressure field.

If the momentum equation is solved with a guessed pressure field p^*,

the resulting face flux J_f^* , computed from Equation 3-3 $J_f = \hat{J}_f + d_f(p_{co} - p_{c1})$ (where p_{co} and p_{c1} are the pressures within the two cells on either side of the face, and $\hat{J}_f$ contains the influence of velocities in these cell. The term d_f is a function of $\bar{a}_p$, the average of the momentum equation $\bar{a}_p$ coefficients for the cells on either side of face f.)

$$J_f^* = \hat{J}_f^* + d_f(p_{co}^* - p_{c1}^*) \tag{3-4}$$

does not satisfy the continuity equation. Consequently, a correction J_f' is added to the face flux J_f^* so that the corrected face flux, J_f

$$J_f = J_f^* + J_f' \tag{3-5}$$

satisfies the continuity equation. The SIMPLE algorithm postulates that J_f' be written as

$$J_f' = d_f(p_{co}' - p_{c1}') \tag{3-6}$$

where p' is the cell pressure correction.

The SIMPLE algorithm substitutes the flux correction equations (Equations 3-5 and 3-6) into the discrete continuity equation ($\sum_f^{N_{faces}} J_f A_f = 0$) to obtain a discrete equation for the pressure correction p' in the cell:

$$a_p p' = \sum_{nb} a_{nb} p_{nb}' + b \tag{3-7}$$

where the source term b is the net flow rate into the cell:

$$b = \sum_{f}^{N_{faces}} J_f^* A_f \tag{3-8}$$

The pressure-correction equation (Equation 3-7) may be solved using the algebraic multigrid (AMG) method. Once a solution is obtained, the cell pressure and the face flux are used correctly.

$$p = p^* + \alpha_p p' \tag{3-9}$$

$$J_f = J_f^* + d_f (p'_{co} - p'_{c1}) \tag{3-10}$$

Here α_p is the under-relaxation factor for pressure. The corrected face flux J_f, satisfies the discrete continuity equation identically during each iteration.

3.3 Computational Procedure of Simulation

The complete operating procedure for using FLUENT package software is carried out through the following processes sequentially.

3.3.1 Model Geometry

For FLUENT calculations, it is necessary to build a model firstly. This study used the pre-processor software Solid Works to build the hot-blast stove model as shown in Fig. 3-3. It has to divide the hot-blast stove into finite volumes in this step in order to generate grids conveniently.

The inlets of mixed fuel gas and combustion air are built as cylinders with a diameter of 1.4 m, and the inlet of cold blast is built as a cylinder with a diameter of 1.6 m. The outlets of waste gas are built as cylinders

with a diameter of 1.6 m, and the outlet of hot blast is built as a cylinder with a diameter of 1.54 m.

3.3.2 Grid Generation

After building the hot-blast stove model, it has to use the pre-processor Gambit to generate grids as shown in Fig. 3-4. It defines the different grid sizes in different volumes in this step. Defining the smaller grid size for the smaller volume will increase the accuracy of the simulation, but it must consider the applicability of the grid size. If it adopts too small grid size in this step, the simulation time will be influenced. Besides, if the largest grid size is different from the smallest one too much, it will influence the FLUENT calculation.

3.3.3 FLUENT Calculation

Once determine the important features of the problem that one wants to solve, it will follow the basic procedural steps shown below.

1. Create the model geometry and grid.
2. Start the appropriate solver for 2D or 3D modeling.
3. Import the grid.
4. Check the grid.
5. Select the solver formulation.
6. Choose the basic equations to be solved: laminar or turbulent (or inviscid), chemical species or reaction, heat transfer models, etc. Identify additional models needed: fans, heat exchangers, porous media, etc.
7. Specify material properties.

8. Specify the boundary conditions.
9. Adjust the solution control parameters.
10. Initialize the flow field.
11. Calculate a solution.
12. Examine the results.
13. Save the results.
14. If necessary, refine the grid or consider revisions to the numerical or physical model.

3.4 Grid and Time Step Tests

In order to obtain the acceptable numerical solution, this study applies the structure and unstructured grids produced from geometry models to carry out the grid and time step tests. The grid and time step tests all include on-gas and on-blast cycles.

This study uses the root mean square percentage error method [15] to appraise the accuracy of simulation. The root mean square percentage error is calculated from the equation that is written as follows:

$$RMSE\% = \left\{ \frac{1}{N} \sum_{1}^{N} \left[(Y_s - Y_e) / Y_e \right]^2 \right\}^{1/2} \qquad (3\text{-}11)$$

where

N = example number

Y_s = simulation value

Y_e = experiment value

1. On-Gas Cycle:

The boundary conditions of inlet1 and inlet2 (see Fig. 2-2 for the locations) are described as follows: Velocity and temperature in the inlet of mixed fuel gas are 27.2 m/s and 491 K respectively, and the mass fraction is tabulated in Table 3-1. Velocity and temperature in the inlet of combustion air are 12.9 m/s and 319 K respectively.

Table 3-1 Mass fractions in the inlet of mixed fuel gas

BFG+COG	
Species	Mass fraction
CO_2	0.327968
CO	0.207077
H_2	0.003213
N_2	0.458232
O_2	0.000023
CH_4	0.002933
C_2H_4	0.000554

There are two waste gas outlets (outlet1 and outlet2) (see Fig. 2-2 for the locations) in the hot-blast stove. The waste gas temperature listed in the experimental data is the temperature that is measured when the waste gases at outlet1 and outlet2 mix. Therefore, the waste gas temperature of simulation mentioned below is using the average waste gas temperature at oulet1 and outlet2.

The purpose for simulating the on-gas cycle is to obtain the waste

gas temperature.

Four different grid distributions (densities) are tested: they are 1027246, 1088989, 1324338 and 1834332 respectively. And three different time steps are tested: 60-, 30- and 15-second respectively. The test results are given in Table 3-2 to Table 3-3 and Fig. 3-5 to Fig. 3-6, in which the locations of inlet1, inlet2, outlet1 and outlet2 are illustrated schematically in Fig. 2-2. To consider the computational time and accuracy, the grid number of 1088989 and time step of 30 second are selected here.

Table 3-2 Grid test results of different grid densities for on-gas cycle

Waste gas temperature (Time step= 60 sec)	
Grid Number	RMSE (%)
1027246	2.1
1088989	2.0
1324338	2.0
1834332	2.4

Table 3-3 Time step test results for on-gas cycle

Waste gas temperature (Grid number= 1088989)	
Time step (sec)	RMSE (%)
60	2.0
30	2.0
15	2.1

2. **On-Blast Cycle:**

The boundary conditions of inlet3 (see Fig. 2-2 for the location) are described as follows: Velocity and temperature in the inlet of cold blast (air) are 39.3 m/s and 493 K respectively.

The purpose for simulating the on-blast cycle is to obtain the average hot blast temperature at outlet3 (see Fig. 2-2 for the location).

Four different grid distributions (densities) are tested: they are 1027246, 1088989, 1324338 and 1834332, respectively. And three different time steps are tested: 60-, the 30- and 15-second respectively. The test results are given in Table 3-4 to Table 3-5 and Fig. 3-7 to Fig. 3-8, in which the locations of inlet3 and outlet3 are illustrated schematically in Fig. 2-2. To consider the computational time and accuracy, the grid number of 1088989 and time step of 30 second are selected here.

Table 3-4 Grid test results of different grid densities for on-blast cycle

Hot blast temperature (Time step= 60 sec)	
Grid Number	RMSE (%)
1027246	1.3
1088989	1.3
1324338	1.4
1834332	1.5

Table 3-5 Time step test results for on-blast cycle

Hot blast temperature (Grid number= 1088989)	
Time step (sec)	RMSE (%)
60	1.3
30	1.2
15	1.3

PC of Intel Core 2 with CPU 2.40 GHz, 2.93 GB RAM is applied to carry out the computation, and the absolute convergence criteria for x-velocity, y-velocity, z-velocity, k and epsilon are selected as 0.001, and the one for energy is 0.00001. Then the computational time for a typical simulation in the on-gas cycle needs about 10 hours, whereas it spends about 2 hours for the on-blast cycle simulation.

CHAPTER 4

RESULTS AND DISCUSSION

The main gaseous fuels used in hot-blast stove are the carbon monoxide and hydrogen, which are contained in the gas coming from the blast furnace (BFG). Using BFG as the fuel gas sometimes cannot reach the required hot blast temperature, so it must be enriched by the other fuel gas, such as coke oven gas (COG), with a higher net calorific value. The mixture of BFG and COG is constituted of CH_4, CO and other usual molecules found in hydrocarbon flames. The compositions and corresponding volume fraction of BFG and COG provided by China Steel Cooperation (CSC) are summarized in Table 4-1.

Table 4-1 Respective Compositions (% in volume) of BFG and COG

	BFG	COG
CO_2	23.02	2.13
CO	22.73	7.12
H_2	3.74	56.08
N_2	50.51	6
O_2	0	0.1
CH_4	0	25.78
C_2H_4	0	2.79

From the information provided by CSC, the price of BFG (0.38 NT$/Nm^3) is about 10 times that of COG (3.94 NT$/Nm^3), and the production of COG is much less than BFG. Therefore, if CSC can minimize the usage of COG, it will be able to reduce the operation cost of hot-blast stove greatly that meets the requirement for saving energy. Accordingly, this study conducted a parametric study to change the respective mixing volume flow rates, i.e. heating values, of BFG and COG under a specified fuel mixture supply rate and the excess air ratio. The purpose is to find the optimal mixing proportion between BFG and COG that can achieve the best hot-blast stove efficiency effectively.

Before the parametric study was carried out, a reference case was described in details in Section 4.1 first. The operation process of hot-blast stove can be divided into on-gas and on-blast cycles; hence, the discussion of reference case includes both cycles.

4.1 Reference Case

This study used a commercial package software FLUENT to simulate the on-gas and on-blast cycles of hot-blast stove. The experimental data on April 9th, 2008 provided by CSC are set to be the boundary conditions for FLUENT calculation. The boundary conditions of on-gas and on-blast cycles can be referred in Section 3.4, and they are not repeated here. To ensure the lifetime of hot-blast stove, some operational criteria are specified and they are listed in Table 4-2.

Table 4-2 Operation criteria of hot-blast stove

Dome temperature	950~1350 ℃ (1223~1623 K)
Waste gas temperature	< 350 ℃ (623 K)
Silica temperature	> 600 ℃ (873 K)
Checker temperature	> 700 ℃ (973 K)
Volume flow rate of mixed fuel gas	< 100 kNm^3/h
Oxygen content of waste gas (% in volume)	0.5 ~ 1.0 %

4.1.1 On-Gas Cycle

The mixed fuel gas and combustion air are injected into the inlet1 and inlet2 (see Fig. 2-2 for the locations), respectively, and then they mix and pass through the burner (see Fig. 2-2 for the location) into combustion chamber to burn. During the on-gas cycle, the hot-blast stove is heated by the combustion product gases generated from the combustion chamber of the stove. The combustion products, or waste gases, enter the dome at the top of hot-blast stove and then descend down to go through the beehive regenerative bricks, referred as the checkers, and transfer energy to these checkers simultaneously. After the waste gases transfer energy to the checkers, it is discharged at outlet1 and outlet2 (see Fig. 2-2 for the locations). Therefore, it must simulate the combustion of mixed fuel gas (BFG and COG) and the heat transfer between gas and solid for on-gas cycle. The mixed fuel gas used here is composed of BFG and COG, and the combustible gases in the mixed fuel gas include hydrogen, carbon

monoxide, methane and ethylene. The volume flow rates of BFG and COG in reference case are 80,248 and 1,805Nm^3/h respectively, and the volume flow rate of combustion air is 61,365 Nm^3/h. Here one-step global reactions of hydrogen, carbon monoxide, methane and ethylene, whose reaction rates are finite, are adopted, and the corresponding finite rate expressions are described in Section 2.2.6.

There are two waste gas outlets (outlet1 and outlet2) in the hot-blast stove. The waste gas temperature listed in the experimental data is the temperature that is measured when the waste gases at outlet1 and outlet2 mix. Therefore, the waste gas temperature of simulation mentioned below is using the average waste gas temperature at oulet1 and outlet2.

The simulated velocity, temperature and species distributions of 1^{st}, 25^{th} and 50^{th} minute are displayed in Figs. 4-1 to 4-18, respectively. From Figs. 4-1, 4-2 and 4-3, it can be found that the velocity distributions at 1^{st}, 25^{th} and 50^{th} minute are very similar each other and the maximum velocities occur in the connection pipe. From the temperature distributions at 1^{st}, 25^{th} and 50^{th} minute (Figs. 4-4, 4-5 and 4-6), the highest temperatures occur at combustion chamber and dome, and the temperatures in checker chamber decreases gradually from the top checker (S21) to the bottom one (SF125).

Figures 4-1 to 4-3 show that the gas velocity is accelerated after the product gases leave the burner because the combustion occurs there. Then, it is decreased in the upper part of combustion chamber because the flow is going to turn around there. The gas velocity in the connection pipe is increased again because the flow area there is reduced. Afterward the gas passes through the checker chamber and is slow down due to the

temperature loss to checker wall and the apparent wall friction.

In Figs. 4-4 to 4-6, they show that the temperature of checker chamber is increasing with time because the heat carried by the combustion product gases is transferred to the checkers.

From Figs. 4-7 to 4-18, it can be found that the combustible gases, such as H_2, CO, CH_4 and C_2H_4 have been burnt out completely in the combustion chamber. It is because that the excess air ratio for this reference case is 1.03 and the chemical reactions are all one-step global reactions (no reversible reactions) that can ensure that the mixed fuels can be burnt out completely there.

The particle tracer of on-gas cycle is shown in Fig. 4-19. It shows that the particles do not produce vortex in the combustion and checker chambers, which proves that there is no hot spot produced during on-gas cycle.

The experimental and simulated temperatures of waste gas and dome vary with time are listed in Table 4-4. The RMSE (%) of waste gas and dome temperatures as a function of time between experiment and simulation are 2.0 and 2.3 % respectively, indicating that the predicted temperatures are quite accurate. According to the operation criteria of hot-blast stove, given in Table 4-2, the waste gas temperature should be less than 350 °C (623 K) to ensure that the most part of energy from the combustion product gases can be transferred to the checkers effectively. From the simulation result, it can be seen that the waste gas temperatures are always less than 350 °C (623 K). Besides, the trends of waste gas temperature variations with time in experiment and simulation are the same. The temperature difference between waste gas and checkers

decreases when the energy of waste gas is transferred to the checkers during on-gas cycle. The decrement of temperature difference between waste gas and checkers results in the decrement of heat transfer. Therefore, the waste gas temperature increases gradually with time.

It can be found that the waste gas temperatures of simulation at initial stage are higher than the ones of experiment. The maximum difference is 31 degrees. The discrepancy is mainly resulted from the initial conditions adopted, which are expected to have great influence on the simulation results at the beginning. When the simulation reaches the stable conditions, such as after 20^{th} minute of on-gas cycle, the simulation waste gas temperatures are very close to the experimental ones at outlets.

Table 4-4 Experimental and simulated temperatures of waste gas and dome

	Experiment	Simulation
Waste gas temperature (K)	501~562	532~568
Dome temperature (K)	1414~1553	1342~1606

4.1.2 On-Blast Cycle

Ten minutes after the end of on-gas cycle, the cold blast (air) is started to inject into the inlet3 (see Fig. 2-2 for the location), and then the cold air is heated as it flows upward through the checkers into the dome. After that, the heated cold-blast (hot blast) proceeds into the combustion chamber before it exhausts from the hot-blast stove through the valve. After leaving the hot-blast stove, the hot blast will mix with the cold air to achieve the

assigned temperature for the blast furnace. Therefore, it has to simulate the heat transfer between gas and solid for on-blast cycle. The volume flow rate of combustion air in reference case is 157,608 Nm^3/h.

The simulated velocity and temperature distributions of 1^{st}, 30^{th} and 60^{th} minute are displayed in Figs. 4-20 to 4-25. From Figs. 4-20, 4-21 and 4-22, it can be found that the velocity distributions of 1^{st}, 30^{th} and 60^{th} minute are very similar each other and the maximum velocities occur in the connection pipe. From the temperature distributions of 1^{st}, 30^{th} and 60^{th} minute (Figs. 4-23, 4-24 and 4-25), the highest temperatures occur at combustion chamber and dome, and the temperatures in checker chamber decrease gradually from the top checker (S21) to the bottom one (SF125).

In Figs. 4-20 to 4-22, the gas velocity is decreased when it ascends through the checker chamber due to the wall friction. Of course, the decelerated flow has enough time to absorb heat from the checkers. Then the gas velocity in the connection pipe is increased because the flow area there is decreased. Afterward, the gas descends down through the combustion chamber and the gas velocity is decreased. After that, the gas is discharged through the hot blast valve, and the gas velocity is increased because the flow area there is decreased. In addition, the gas velocity in combustion chamber is faster than that in checker chamber due to the higher temperature in combustion chamber. In Figs. 4-23 to 4-25, they show that the temperature of checker chamber is decreasing with time because the energy of checkers is transferred to the gas. In the meantime, the temperature of combustion chamber is decreasing with time because of the continuous supply of cold blast.

The experimental and simulated temperatures of dome and hot blast

at outlet3 (see Fig. 2-2 for the location) as a function of time are listed in Table 4-5. The RMSE (%) of dome and hot blast temperatures as a function of time between experiment and simulation are 1.2 and 1.3 % respectively, indicating that the forecasted temperatures are quite proper. The trends of hot blast temperature variations with time are the same in both experiment and simulation. The cold blast that injected into the inlet3 absorbs the energy from checkers and becomes the hot blast to be supplied into blast furnace. After that, the temperature of checker chamber decreases, and then the energy of checkers transferred to the cold blast are gradually decreased. Therefore, the hot blast temperature at outlet3 is reducing with time. In addition, it can be found that the end hot blast temperatures of experiment drop quickly, which is caused by an increment of volume flow rate of cold blast. In real operation, there are two hot-blast stoves supplying hot blast to the blast furnace during on-blast cycle, but one of them will stop supplying and change to on-gas cycle at the last 10 minutes of on-blast cycle. Therefore, the other one must increase the volume flow rate of cold blast to supply enough hot blast to the blast furnace, leading to a temperature drop. However, the volume flow rate of cold blast in the simulation process is kept constant, therefore, the end hot blast temperatures decrease gradually due to the decrement of energy supply from checkers. From the information provided by CSC, it can be known that the average hot blast temperature supplied into blast furnace is 1180 °C (1453 K) generally.

Table 4-5 Experimental and simulated temperatures of hot blast and dome

	Experiment	Simulation
Hot blast temperature (K)	1362~1481	1400~1500
Dome temperature (K)	1428~1527	1425~1491

4.2 Parametric Study

After the reference case was completed, a parametric study was conducted to analyze the influence of the heating value of mixed fuel gas, the volume flow rate of mixed fuel gas, and the excess air ratio on the operation process of hot-blast stove.

4.2.1 Effect of Heating Value of Mixed Fuel Gas

In this part, cases to be simulated and discussed are that the proportion between BFG and COG in the mixed fuel gas is changed. In other words, these cases vary the heating values of mixed fuel gas. There are three cases being simulated here: (1) BFG = 82048 Nm^3/h, COG = 1805 Nm^3/h; (2) BFG = 82589.5 Nm^3/h, COG = 1263.5 Nm^3/h; (3) BFG = 83853 Nm^3/h.

Figures 4-26 to 4-28 show the predicted velocity and temperature distributions in the end of the typical on-gas cycle. The maximum gas velocities in these three cases all occur in the connection pipe, and they are 94, 92 and 86 m/s respectively. The maximum gas velocity is thus a direct function of the fraction of COG in the mixed fuel gas. The highest equilibrium temperatures in these three cases all occur in the combustion chamber, and they are 2031, 2016 and 1974 K respectively. The highest

equilibrium temperature is thus a direct function of the fraction of COG in the mixed fuel gas as well. These results indicate that the heating value of COG is higher than that of BFG, however, it cannot just use high heating value gas (COG) as the fuel gas because of cost and production.

Figures 4-29 to 4-31 present the predicted velocity and temperature distributions in the end of the typical on-blast cycle. They can be seen that the velocity distributions in these three cases are very similar. The maximum gas velocities are at the exit of hot blast because the flow area is smallest and the temperature is highest there.

The comparisons of waste gas and hot blast temperatures as a function of time for these three cases are given in Figs. 4-32 and 4-33.

The waste gas, dome temperatures and oxygen contents of waste gas (% in volume) during on-gas cycle in these three cases are listed in Table 4-6. It shows that the waste gas temperatures as a function of time in these three cases are all less than 350 °C (623 K), indicating that the most part of energy from fuel gas combustion has been transferred to the checkers effectively. The dome temperatures vary with time in these three cases all fit in the operation criteria of hot-blast stove to ensure the structure not to be destroyed. The oxygen contents of waste gas (% in volume) change with time in these three cases are all less than 0.3 % so that the complete combustion is ensured.

Table 4-6 Waste gas and dome temperatures and oxygen contents of waste gas (% in volume) for different BFG/COG ratios

	Dome temperature (K)	Waste gas temperature (K)	Oxygen content of waste gas (% in volume)
BFG = 82048 Nm^3/h COG = 1805 Nm^3/h	1342~1606	532~568	0.19~0.23
BFG = 82589.5 Nm^3/h COG = 1263.5 Nm^3/h	1340~1596	532~567	0.21~0.25
BFG = 83853 Nm^3/h	1335~1575	532~565	0.21~0.25

Huang et al. [16] conducted a research about the effects of preheating and operation conditions on combustion in a porous medium. In this article, it mentioned that the temperatures of combustion chamber reach to different stable values as time proceeds, implying that they are the characteristics of the stable combustion.

In order to confirm the combustion process whether is stable or not, this study sets three measuring points (lower, middle and upper) in the combustion chamber (see Fig. 4-34) for the examination purpose. In Figs. 4-35 to 4-37, they show that the temperatures of measuring points in the combustion chamber all reach stable values. Therefore, the combustion processes in these three cases are stable.

In Table 4-7, the dome and average hot blast temperatures during on-blast cycle in these three cases are listed. The dome temperatures vary with time in these three cases all conform to the operation criteria to

ensure the structure not to be destroyed. The average hot blast temperature decreases with a decrease of the proportion of COG in the mixed fuel gas. The one in the case that the quantity of COG decreases 30 % (BFG = 82589.5 Nm^3/h, COG = 1263.5 Nm^3/h) is still above 1180°C (1453K), therefore, this case is practicable to reduce operation cost. However, the one in the case using 100% BFG (BFG = 83853 Nm^3/h) as the fuel gas is below 1180°C (1453K), therefore, the operation in this case is not feasible.

Table 4-7 Dome and average hot blast temperature for different BFG/COG ratios

	Dome temperature (K)	Average hot blast temperature (K)
BFG = 82048 Nm^3/h COG = 1805 Nm^3/h	1425~1491	1475
BFG = 82589.5 Nm^3/h COG = 1263.5 Nm^3/h	1420~1483	1466
BFG = 83853 Nm^3/h	1402~1465	1450

4.2.2 Effect of Volume Flow Rate of Mixed Fuel Gas

In this part, cases to be simulated and discussed are that the volume flow rate of mixed fuel gas is changed. There are three cases being simulated here: (1) BFG = 82048 Nm^3/h, COG = 1805 Nm^3/h; (2) BFG = 73843.2 Nm^3/h, COG = 1624.5 Nm^3/h; (3) BFG = 65638.4 Nm^3/h, COG = 1444 Nm^3/h.

Figures 4-38 to 4-40 show the predicted velocity and temperature distributions in the end of the typical on-gas cycle. The maximum gas velocities in these three cases all occur in the connection pipe, and they are 94, 84 and 75 m/s, respectively. The result indicates that the maximum gas velocity is influenced by the volume flow rate of mixed fuel gas very much. The greater volume flow rate of mixed fuel gas results in the faster gas velocity. The highest equilibrium temperatures in these three cases all occur in the combustion chamber, and they are 2031, 2032 and 2032K, respectively. It implies that the highest equilibrium temperature is almost not influenced by the volume flow rate of mixed fuel gas.

In Figs. 4-41 to 4-43, they are the predicted velocity and temperature distributions in the end of the typical on-blast cycle. The velocity distributions in these three cases are found very similar, and the maximum gas velocities all occur at the exit of hot blast because the flow area is smallest and the temperature is highest there.

The comparisons of waste gas and hot blast temperatures as a function of time in these three cases are shown in Figs. 4-44 and 4-45.

Table 4-8 lists the waste gas, dome temperatures and oxygen contents of waste gas (% in volume) during on-gas cycle in these three cases. It indicates that the waste gas temperatures as a function of time in these three cases are all less than 350 °C (623 K). This result shows that the most portion of energy from fuel gas combustion has been delivered to the checkers usefully. The dome temperatures vary with time in these three cases all tally with the operation criteria of hot-blast stove to ensure the structure not to be destructed. The oxygen contents of waste gas (% in volume) change with time in these three cases are all less than 0.3 % so

that the complete combustion is ensured.

In Figs. 4-46 to 4-48, they show that the temperatures of measuring points in the combustion chamber all achieve stable values. Therefore, the combustion processes in these three cases are stable.

In Table 4-9, the dome and average hot blast temperatures during on-blast cycle in these three cases are listed. The dome temperatures vary with time in these three cases all conform to the operation criteria to ensure the structure not to be destroyed. The average hot blast temperature decreases with a decrease of the volume flow rate of mixed fuel gas. Thus, the hot blast temperature is affected by the volume flow rate of mixed fuel gas. The more volume flow rate is, the more energy transferred to the checkers is. Therefore, the more volume flow rate of mixed fuel gas will produce the higher hot blast temperature. The one in the case that the volume flow rate of mixed fuel gas decreases 10 % (BFG = 73843.2 Nm^3/h and COG = 1624.5 Nm^3/h) is above 1180°C (1453 K), but, it is just above 3 degrees, therefore, the case that the volume flow rate of mixed fuel gas decreases 5 % is recommended to be workable. The one in the case that the volume flow rate of mixed fuel gas decreases 20 % (BFG = 65638.4 Nm^3/h and COG = 1444 Nm^3/h) is below 1180°C (1453 K), therefore, this case is not practicable.

Table 4-8 Waste gas, dome temperatures and oxygen content of waste gas (% in volume) for different volume flow rates of mixed fuel gas

	Dome temperature (K)	Waste gas temperature (K)	Oxygen content of waste gas (% in volume)
BFG = 82048 Nm^3/h COG = 1805 Nm^3/h	1342~1606	532~568	0.19~0.23
BFG = 73843.2 Nm^3/h COG = 1624.5 Nm^3/h	1337~1596	532~562	0.17~0.21
BFG = 65638.4 Nm^3/h COG = 1444 Nm^3/h	1333~1585	532~555	0.14~0.19

Table 4-9 Dome and average hot blast temperature for different volume flow rates of mixed fuel gas

	Dome temperature (K)	Average hot blast temperature (K)
BFG = 82048 Nm^3/h COG = 1805 Nm^3/h	1425~1491	1475
BFG = 73843.2 Nm^3/h COG = 1624.5 Nm^3/h	1409~1474	1456
BFG = 65638.4 Nm^3/h COG = 1444 Nm^3/h	1392~1456	1438

4.2.3 Effect of Excess Air Ratio

In this part, the effect of excess air ratio is investigated. There are

three cases being simulated here: (1) Excess air ratio = 1.03; (2) Excess air ratio = 1.05; (3) Excess air ratio = 1.1.

Figures 4-49 to 4-51 show that the predicted velocity and temperature distributions in the end of the typical on-gas. The maximum gas velocities in these three cases all occur in the connection pipe, and all of them are 94 m/s. Apparently, the maximum gas velocity is not affected by the excess air ratio. The highest equilibrium temperatures in these three cases all occur in the combustion chamber, and they are 2031, 2033 and 2031K, respectively. This result also indicates that the highest equilibrium temperature is not influenced by the excess air ratio very much.

In Figs. 4-52 to 4-54, they are the predicted velocity and temperature distributions in the end of the typical on-blast cycle. It can be seen that the velocity distributions in these three cases are very similar. The maximum gas velocity occurs at the exit of hot blast because the maximum temperature and minimum area are occurred there.

The comparisons of waste gas and hot blast temperatures as a function of time in these three cases are shown in Figs. 4-55 and 4-56.

The waste gas and dome temperatures and oxygen contents of waste gas (% in volume) during on-gas cycle in these three cases are listed in Table 4-10. Table 4-10 indicates that the waste gas temperatures as a function of time in these three cases are all less than 350 °C (623 K). This result shows that the most part of energy from fuel gas combustion has been transferred to the checkers effectually. The dome temperatures as a function of time in these three cases all fit in the operation criteria of hot-blast stove to ensure the structure not to be destroyed. The oxygen contents of waste gas (% in volume) as a function of time in these three

cases are all less than 0.9 % so that the complete combustion is ensured.

In Figs. 4-57 to 4-59, they show that the temperatures of measuring points in the combustion chamber all get up to stable values. Therefore, the combustion processes in these three cases are stable.

Table 4-10 Waste gas, dome temperatures and oxygen content of waste gas (% in volume) for different excess air ratio

	Dome temperature (K)	Waste gas temperature (K)	Oxygen content of waste gas (% in volume)
Excess air ratio = 1.03	1342~1606	532~568	0.19~0.23
Excess air ratio = 1.05	1341~1600	532~568	0.40~0.45
Excess air ratio = 1.01	1339~1588	532~569	0.81~0.87

Table 4-11 lists the dome and average hot blast temperatures during on-blast cycle in these three cases. The dome temperatures change with time in these three cases all fit in the operation criteria to ensure the structure not to be destroyed. The average hot blast temperatures in these three cases are all above 1180°C (1453 K). The results show that too much combustion air results in the decrease of average hot blast temperature due to the cooling effect, therefore, the cases that increase the excess air ratio are not feasible.

Table 4-11 Dome and average hot blast temperature for different excess air ratios

	Dome temperature (K)	Average hot blast temperature (K)
Excess air ratio = 1.03	1425~1491	1475
Excess air ratio = 1.05	1424~1487	1470
Excess air ratio = 1.1	1418~1480	1464

CHAPTER 5
CONCLUSIONS AND RECOMMENDATION

This thesis utilized a commercial package software, FLUENT, to simulate on-gas and on-blast cycles of the hot-blast stove and found out the best mixing proportion between BFG and COG to promote the hot-blast stove efficiency and minimize the usage of COG.

At first, the simulation results for on-gas cycle of the reference case described in Section 4.1 compare with the experimental data. It can be found that the waste gas temperatures of simulation at initial stage are higher than the ones of experiment. The difference is 31 degrees. The discrepancy is mainly resulted from the initial conditions adopted, which are expected to have great influence on the simulation results at the beginning. When the simulation reaches the stable conditions, such as after 20^{th} minute of on-gas cycle, the simulation waste gas temperatures are very close to the experimental ones at outlets. The RMSE (%) of waste gas temperatures as a function of time between experiment and simulation is 2.0 %, indicating that the predicted waste gas temperatures are quite accurate. The trends of waste gas temperature variations in experiment and simulation are both increasing with time gradually.

The simulation results for on-blast cycle of the reference case described in Section 4.1 compare with the experimental data. It can be found that the end hot blast temperatures of experiment drop quickly, which is caused by an increment of volume flow rate of cold blast. In real operation, there are two hot-blast stoves supplying hot blast to the blast

furnace during on-blast cycle, but one of them will stop supplying and change to on-gas cycle at the last 10 minutes of on-blast cycle. Therefore, the other one must increase the volume flow rate of cold blast to supply enough hot blast to the blast furnace, leading to a temperature drop. However, the volume flow rate of cold blast in the simulation process is kept constant, therefore, the end hot blast temperatures decrease gradually due to the decrement of energy supply from checkers. The RMSE (%) of hot blast temperatures as a function of time between experiment and simulation is 1.2 %, indicating the predicted hot blast temperatures are quite accurate. The trends of hot blast temperature variations in experiment and simulation are both decreasing with time gradually.

The results about reference case and parametric studies are summarized as follows:

(1) There is no hot spot produced during on-gas cycle in the reference case.

(2) The on-gas cycles of cases about parametric studies are all stable combustion.

(3) When the quantity of COG in mixed fuel gas decreases 30 %, the average hot blast temperature decreases about 9 degrees, however, it is still above 1180 ℃ (1453 K), therefore, this case is practicable.

(4) When the mixed fuel gas is using BFG only, the average hot blast is below 1180 ℃ (1453 K), therefore, this case is not feasible.

(5) When the volume flow rate of mixed fuel gas decreases 10 %, the average hot blast temperature is reduced about 19 degrees, however, it is still above 1180 ℃ (1453 K), but it is just 3 degrees, therefore, the case that the volume flow rate of mixed fuel gas decreases 5 % is

recommended to be workable.

(6) When the volume flow rate of mixed fuel gas decreases 20 %, the average hot blast is below 1180 ℃ (1453 K), therefore, this case is not practicable.

(7) The increment of excess air ratio results in the decrement of average hot blast temperature due to the cooling effect. Therefore, the increment of excess air ratio is not feasible.

Based on the above-mentioned conclusions and shortcomings, here one recommendation is addressed for possible solutions.

(1) Establishing a data base about changing the heating value and volume flow rate of mixed fuel gas to reduce the experimental times in the scene of hot-blast stove operation.

REFERENCE

[1] Y. Zhang, Y. D. He, S. Q. Li, Y. S. Shen, X. Y. Huang, Q. H. Tang, H. X. Li and M. Wang, “Mathematical Model of Combustion Blunt Annular Ceramic Burner”, J. Iron & Steel Res. , Int., Vol. 8, No. 2, 2001.

[2] Y. S. Chen, Y. D. He, Z. He, G. L. Sun and Z. Z. Hao, “Simulation Study on Flame Shape of Combustion of Ceramic-grid Burners”, Industrial Furnace, Vol. 28, No.5, Sep.2006.

[3] K. R. Muske, J. W. Howse, G. A. Hansen and D. J. Cagliostro, “Model-based Control of a Thermal Regenerator. Part 1: Dynamic Model”, Computers and Chemical Engineering, pp. 2519-2531, 2000.

[4] O. Gicquel, L. Vervisch, G. Joncquet, B. Labegorre and N. Darabiha, “Combustion of Residual Steel Gases: Laminar Flame Analysis and Turbulent Flamelet Modeling”, Fuel, pp. 983-991, 2003.

[5] G. J. Zhu, Z. Y. Liang, N. Y. Deng and R. Zhong, “Study on Optimum Combustion Techniques of Hot Stoves”, Industrial Furnace, Vol. 27, No. 4, Jul. 2005.

[6] B. Z. Zhang, X. X. Zhang, F. Yu, J. C. Jiao and B. C. Peng, “Numerical Simulations of Gas Combustion and Flow in Kalugin Hot Blast Stove”, Industrial Furnace, Vol. 27, No. 6, Nov. 2005.

[7] D. Andahazy, G. Loffler, F. Winter, C. Feilmayr and T. Burgler, “Theoretical Analysis on the Injection of H_2, CO, CH_4 Rich Gases into the Blast Furnace”, ISIJ Internation, Vol. 45, No. 2, pp. 166-174, 2005.

[8] C. Ellul, M. Pourkashanian and A. Williams, “Numerical

Investigations of Blast Furnace Gas (BFG) and Coke Oven Gas (COG) in Laminar Counter Flow Preheated Air Diffusion Flames", ERRI/ CFD Center, University of Leeds, Leeds United Kingdom LS2 9JT, 2006.

[9] J. Sun, J. Yang, G. Hou and J. Yin, "Estimation of Blast Duration and Coordinated Control Strategy for Hot-Blast-Stove System", IEEE, 2006.

[10] J. Sun, J. Yang, R. Meng and J. Yin, "Case-Based Real-Time Controller and its Application in Combustion Control of Hot Blast Stoves", Proceedings of the 6th World Congress on Intelligent Control and Automation, June 2006.

[11] H. S. Liu and M. Z. Xie, "Working Process Simulation of PM Engine Using a Single-Zone Model", Transations of CSICE, Vol. 25, No. 2, 2007.

[12] Z. G. Zhao and M. Z. Xie, "Numerical Study on the Combustion Process of a Porous Medium Internal Combustion Engine", Transations of CSICE, Vol. 25, No. 4, 2007.

[13] S. J. Wang and R. Sun, "Numerical Investigation of Premixed Combustion in Porous Media", Vol. 25, No. 144, Jul. 2007.

[14] W. S. Fu, K. N. Wang and W. W. Ke, "Heat Transfer of Porous Medium with Random Porosity Model in a Laminar Channel Flow", Journal of the Chinese Institute of Engineers, Vol. 24, No. 4, pp. 431-438, 2001.

[15] S. L. Peng and J. Chou, "The Building and Application of the Current Quarterly Model (CQM) for Taiwan",1999.

[16] Y. Huang, C. Y. H. Chao and P. Cheng, "Effects of Preheating and

Operation Conditions on Combustion in a Porous Medium", International Journal of Heat and Mass Transfer, 2002.

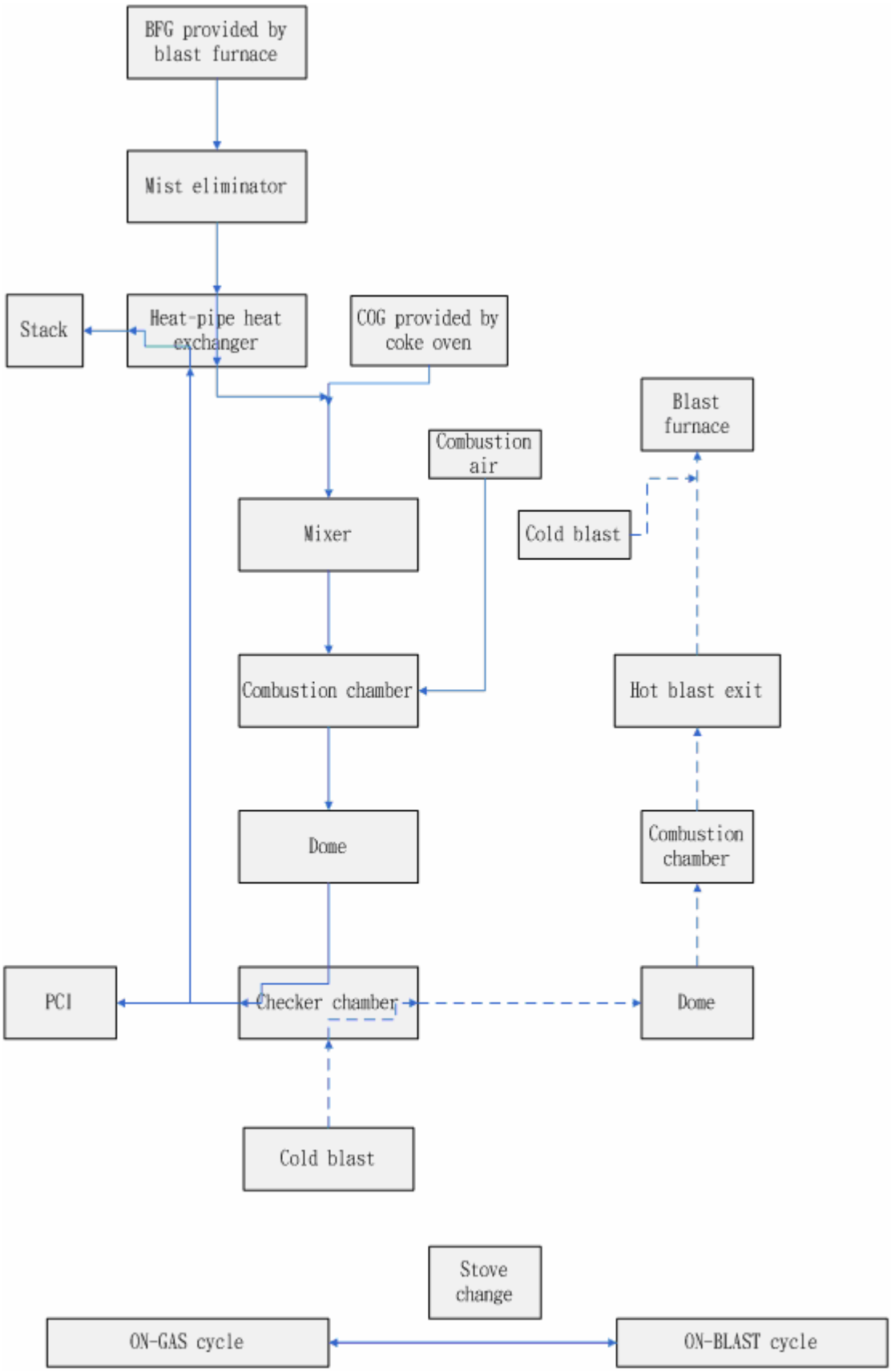

Fig. 1-1 Operation process of hot-blast stove

Fig. 2-1 Hot-blast stove of the China Steel Cooperation

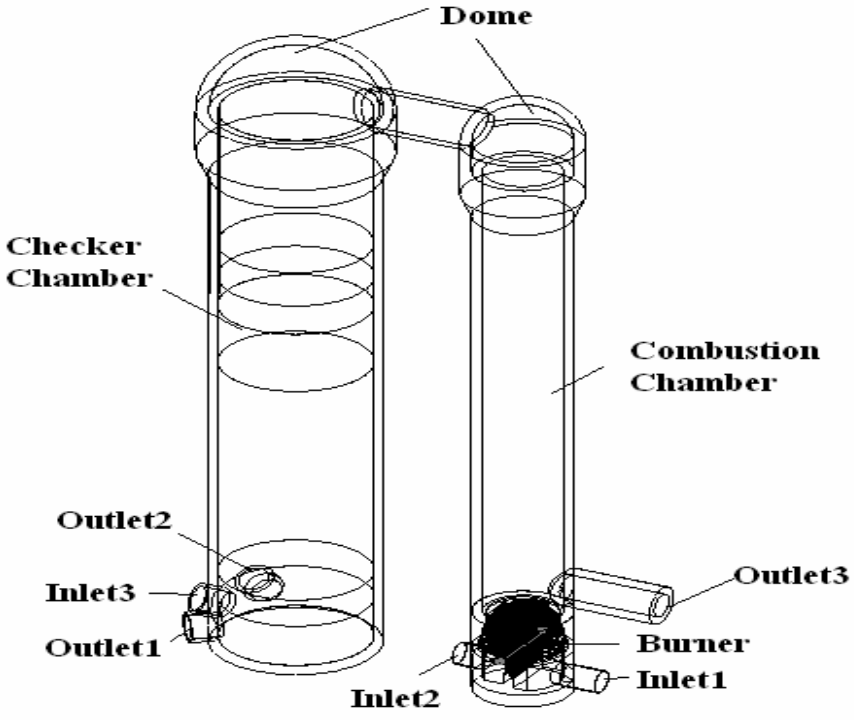

Fig. 2-2 Hot-blast stove's architecture

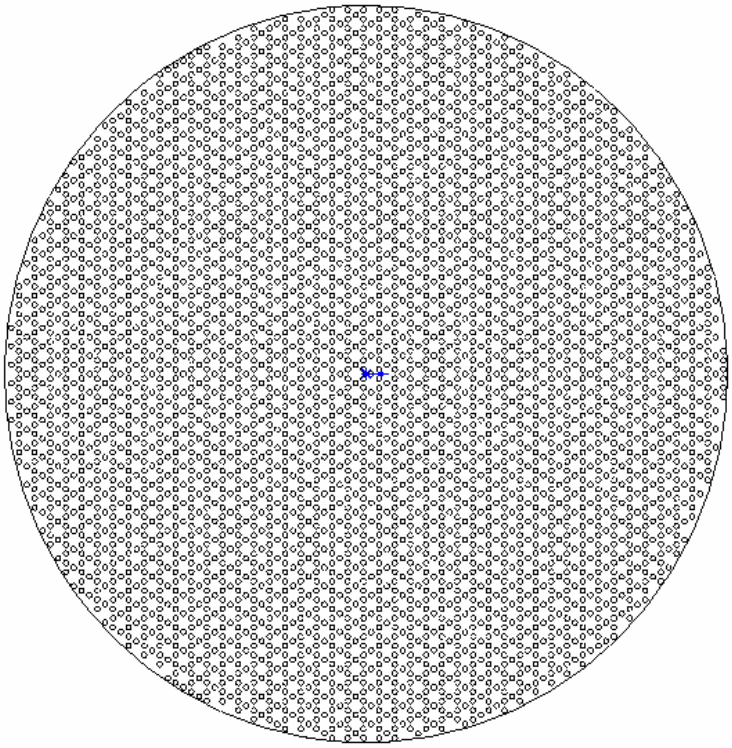

Fig. 2-3 Top view of real checkers

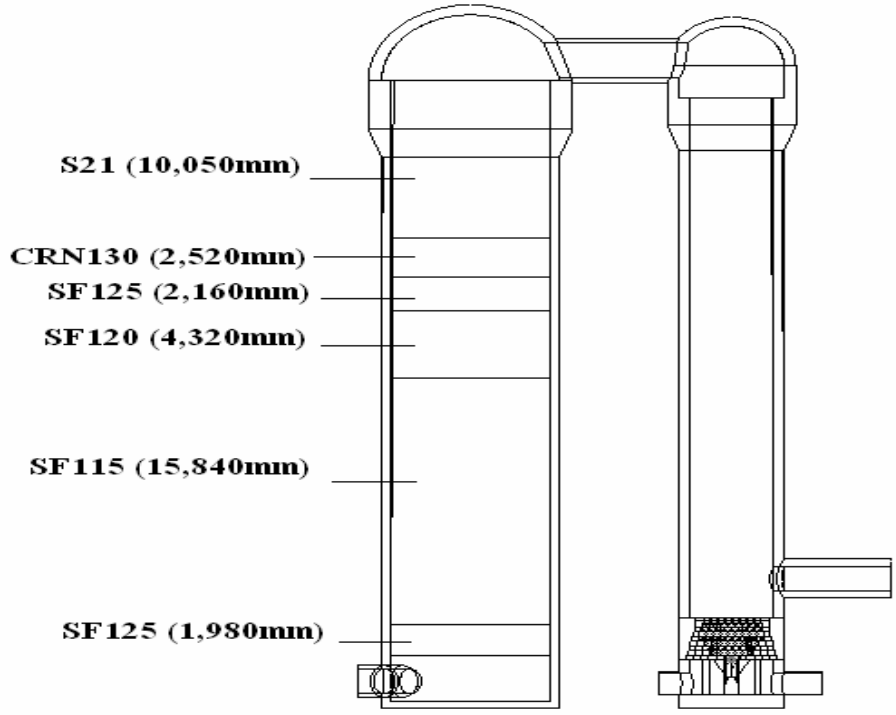

Fig. 2-4 Materials and height of every checker in the hot-blast stove

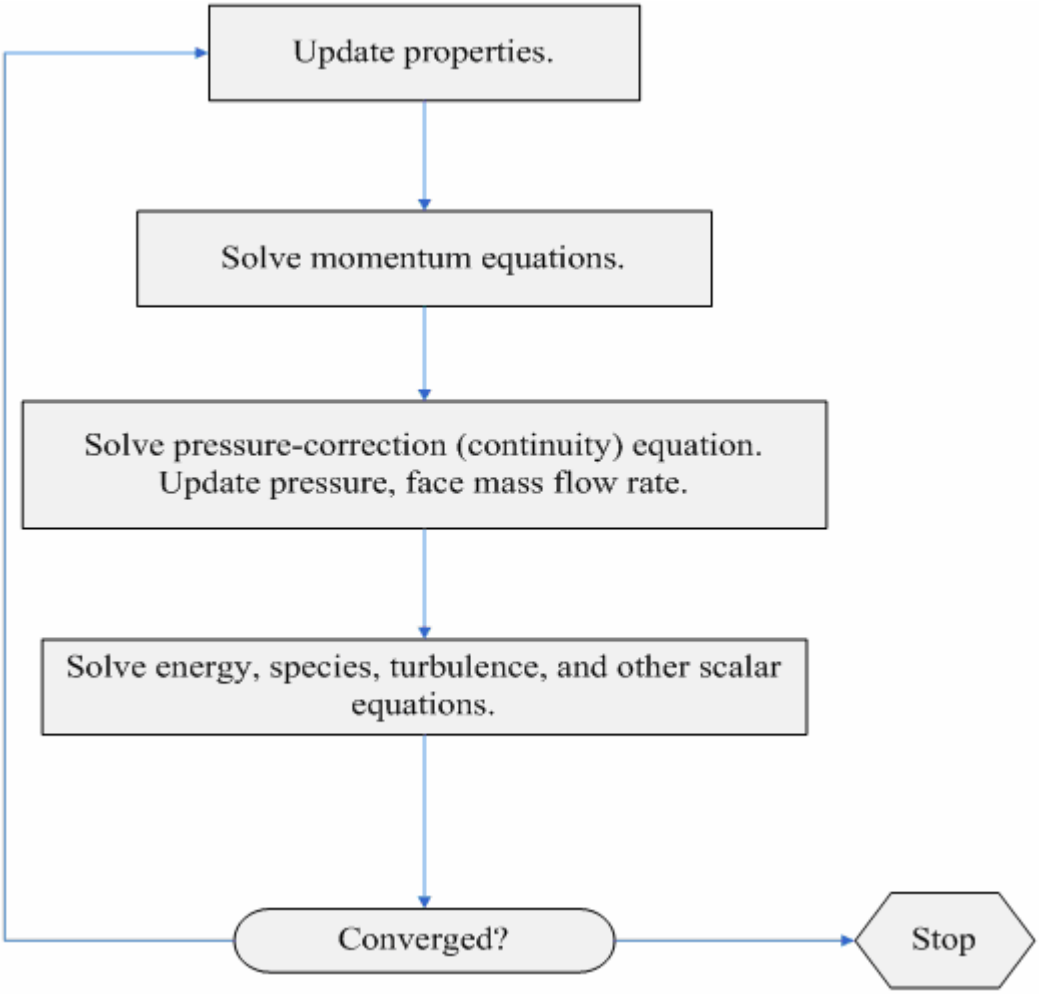

Fig. 3-1 Overview of the segregated solution method

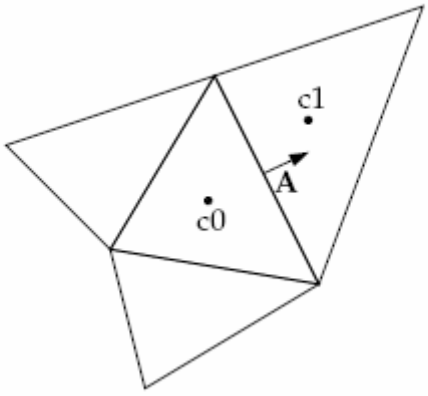

Fig. 3-2 Control volume used to illustrate discretization of a scalar transport equation

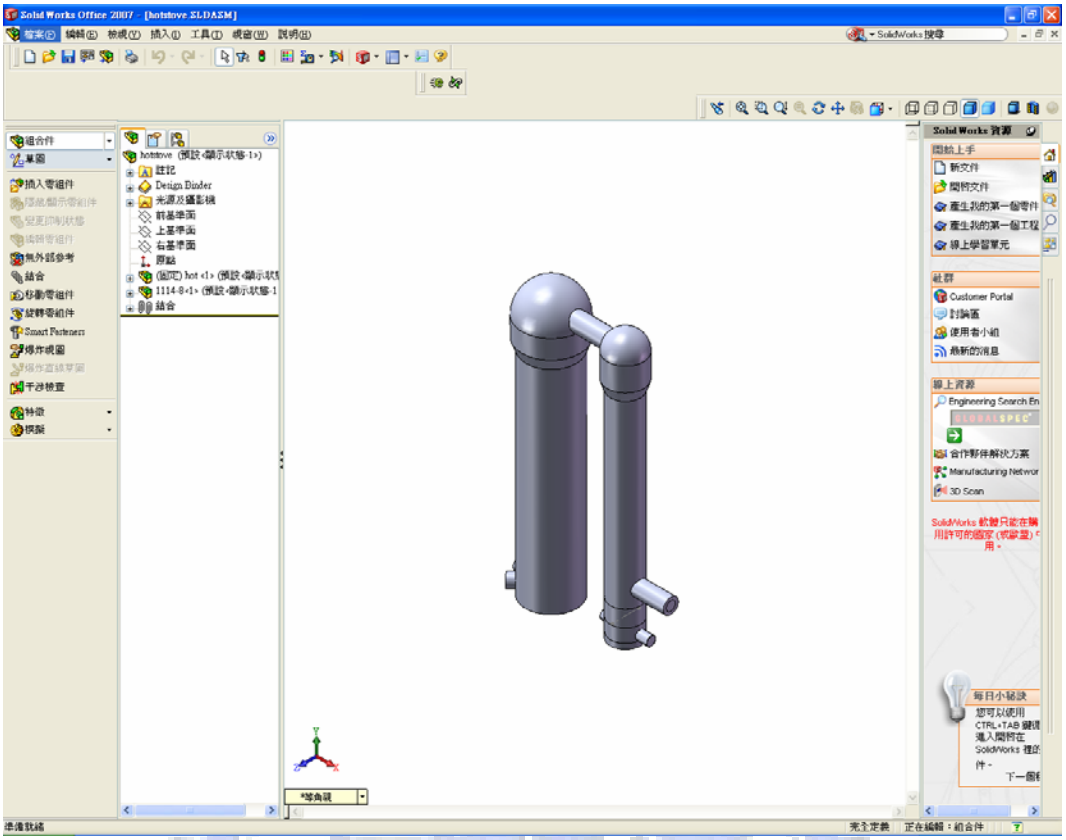

Fig. 3-3 User interface of Solid Works

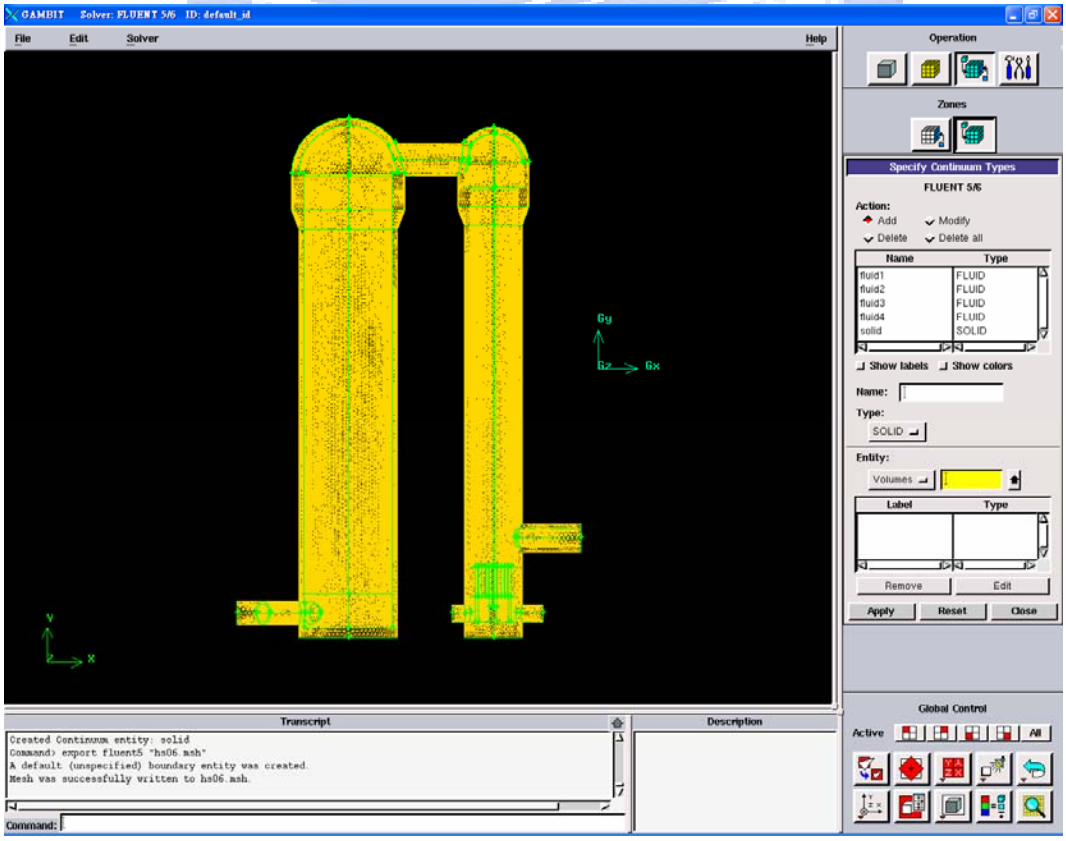

Fig. 3-4 User interface of Gambit

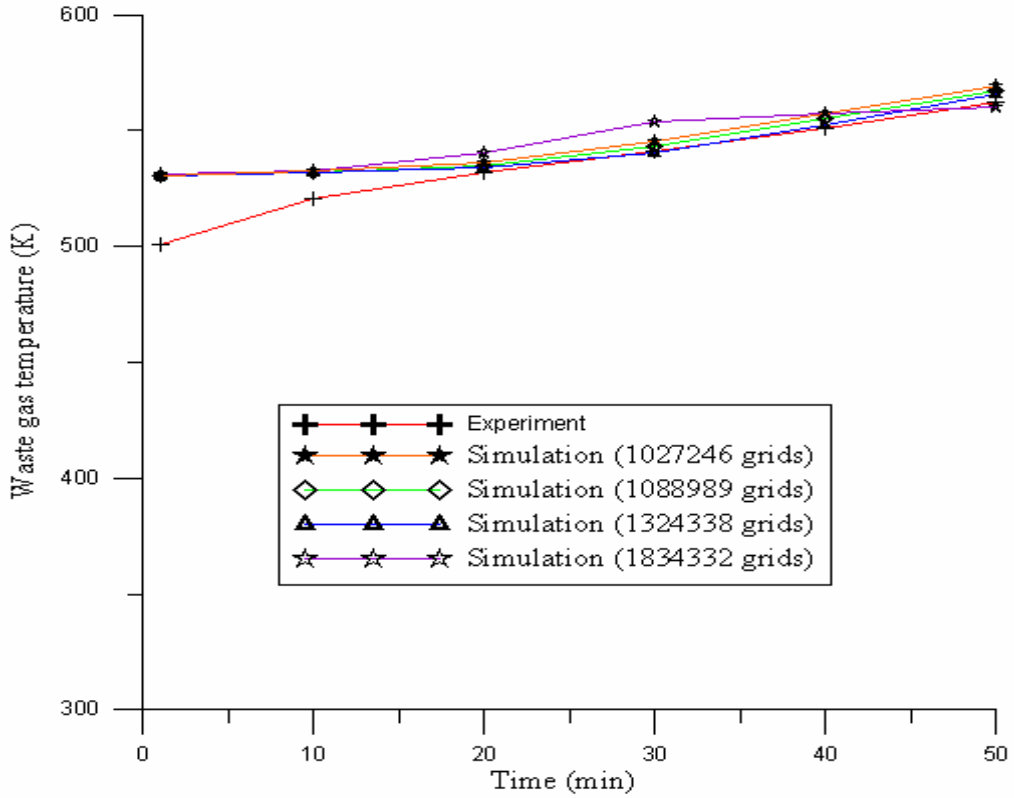

Fig. 3-5 Grid test results of different grid densities for on-gas cycle

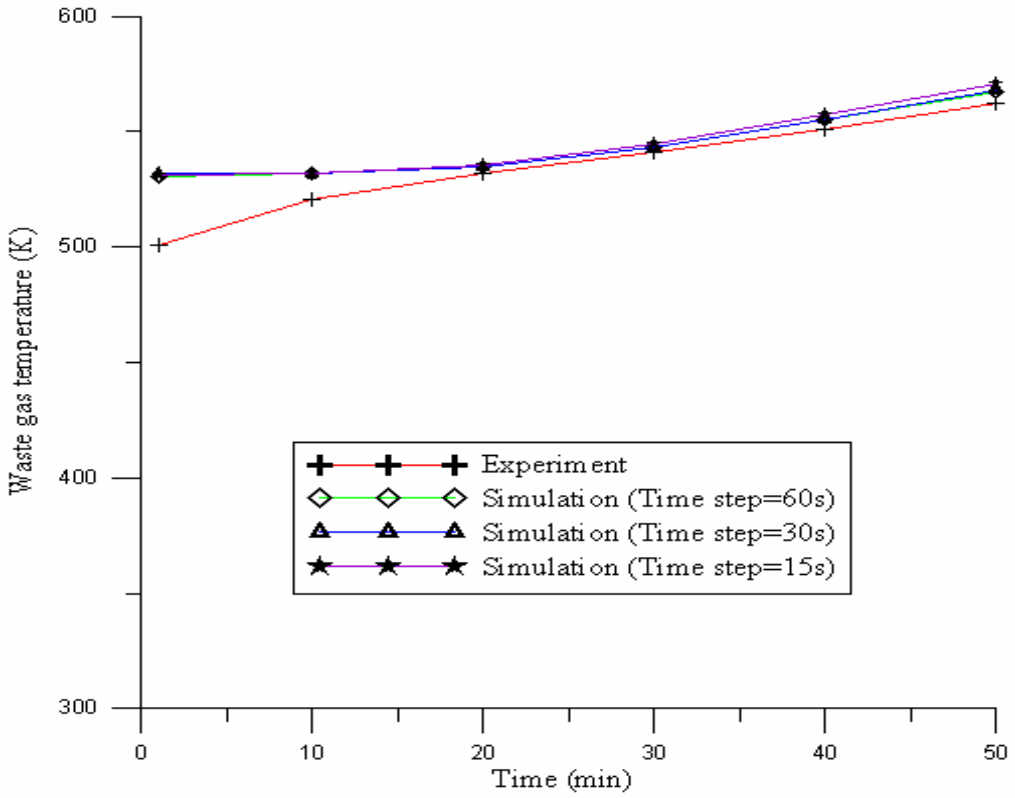

Fig. 3-6 Time step test results for on-gas cycle

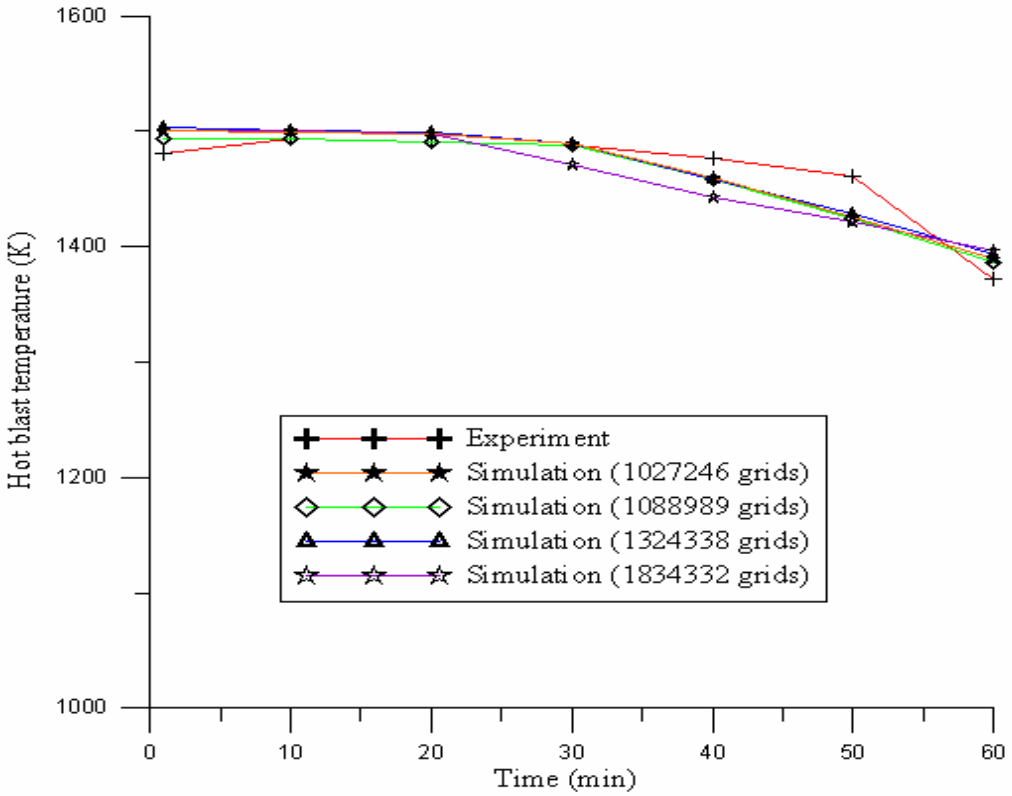

Fig. 3-7 Grid test results of different grid densities for on-blast cycle

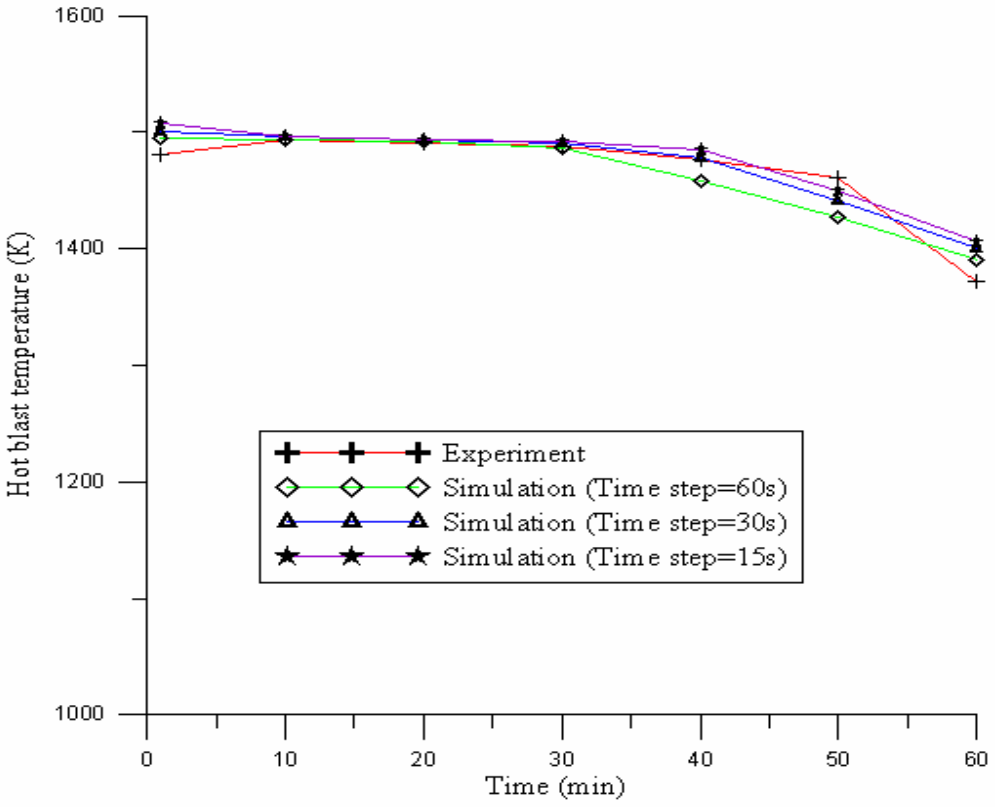

Fig. 3-8 Time step test results for on-blast cycle

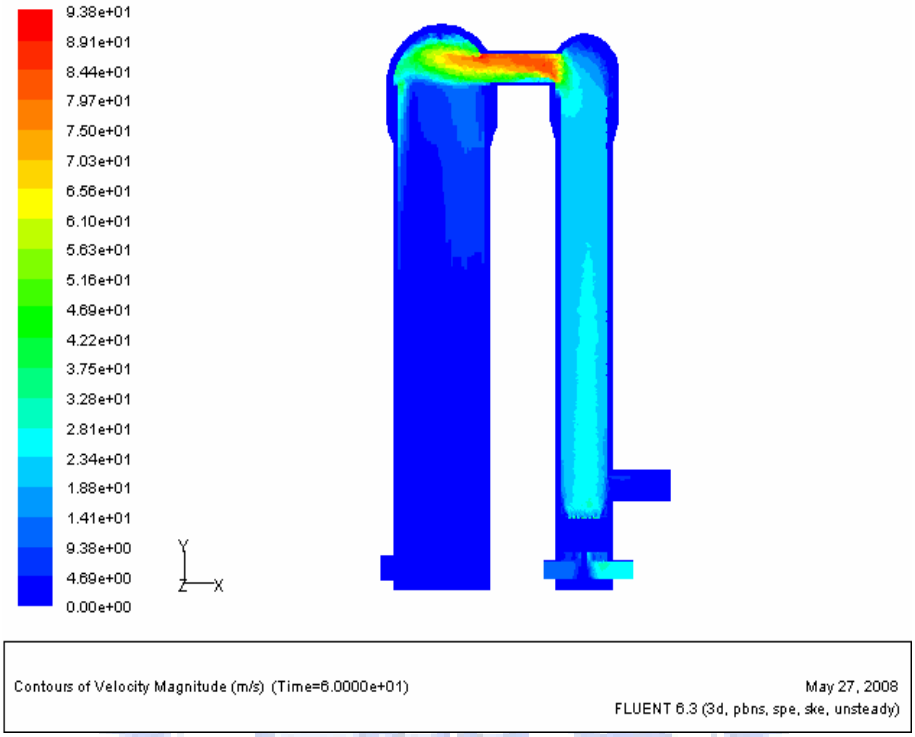

Fig. 4-1 Velocity distribution of 1st minute for the on-gas cycle

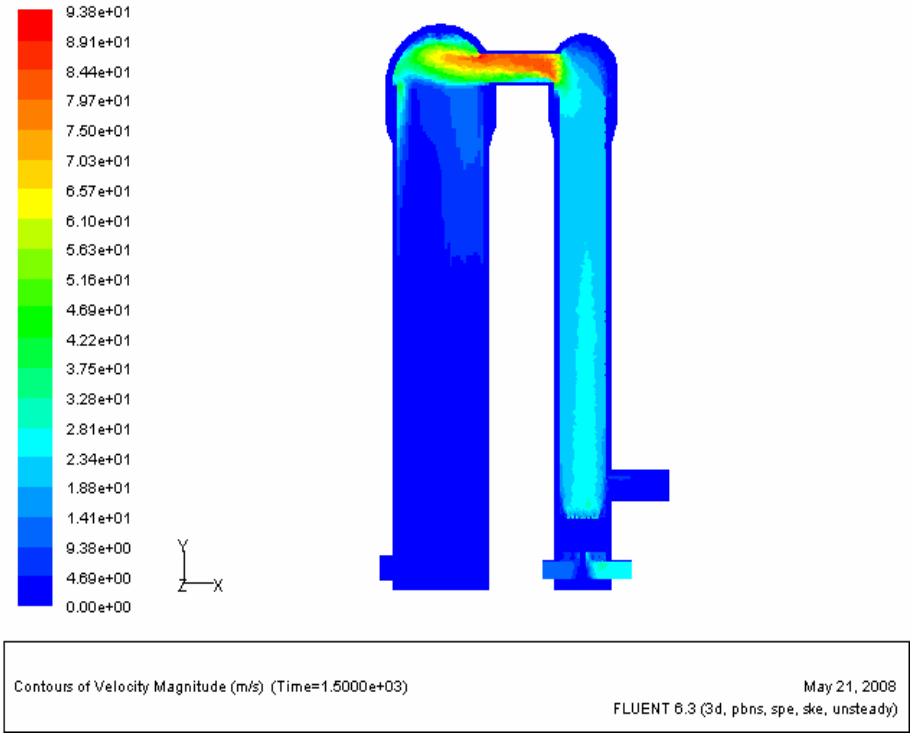

Fig. 4-2 Velocity distribution of 25th minute for the on-gas cycle

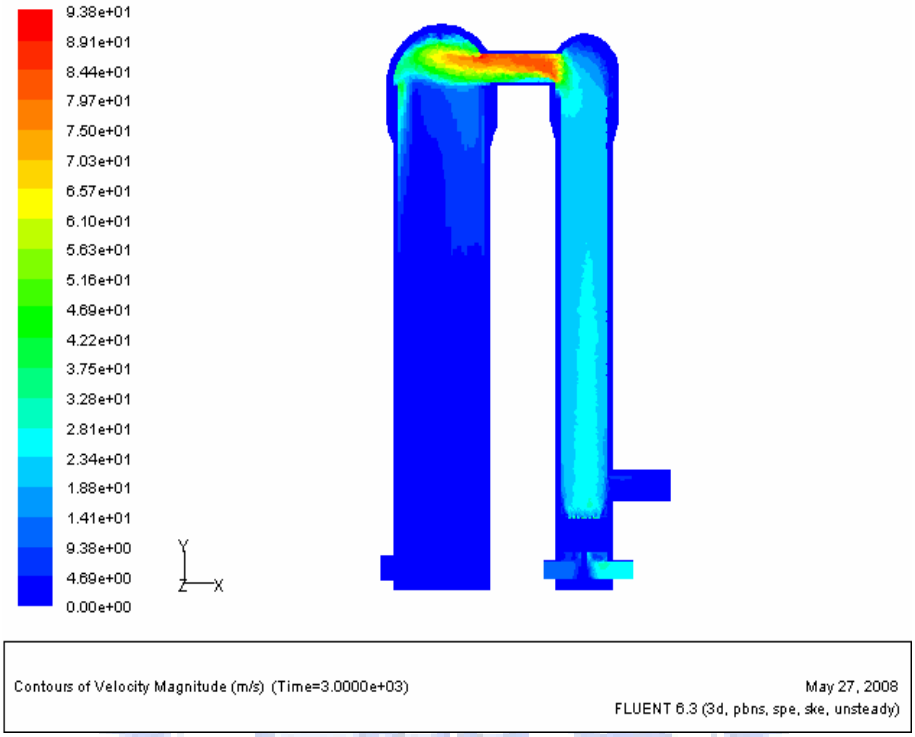

Fig. 4-3 Velocity distribution of 50th minute for the on-gas cycle

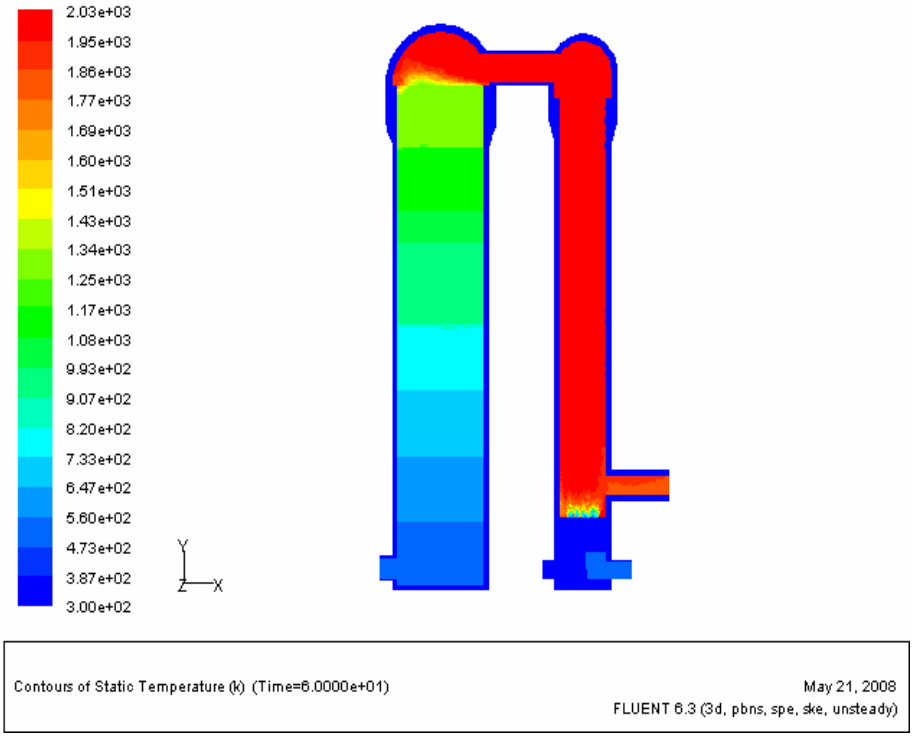

Fig. 4-4 Temperature distribution of 1st minute for the on-gas cycle

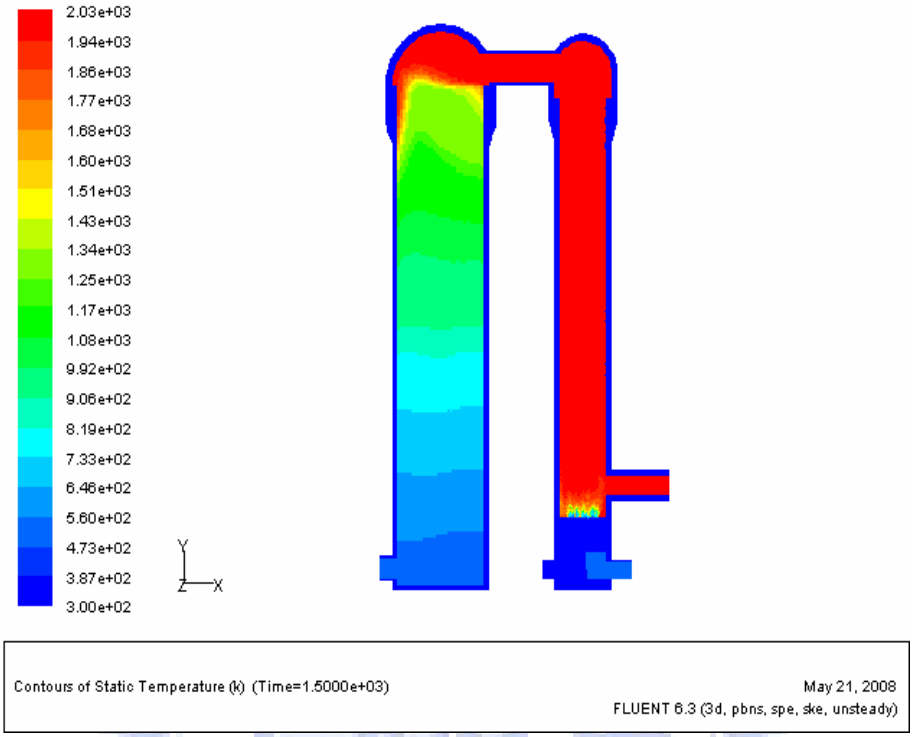

Fig. 4-5 Temperature distribution of 25th minute for the on-gas cycle

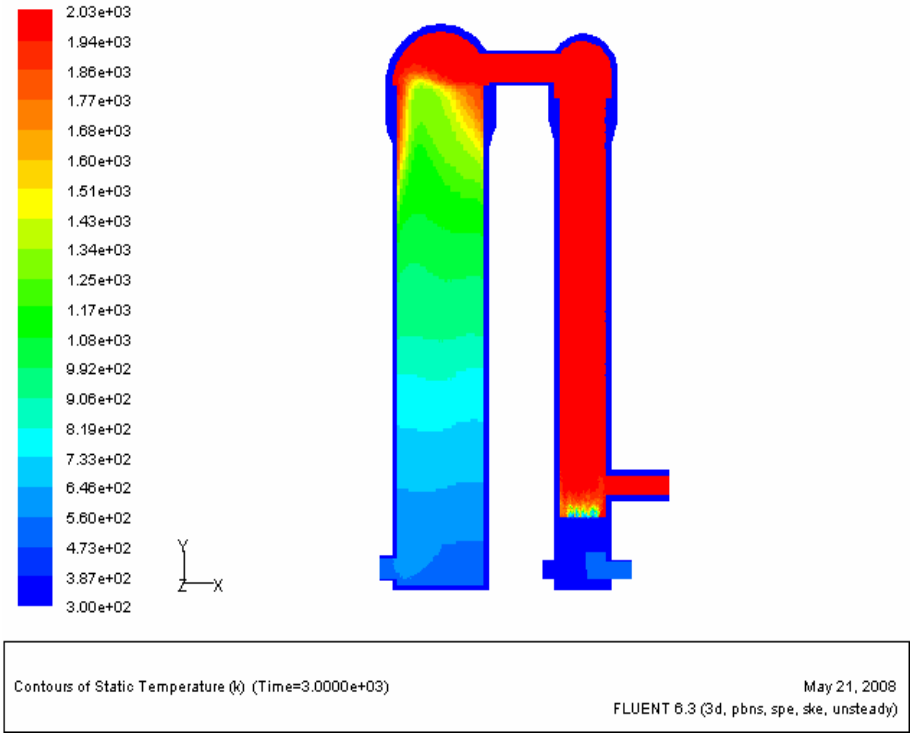

Fig. 4-6 Temperature distribution of 50th minute for the on-gas cycle

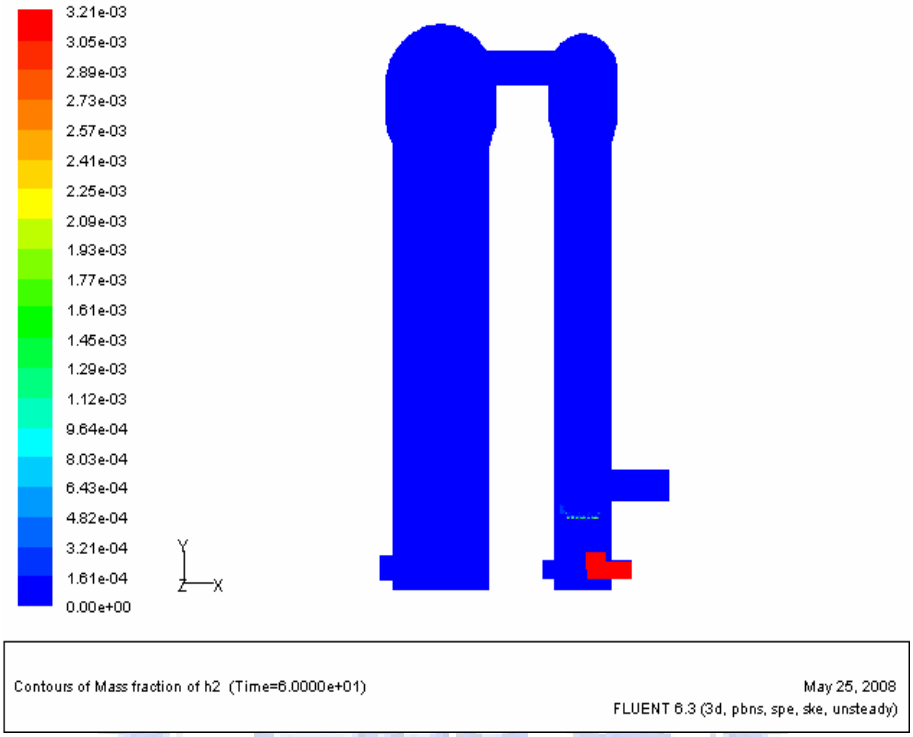

Fig. 4-7 Mass fraction distribution of H_2 of 1st minute for the on-gas cycle

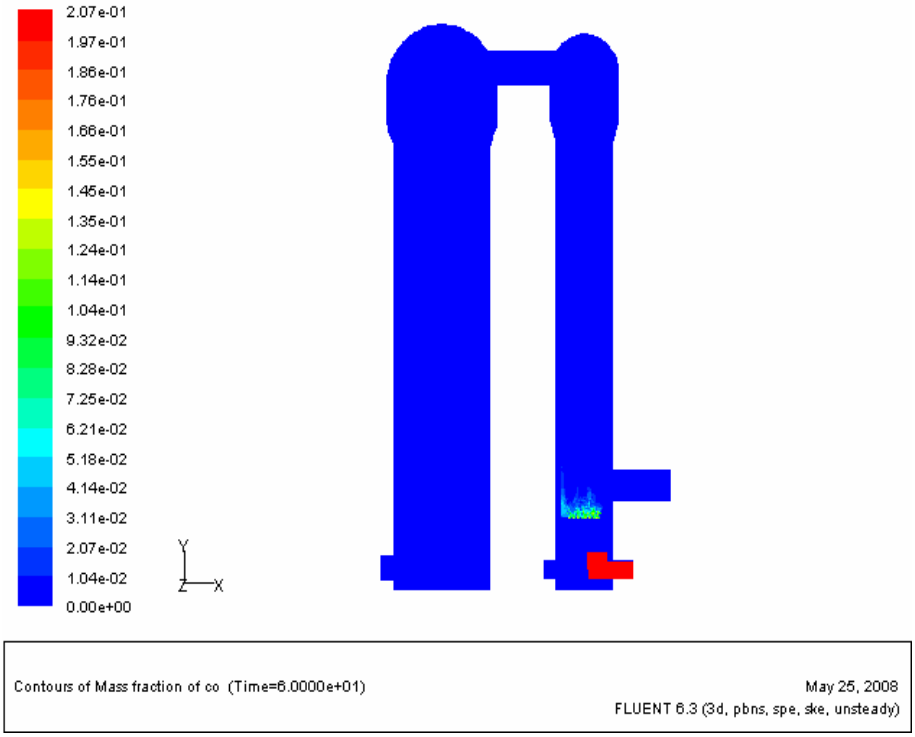

Fig. 4-8 Mass fraction distribution of CO of 1st minute for the on-gas cycle

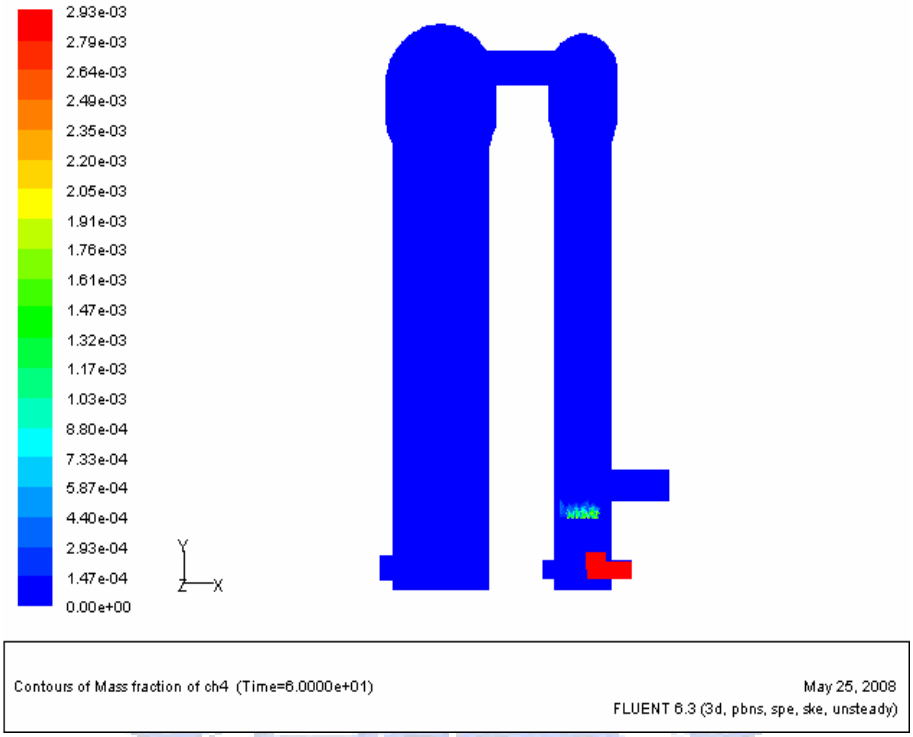

Fig. 4-9 Mass fraction distribution of CH_4 of 1st minute for the on-gas cycle

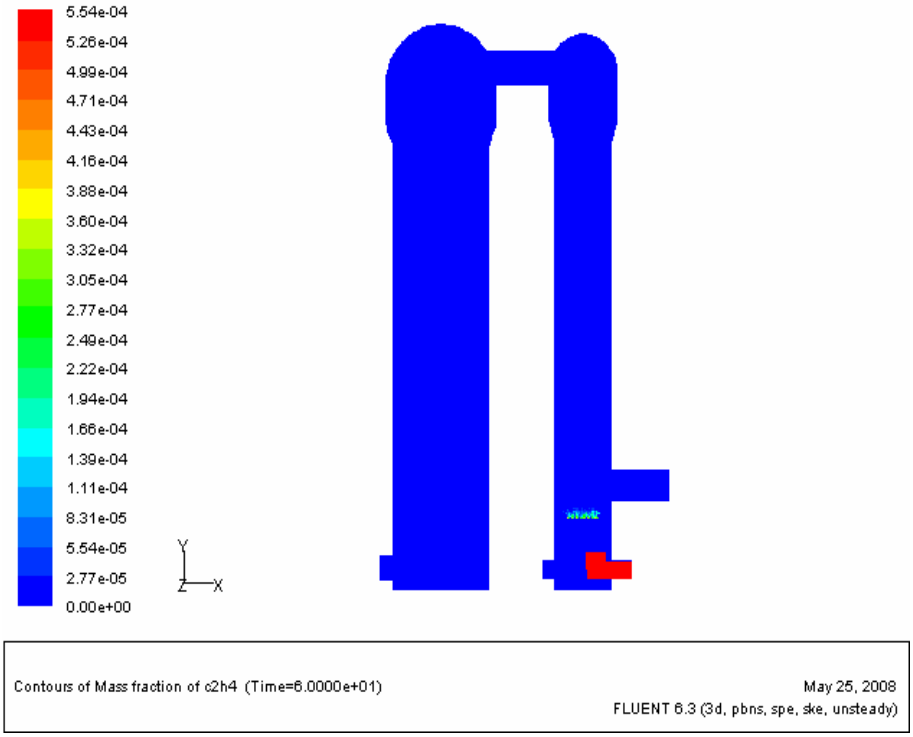

Fig. 4-10 Mass fraction distribution of C_2H_4 of 1st minute for the on-gas cycle

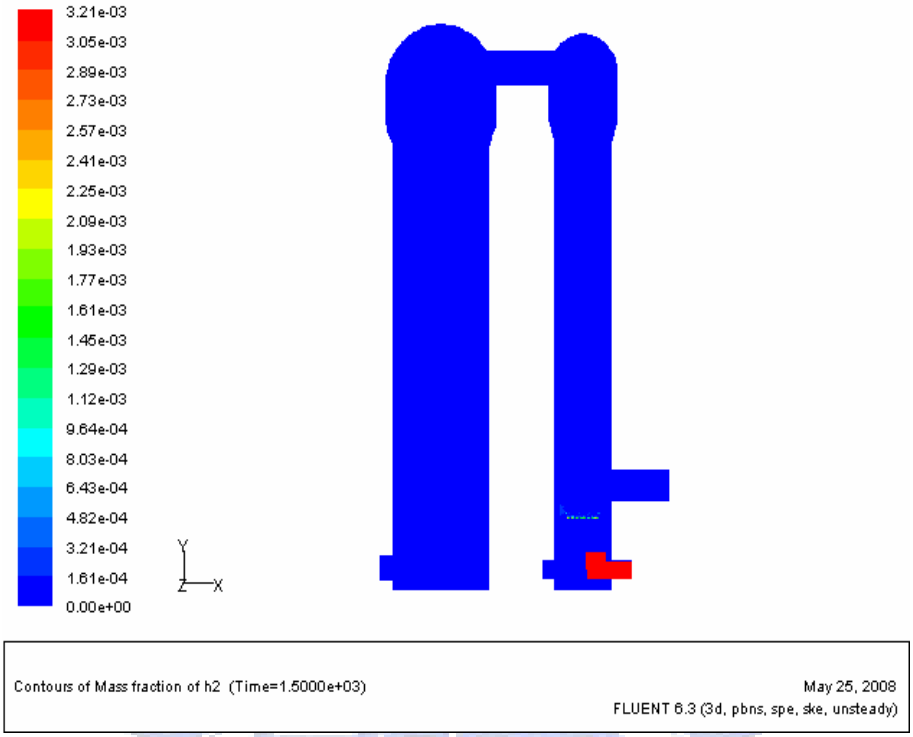

Fig. 4-11 Mass fraction distribution of H_2 of 25th minute for the on-gas cycle

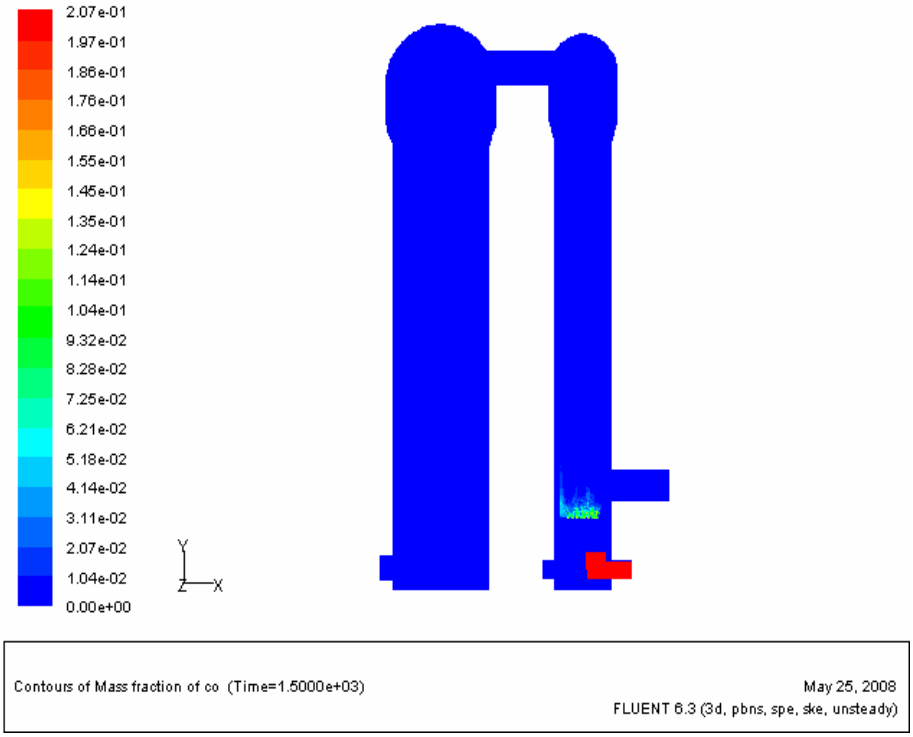

Fig. 4-12 Mass fraction distribution of CO of 25th minute for the on-gas cycle

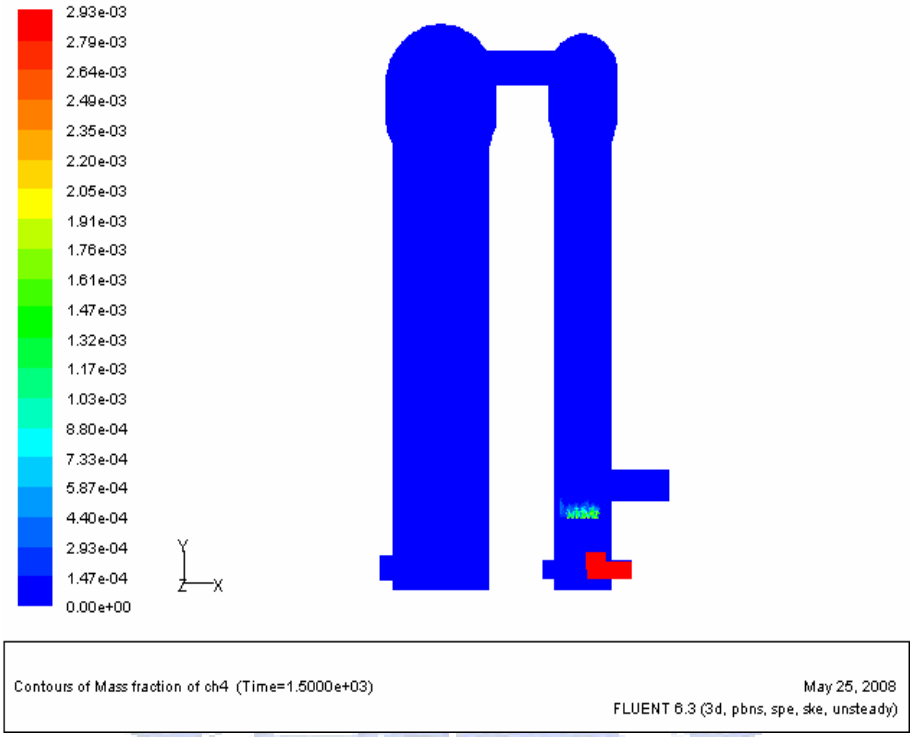

Fig. 4-13 Mass fraction distribution of CH_4 of 25th minute for the on-gas cycle

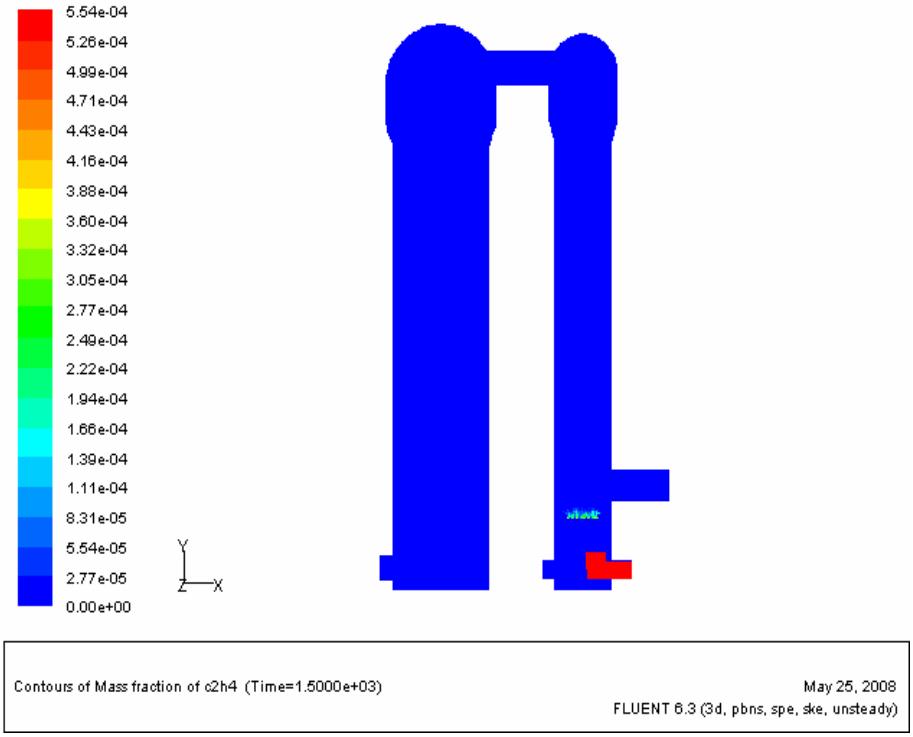

Fig. 4-14 Mass fraction distribution of C_2H_4 of 25th minute for the on-gas cycle

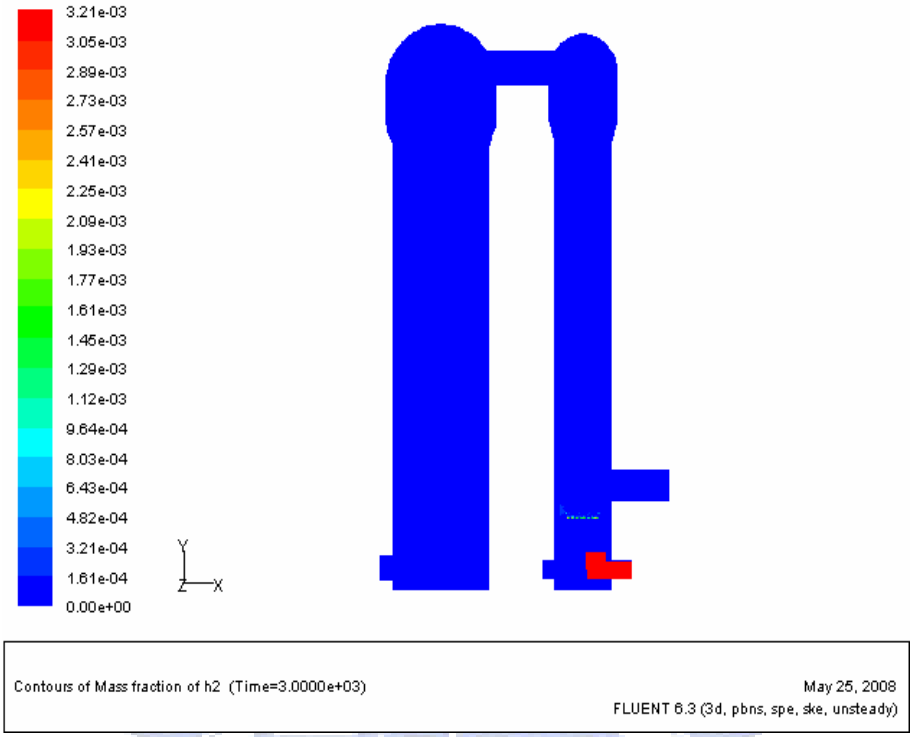

Fig. 4-15 Mass fraction distribution of H_2 of 50th minute for the on-gas cycle

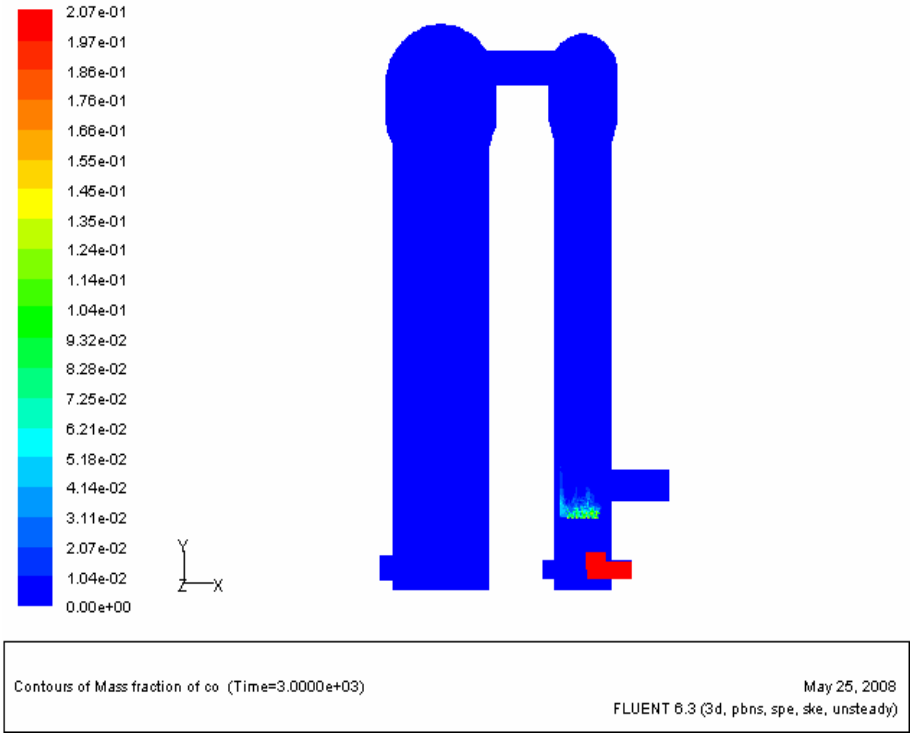

Fig. 4-16 Mass fraction distribution of CO of 50th minute for the on-gas cycle

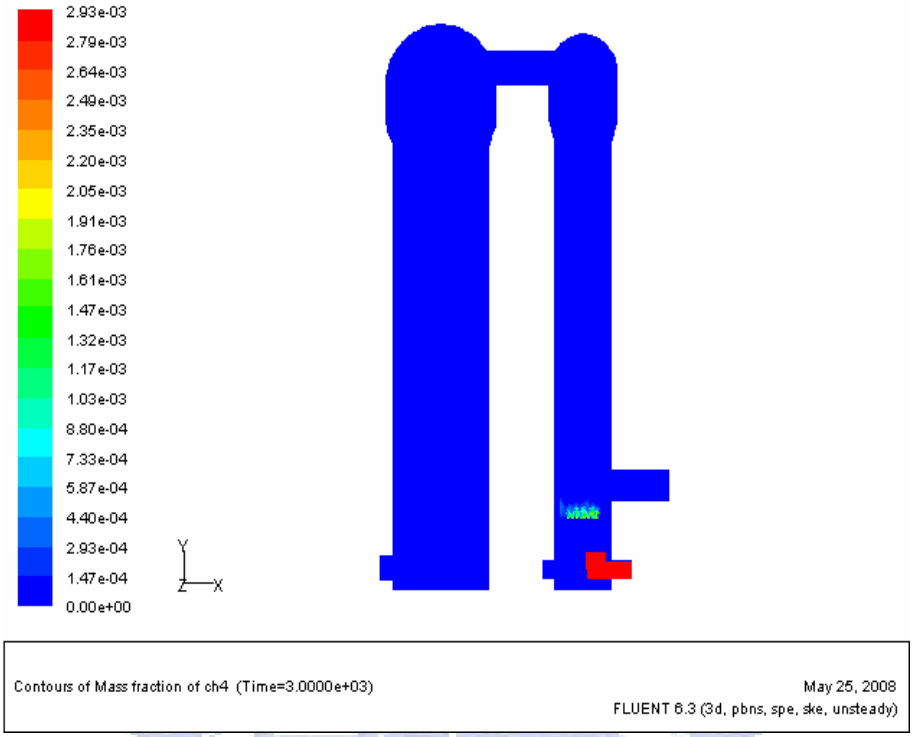

Fig. 4-17 Mass fraction distribution of CH_4 of 50th minute for the on-gas cycle

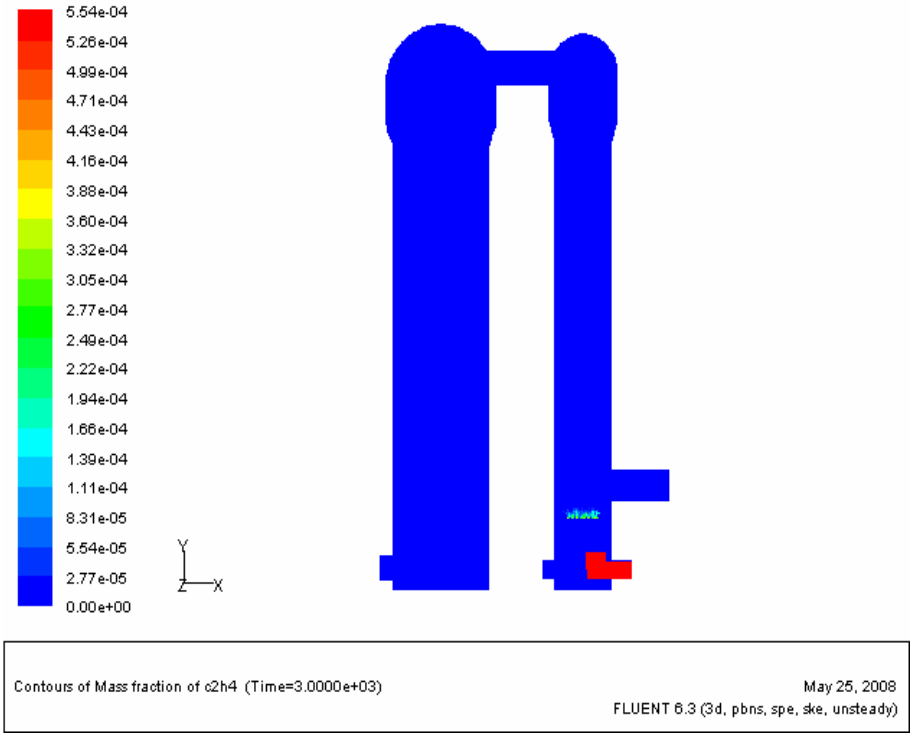

Fig. 4-18 Mass fraction distribution of C_2H_4 of 50th minute for the on-gas cycle

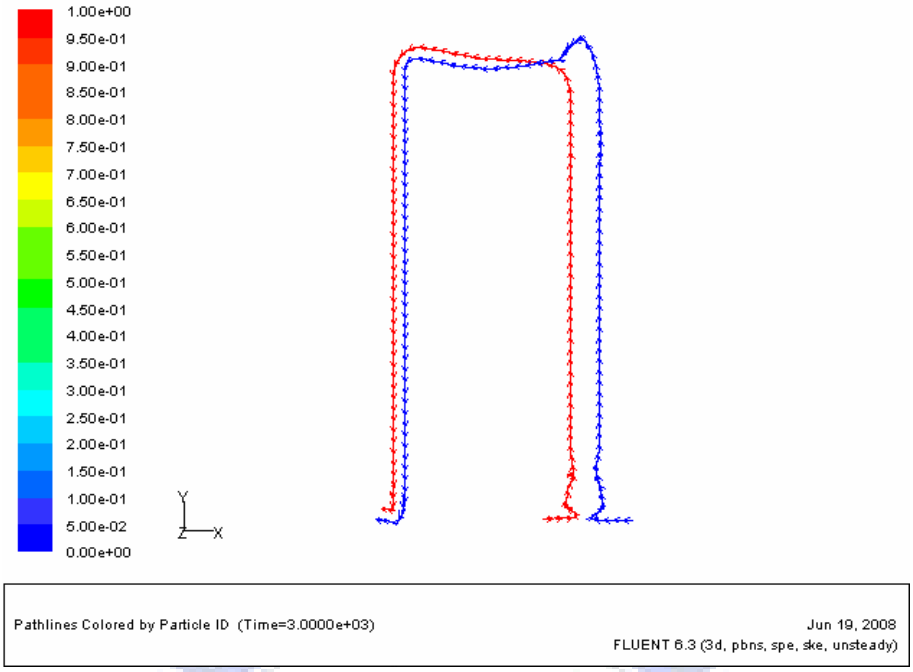

Fig. 4-19 Particle tracer of on-gas cycle in the reference case

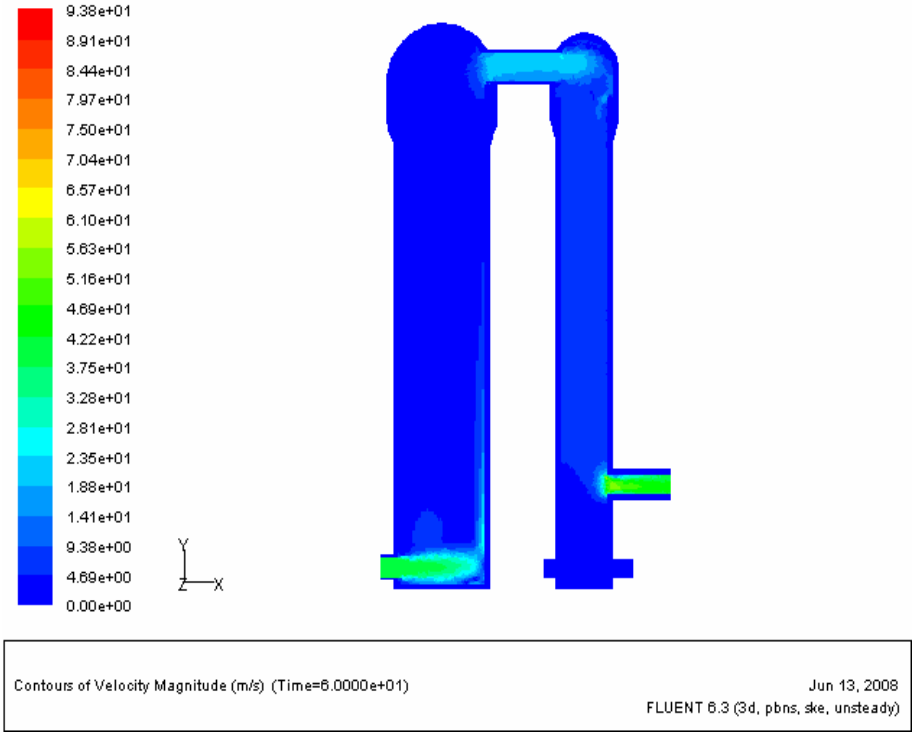

Fig. 4-20 Velocity distribution of 1st minute for the on-blast cycle

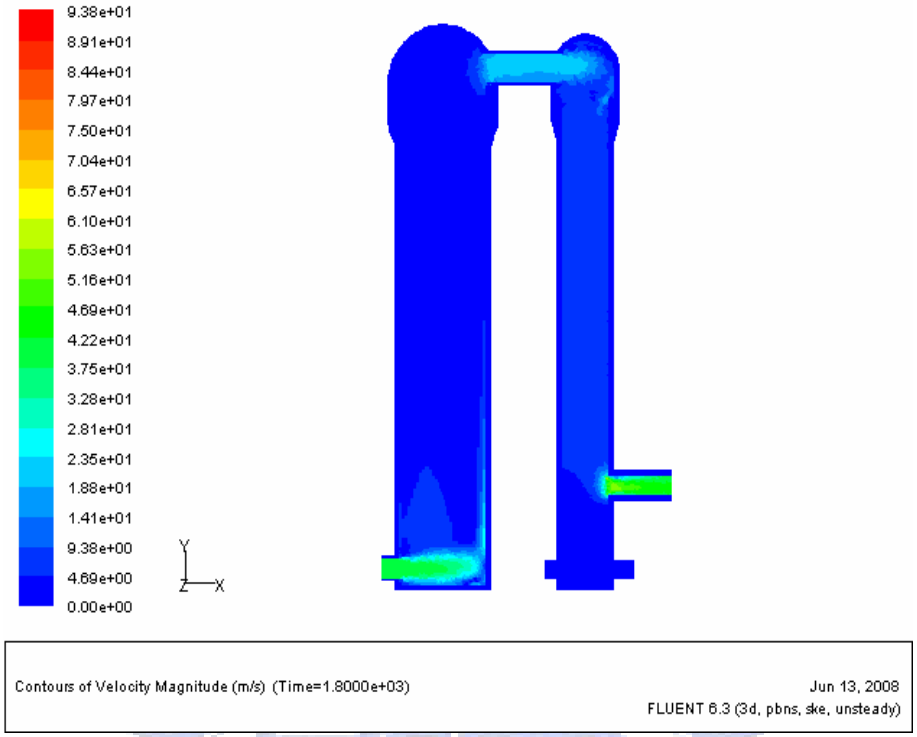

Fig. 4-21 Velocity distribution of 30th minute for the on-blast cycle

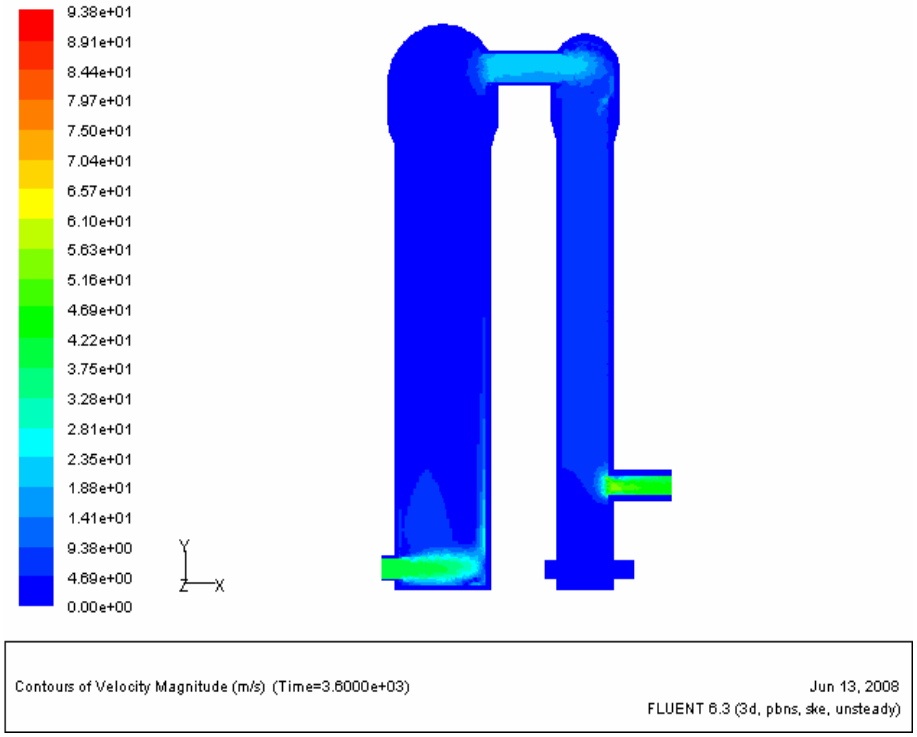

Fig. 4-22 Velocity distribution of 60th minute for the on-blast cycle

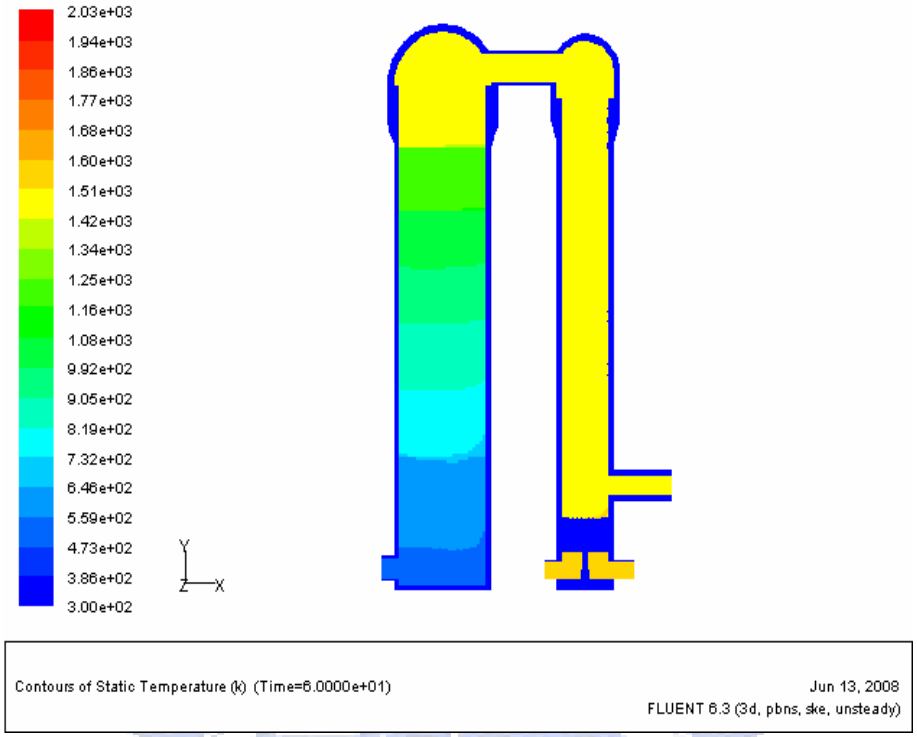

Fig. 4-23 Temperature distribution of 1st minute for the on-blast cycle

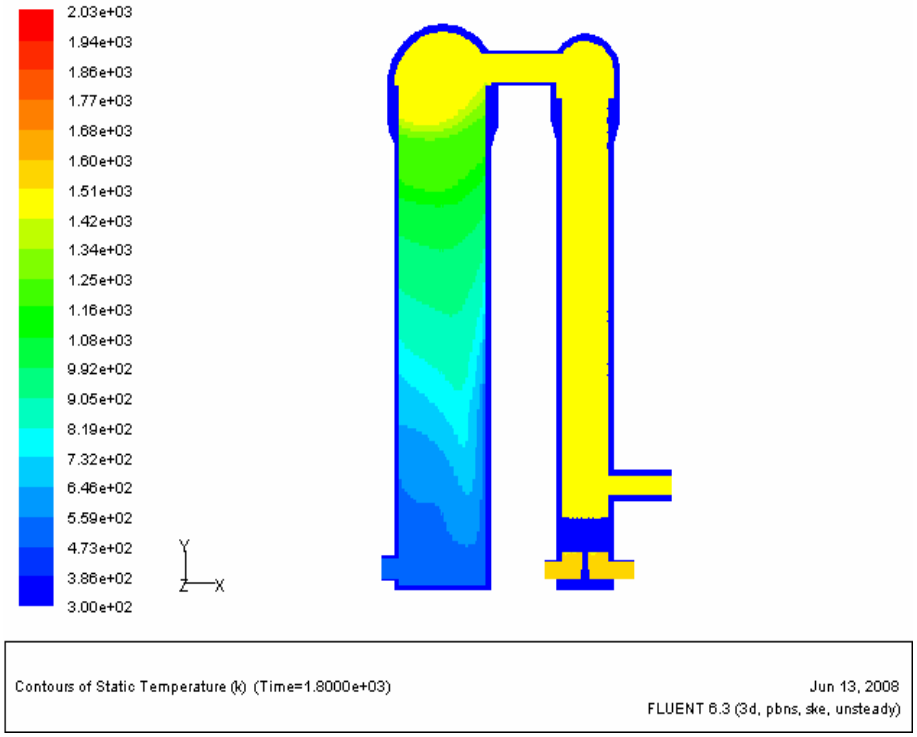

Fig. 4-24 Temperature distribution of 30th minute for the on-blast cycle

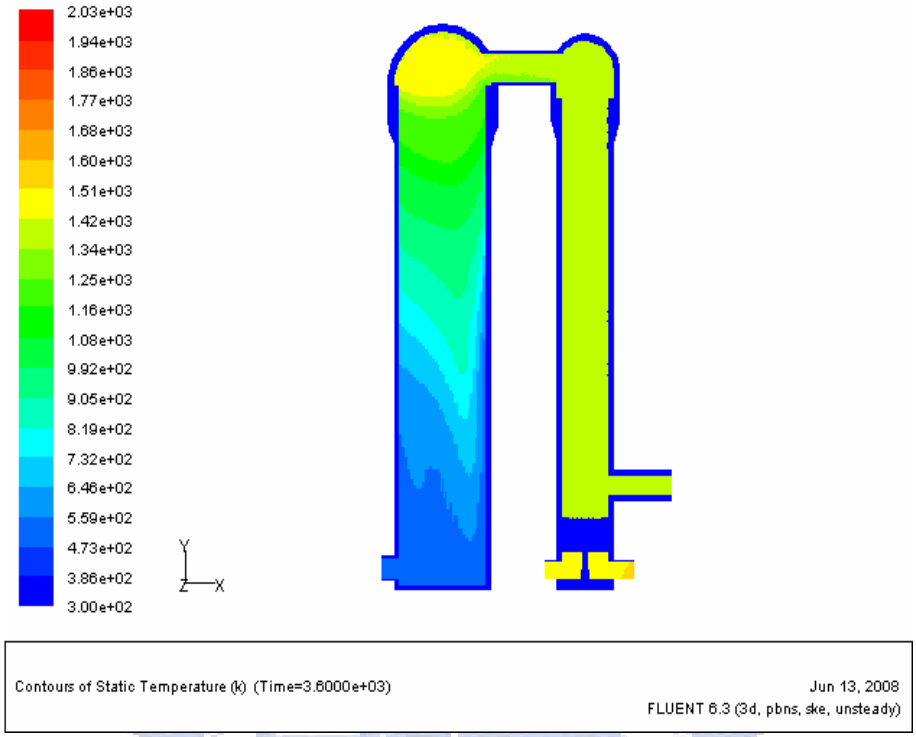

Fig. 4-25 Temperature distribution of 60th minute for the on-blast cycle

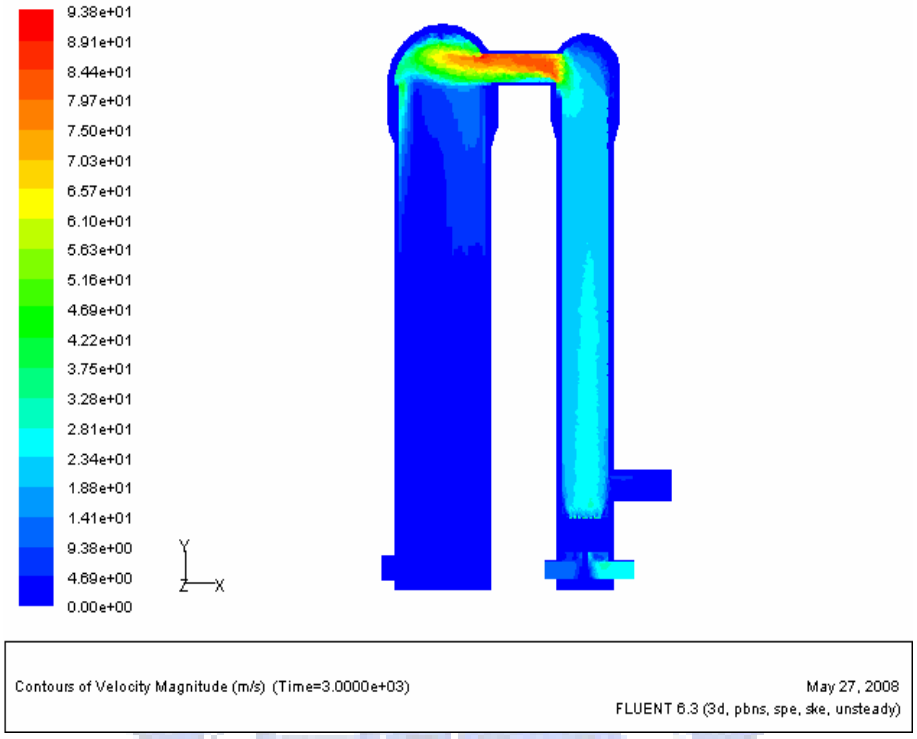

(a) Velocity distribution

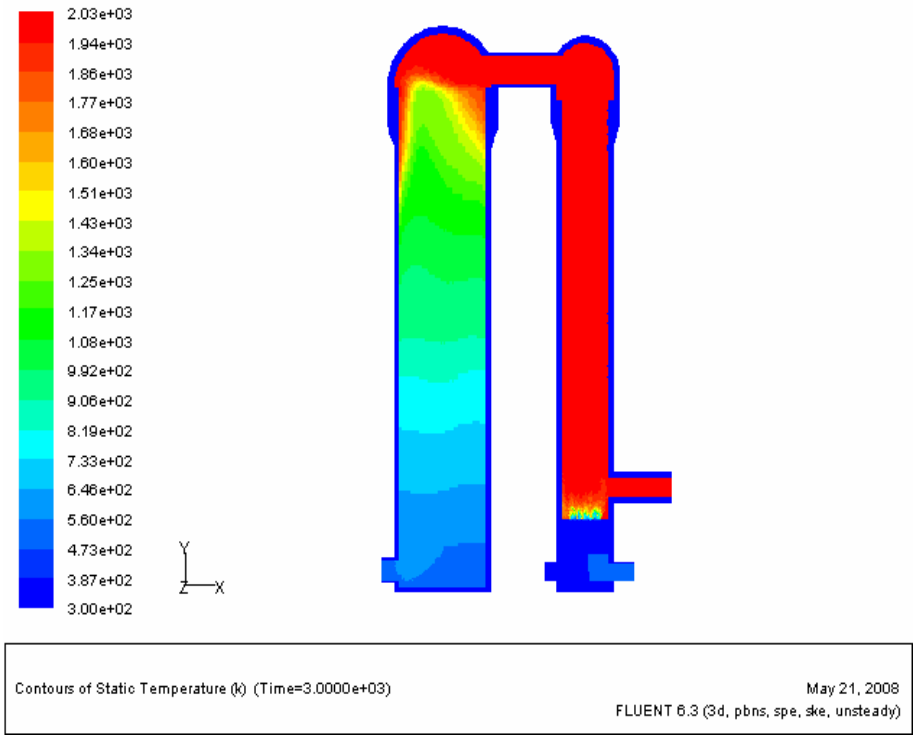

(b) Temperature distribution

Fig. 4-26 Velocity and temperature distributions in the end of on-gas cycle (BFG = 82048 Nm^3/h, COG = 1805 Nm^3/h)

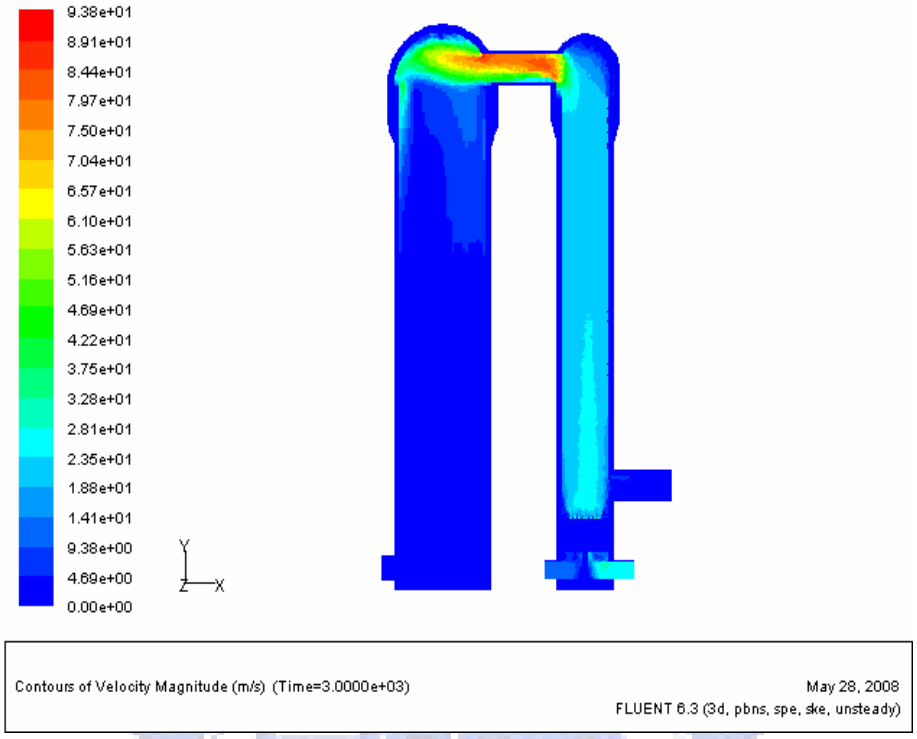

(a) Velocity distribution

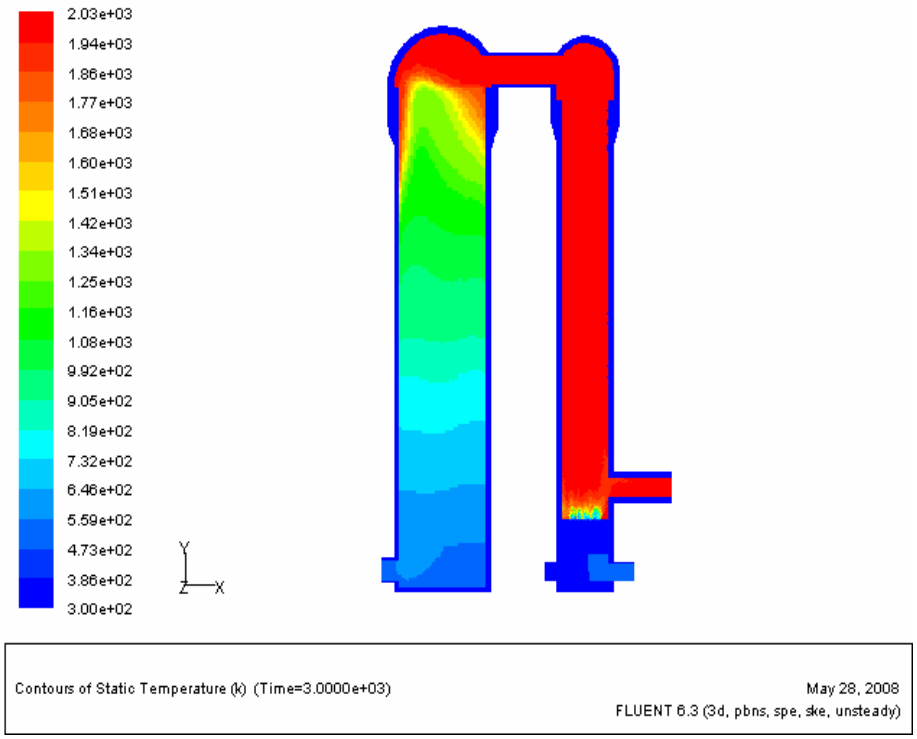

(b) Temperature distribution

Fig. 4-27 Velocity and temperature distributions in the end of on-gas cycle (BFG = 82589.5 Nm^3/h, COG = 1263.5 Nm^3/h)

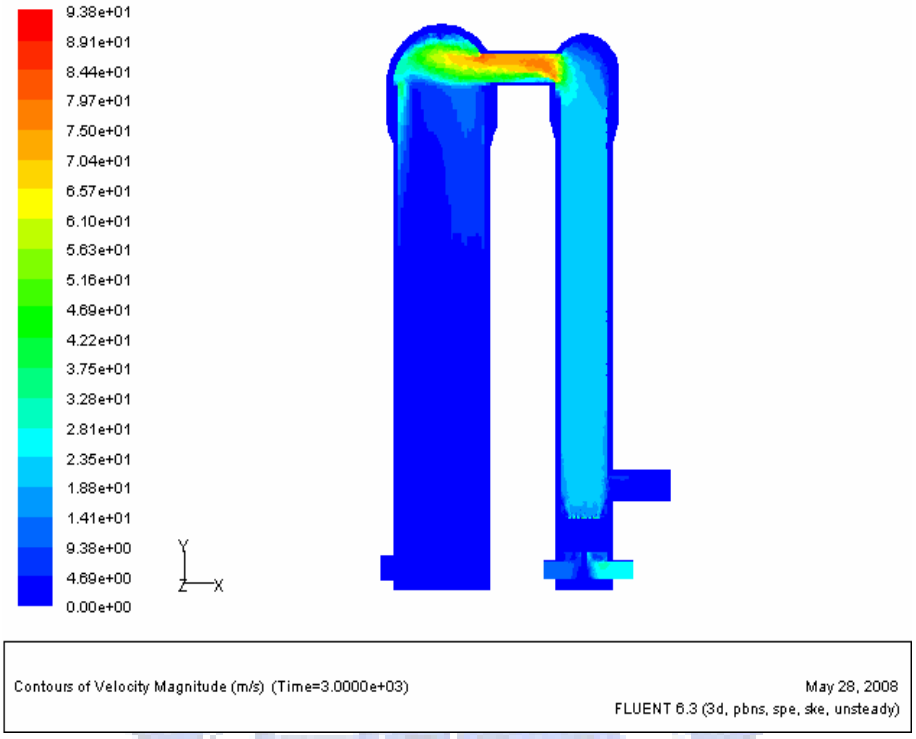

(a) Velocity distribution

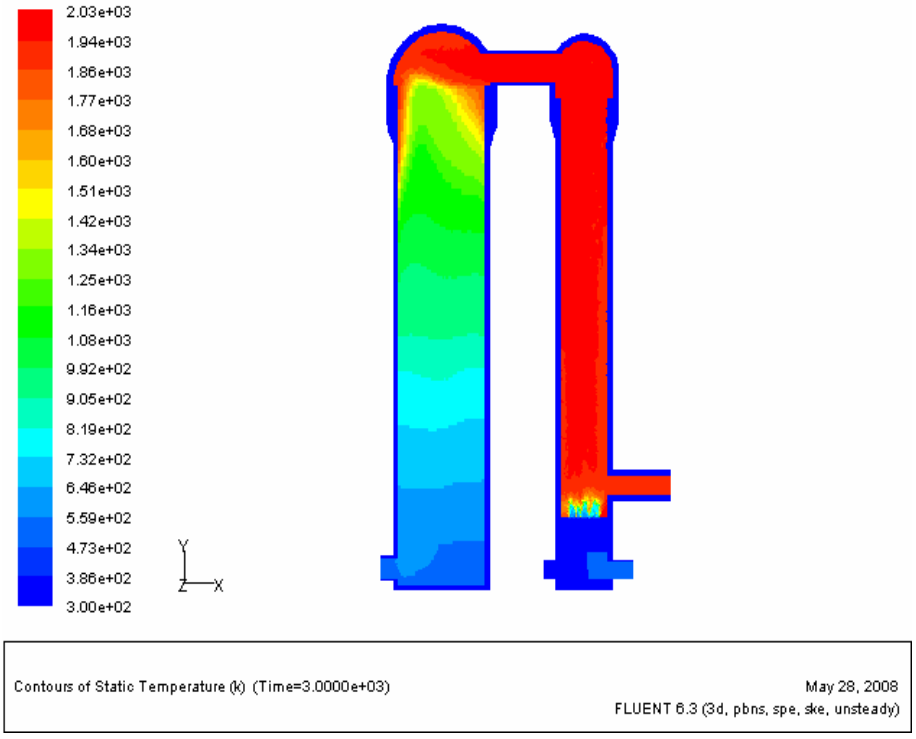

(b) Temperature distribution

Fig. 4-28 Velocity and temperature distributions in the end of on-gas cycle (BFG = 83853 Nm^3/h)

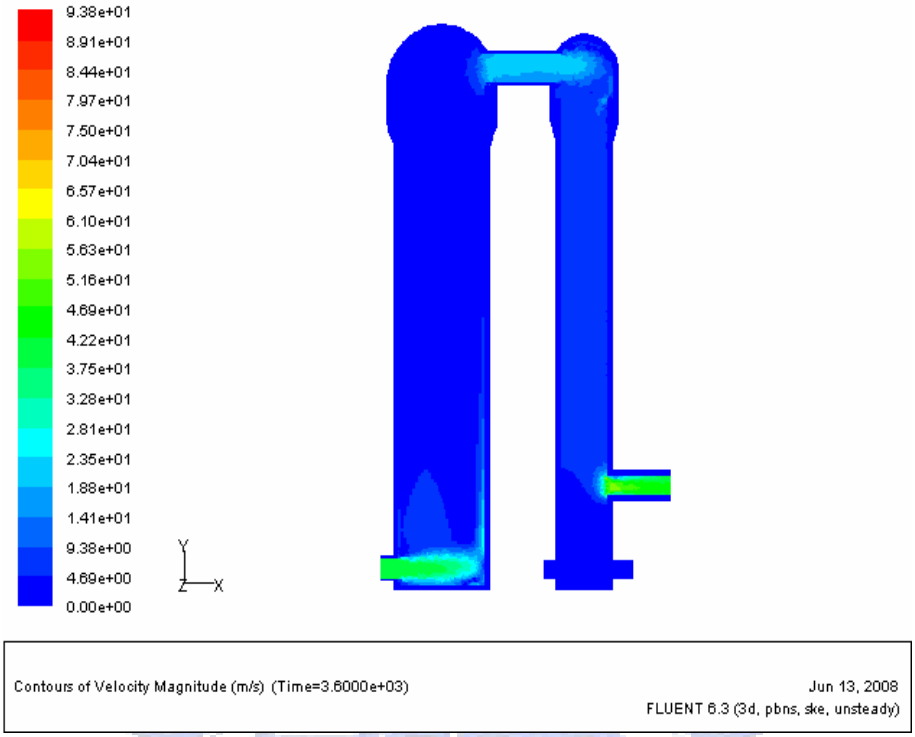

(a) Velocity distribution

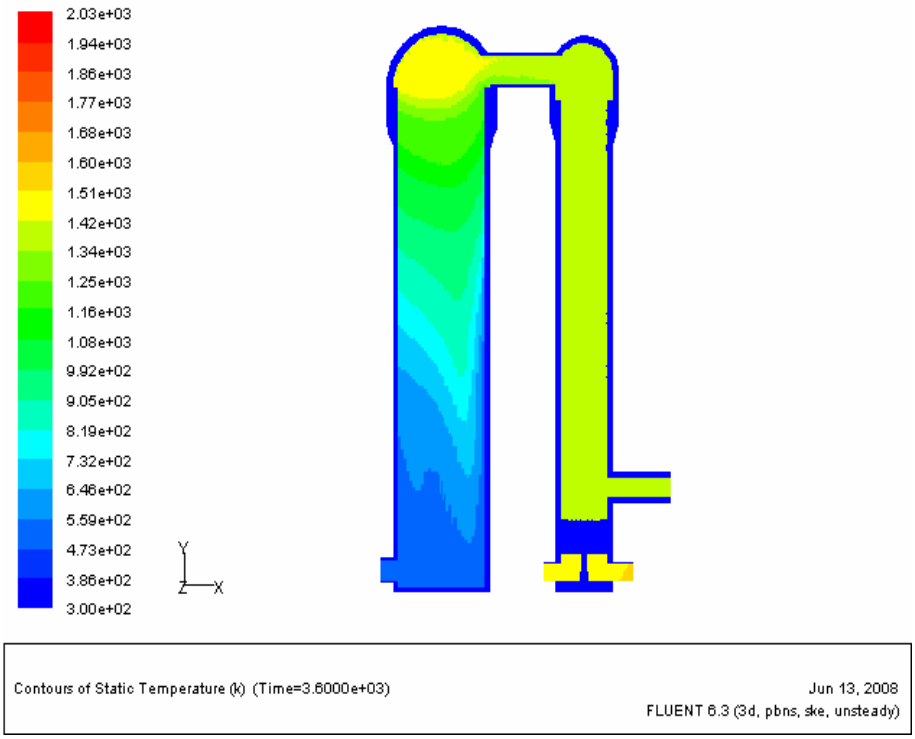

(b) Temperature distribution

Fig. 4-29 Velocity and temperature distributions in the end of on-blast cycle (BFG = 82048 Nm^3/h, COG = 1805 Nm^3/h)

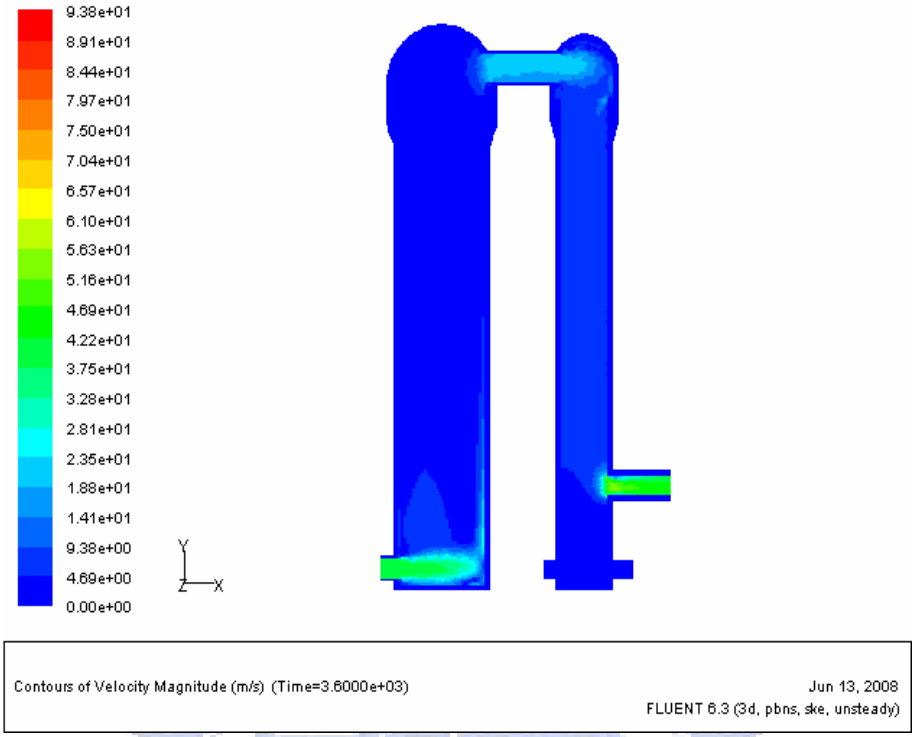

(a) Velocity distribution

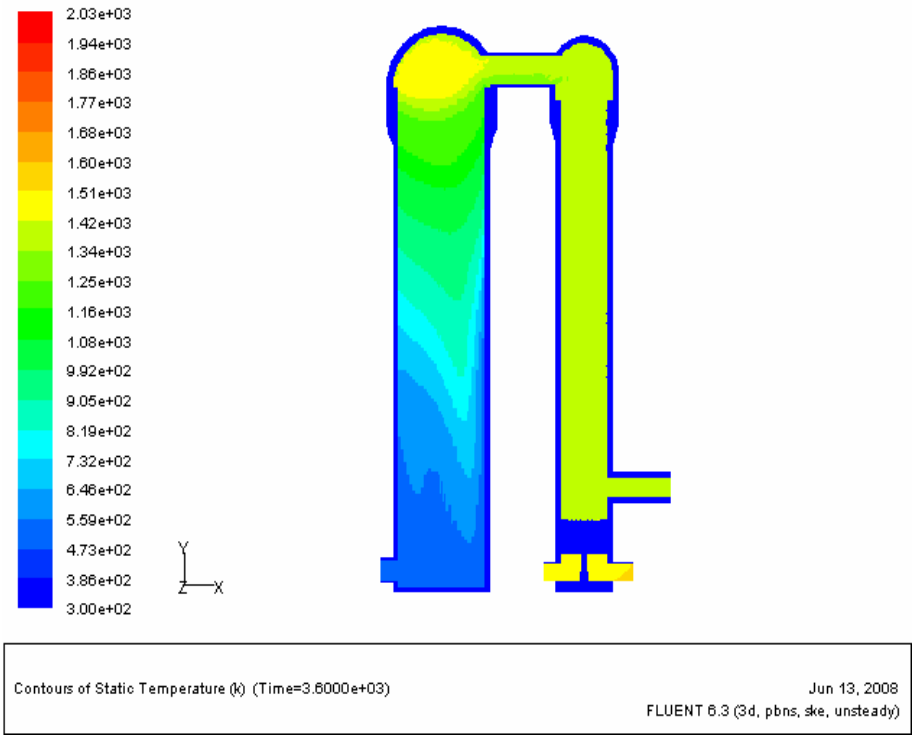

(b) Temperature distribution

Fig. 4-30 Velocity and temperature distributions in the end of on-blast cycle (BFG = 82589.5 Nm^3/h, COG = 1263.5 Nm^3/h)

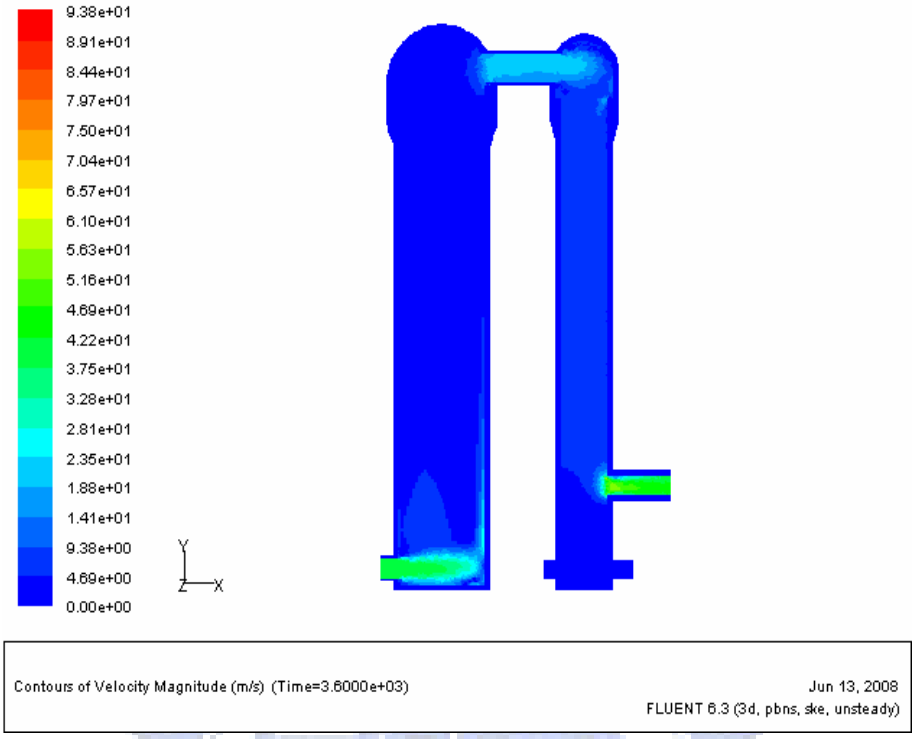

(a) Velocity distribution

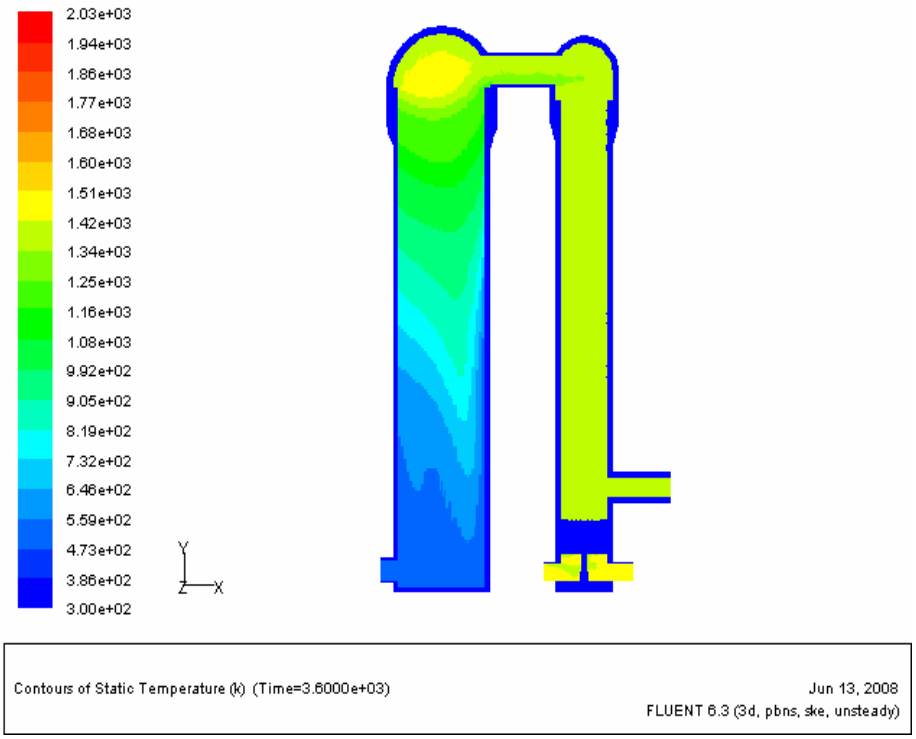

(b) Temperature distribution

Fig. 4-31 Velocity and temperature distributions in the end of on-blast cycle (BFG = 83853 Nm^3/h)

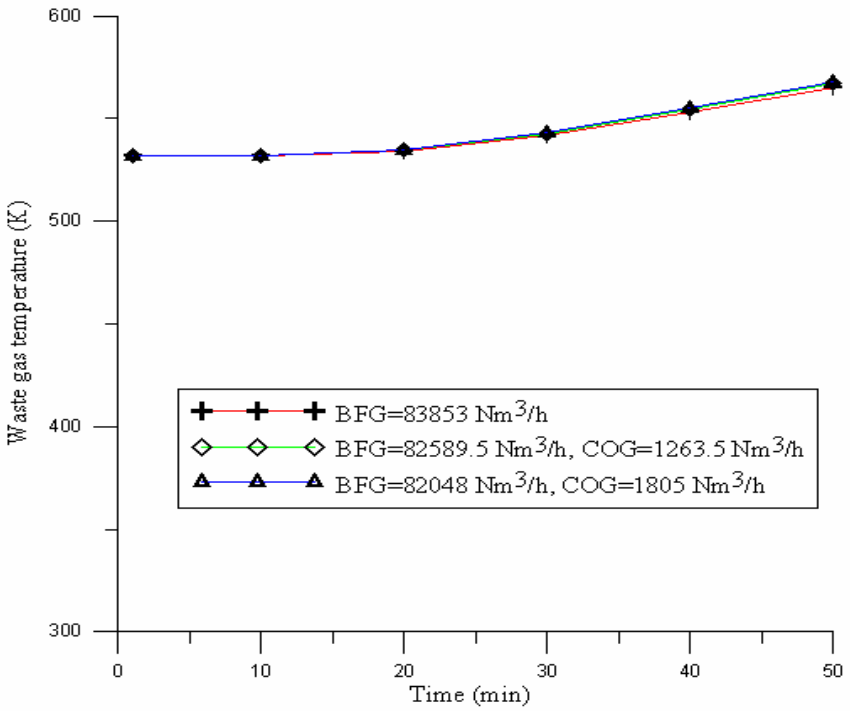

Fig. 4-32 Waste gas temperatures for different BFG/COG ratios

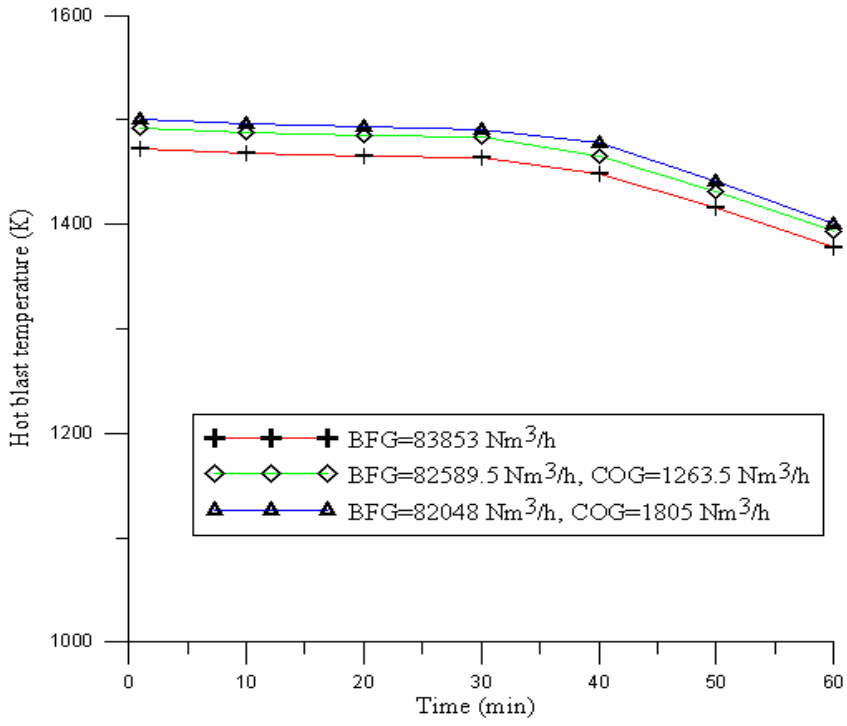

Fig. 4-33 Hot blast temperatures for different BFG/COG ratios

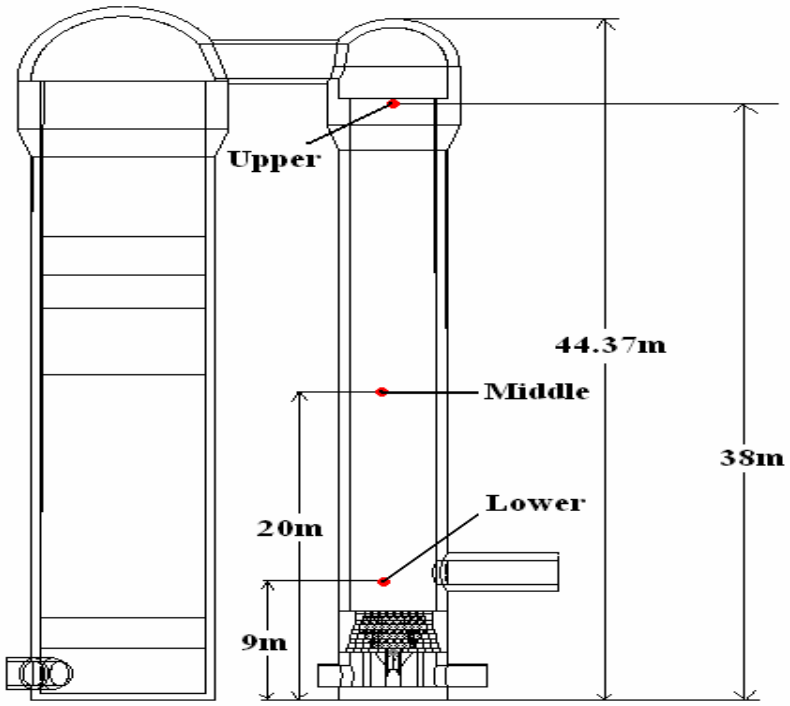

Fig. 4-34 Measuring points in the combustion chamber

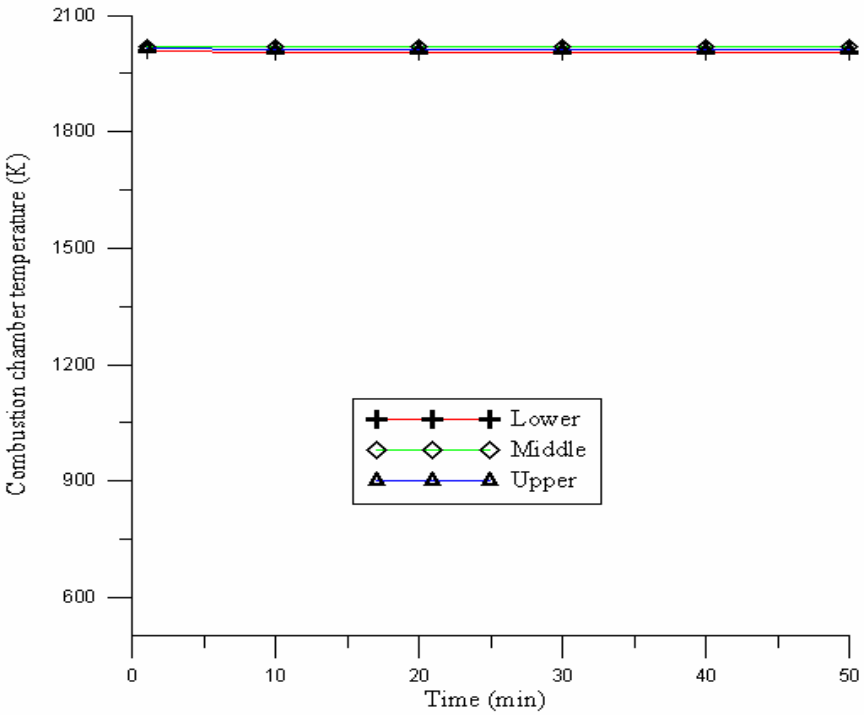

Fig. 4-35 Combustion chamber temperature during on-gas cycle (BFG = 82048 Nm3/h, COG = 1805 Nm3/h)

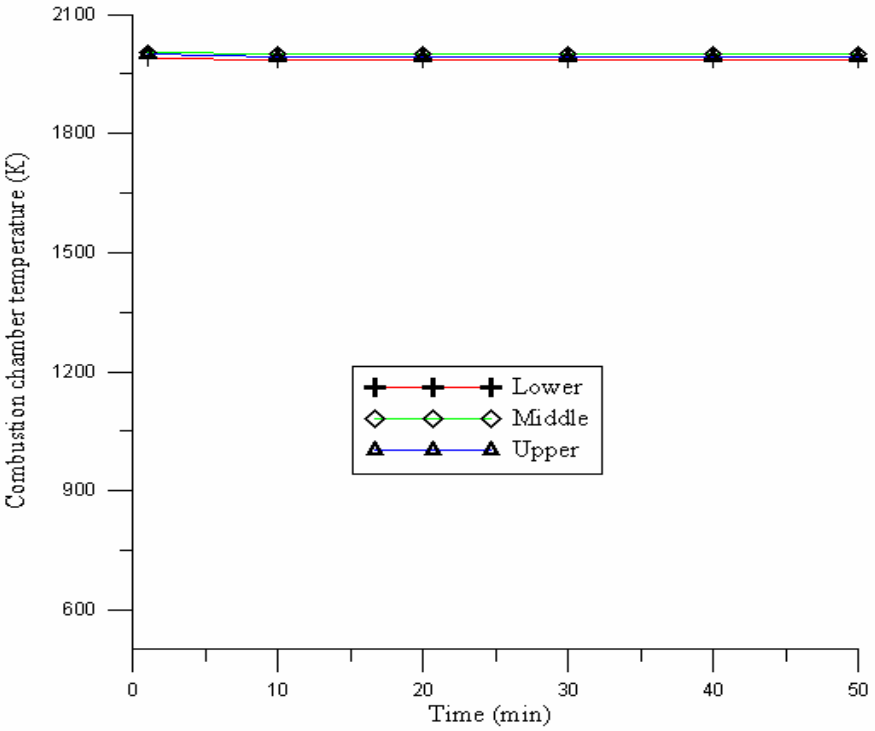

Fig. 4-36 Combustion chamber temperature during on-gas cycle (BFG = 82589.5 Nm3/h, COG = 1263.5 Nm3/h)

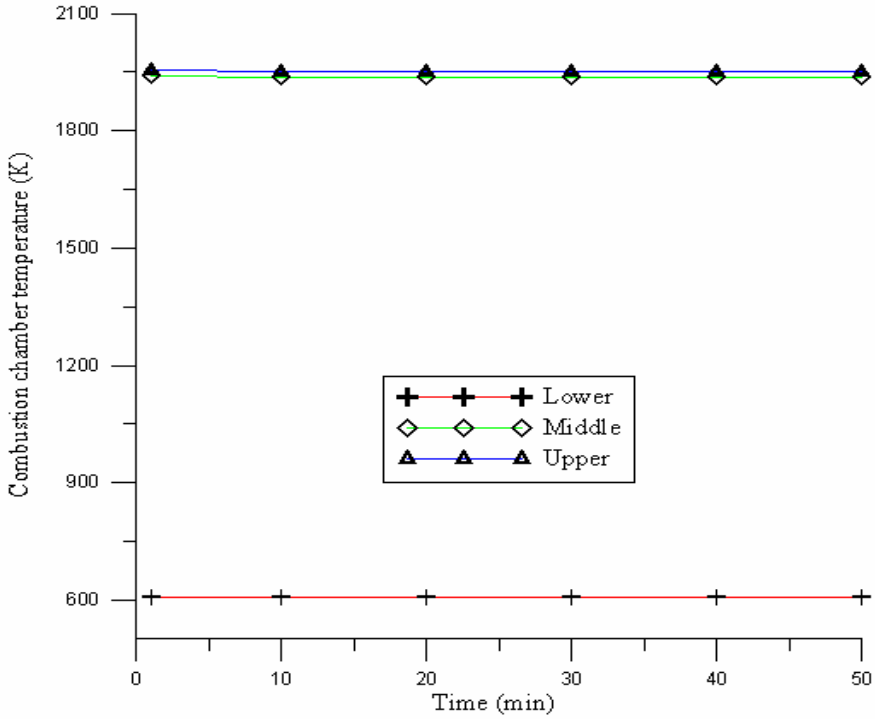

Fig. 4-37 Combustion chamber temperature during on-gas cycle (BFG = 83853 Nm3/h)

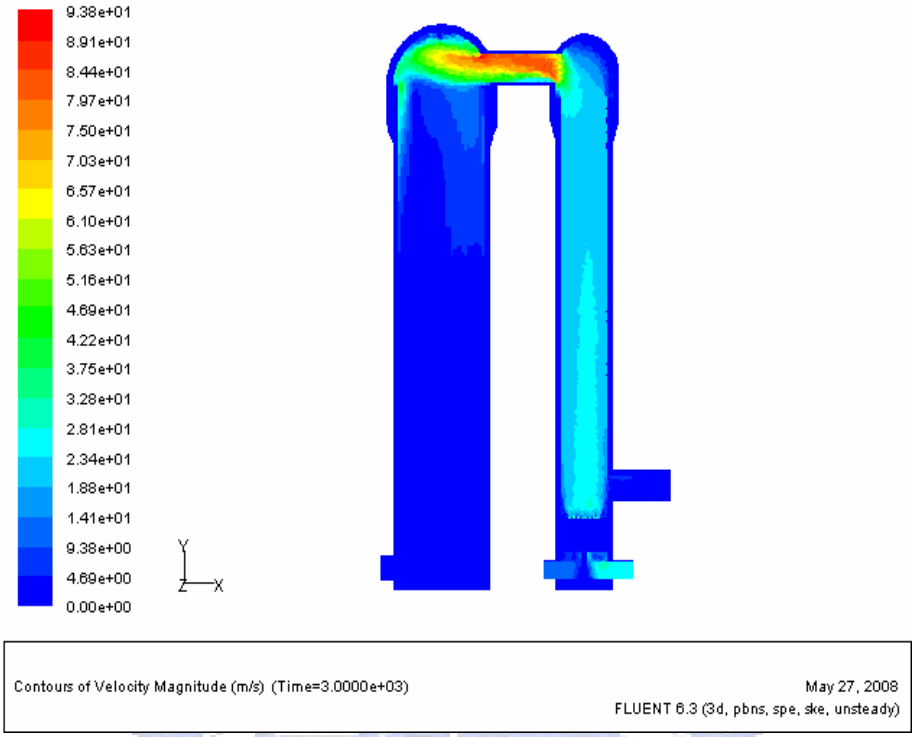

(a) Velocity distribution

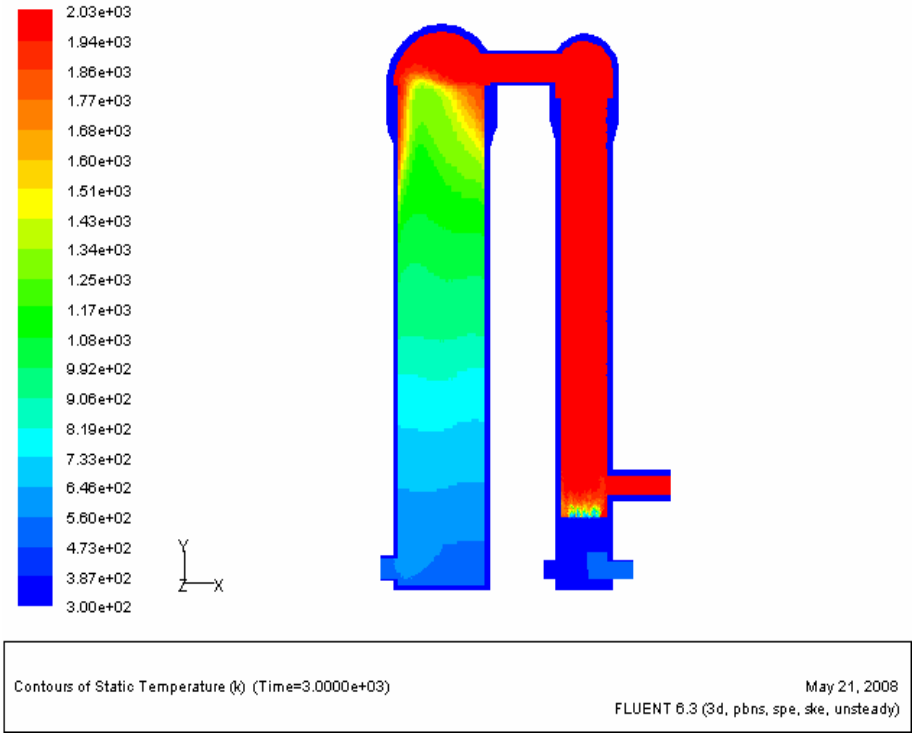

(b) Temperature distribution

Fig. 4-38 Velocity and temperature distributions in the end of on-gas cycle

(BFG = 82048 Nm^3/h, COG = 1805 Nm^3/h)

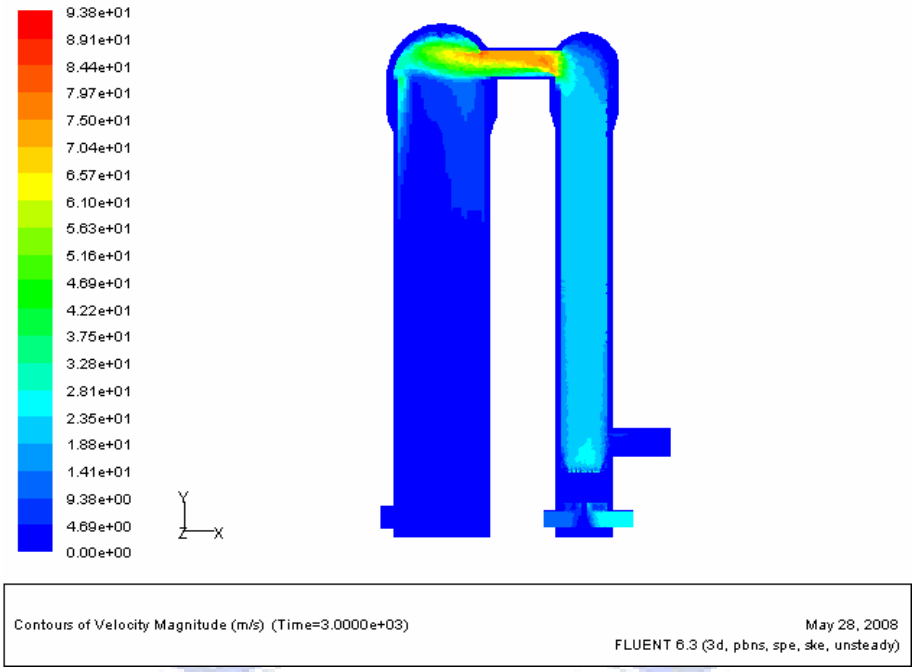

(a) Velocity distribution

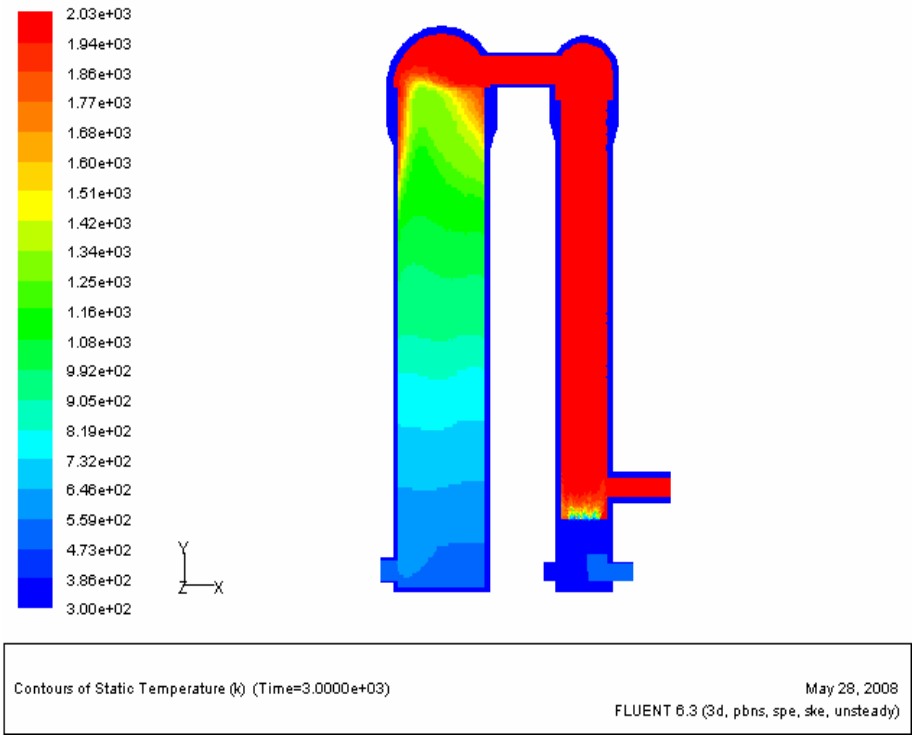

(b) Temperature distribution

Fig. 4-39 Velocity and temperature distributions in the end of on-gas cycle

(BFG = 73843.2 Nm^3/h, COG = 1624.5 Nm^3/h)

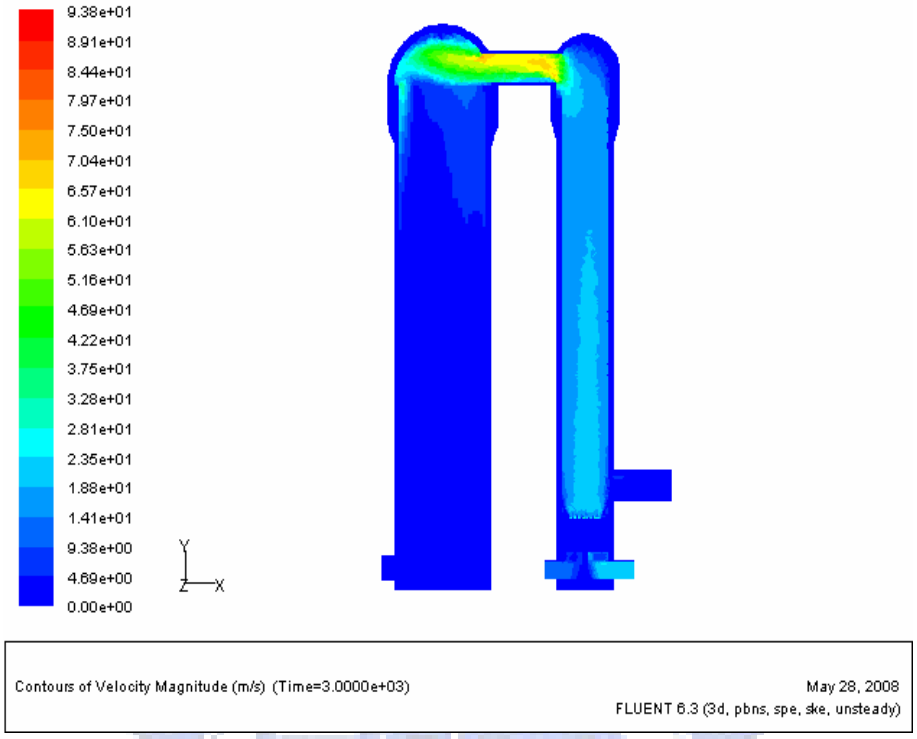

(a) Velocity distribution

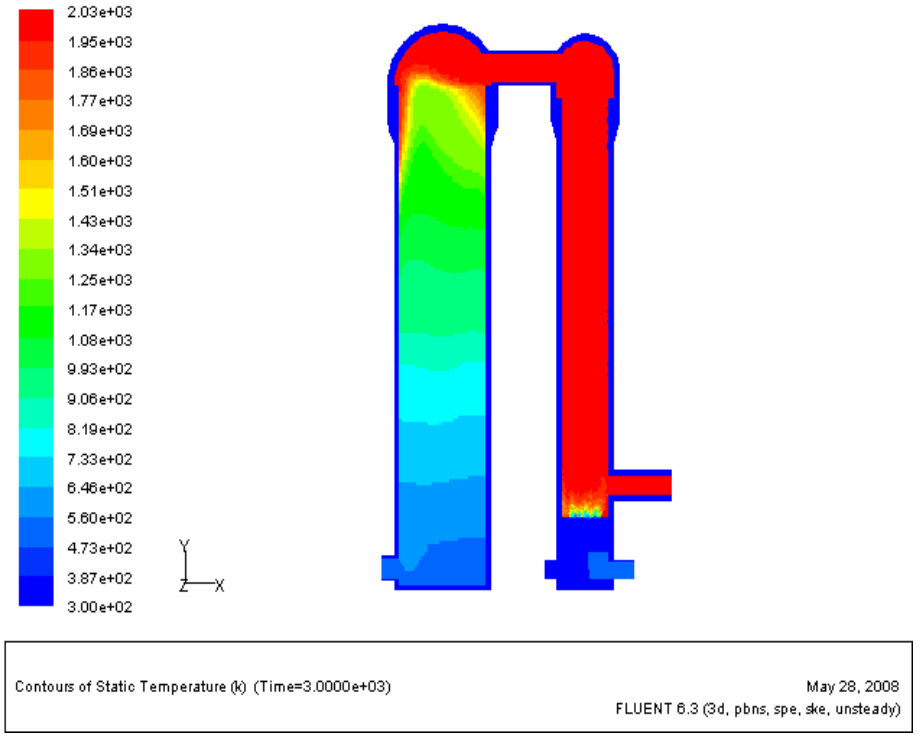

(b) Temperature distribution

Fig. 4-40 Velocity and temperature distributions in the end of on-gas cycle

(BFG = 65638.4 Nm^3/h, COG = 1444 Nm^3/h)

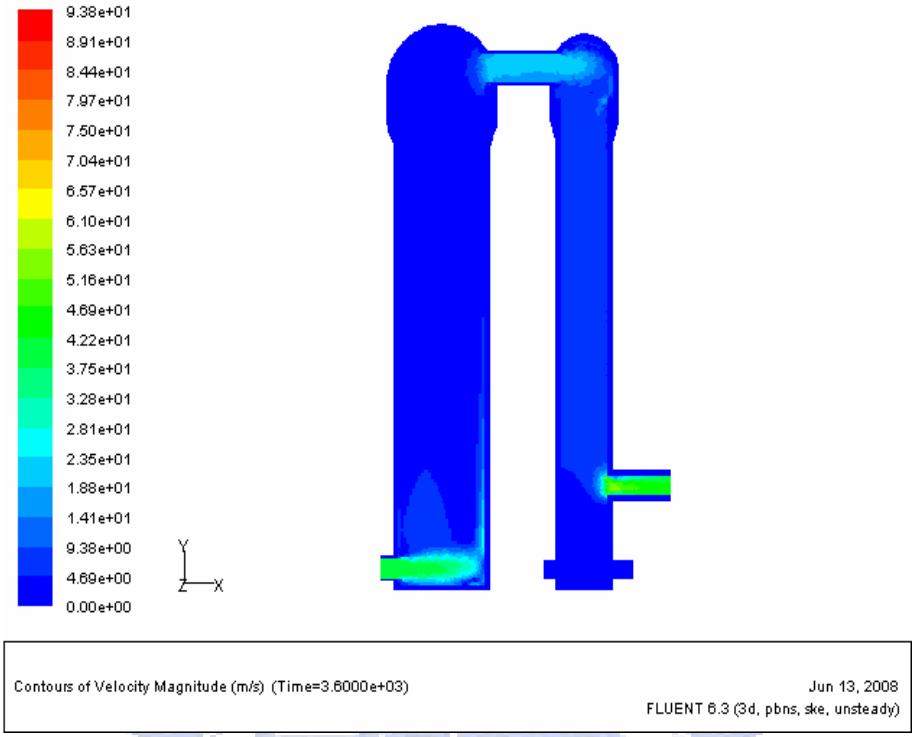

(a) Velocity distribution

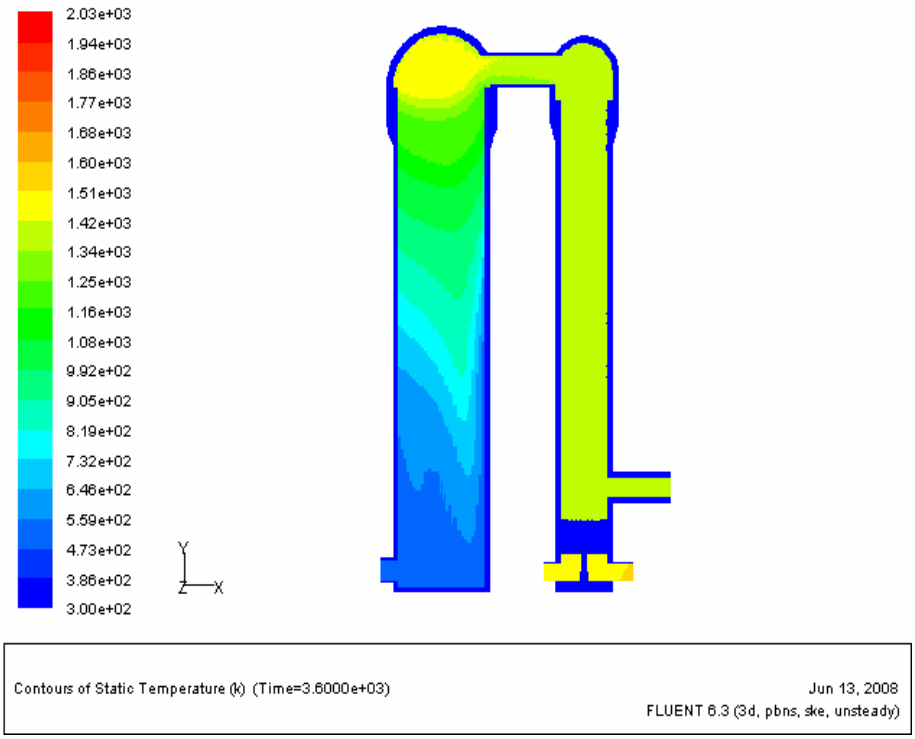

(b) Temperature distribution

Fig. 4-41 Velocity and temperature distributions in the end of on-blast cycle (BFG = 82048 Nm^3/h, COG = 1805 Nm^3/h)

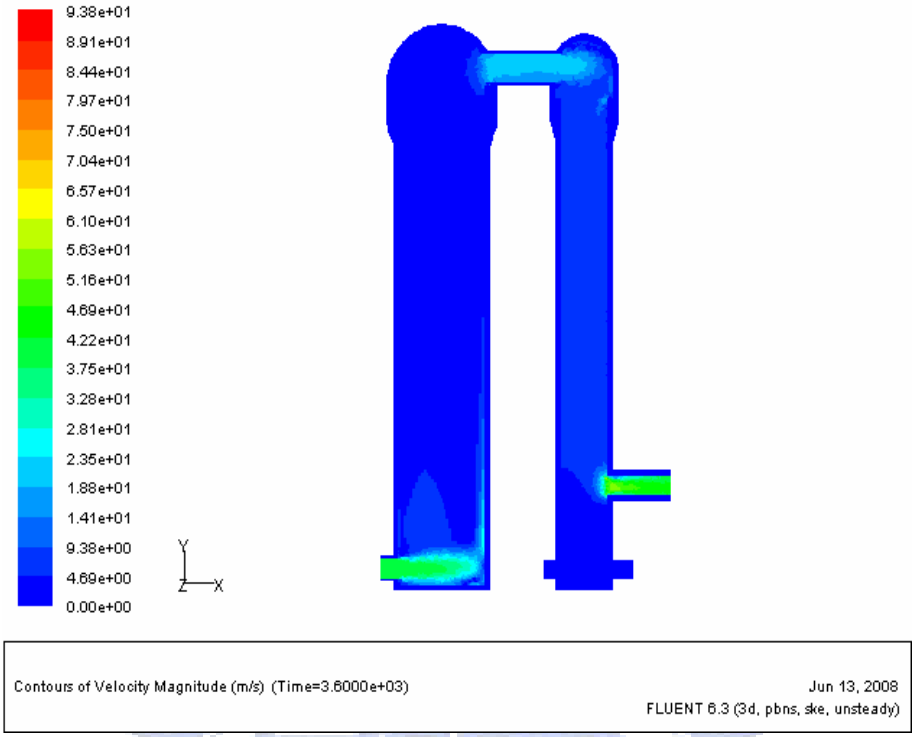

(a) Velocity distribution

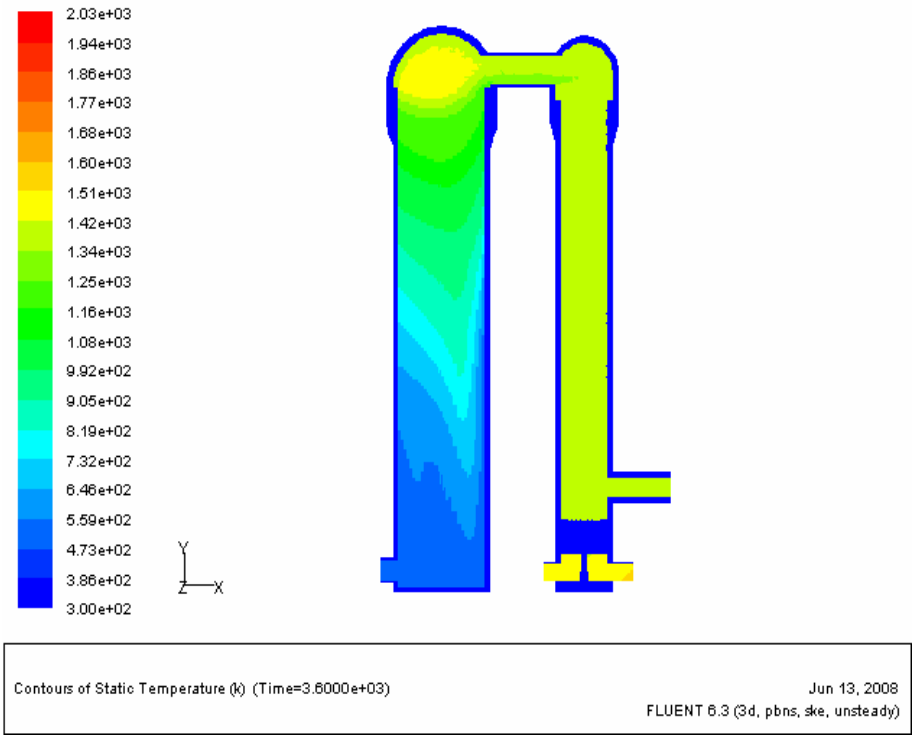

(b) Temperature distribution

Fig. 4-42 Velocity and temperature distributions in the end of on-blast cycle (BFG = 73843.2 Nm^3/h, COG = 1624.5 Nm^3/h)

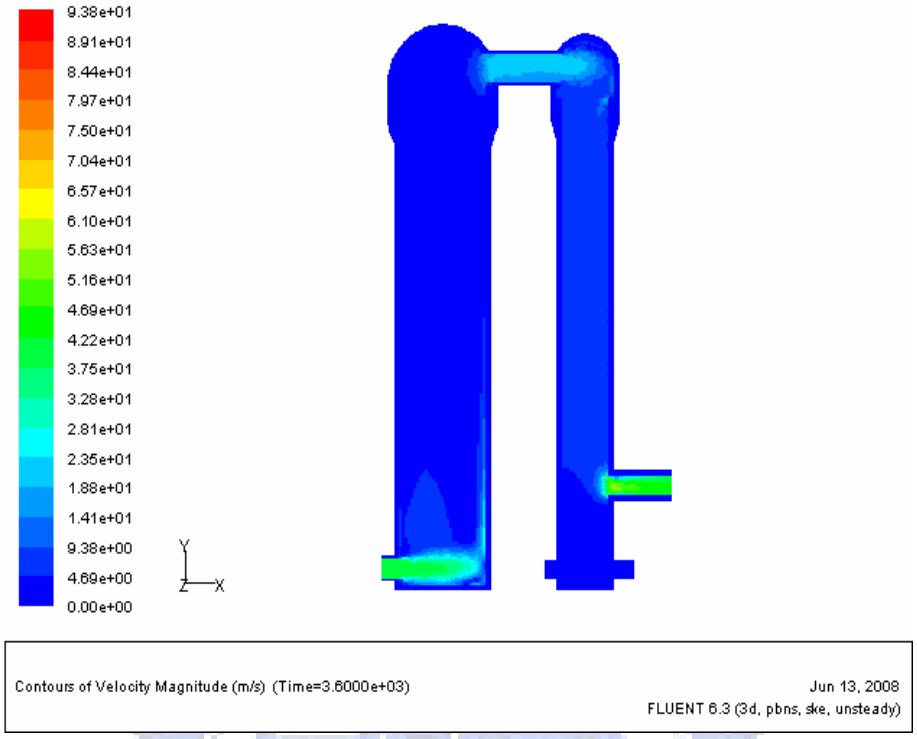

(a) Velocity distribution

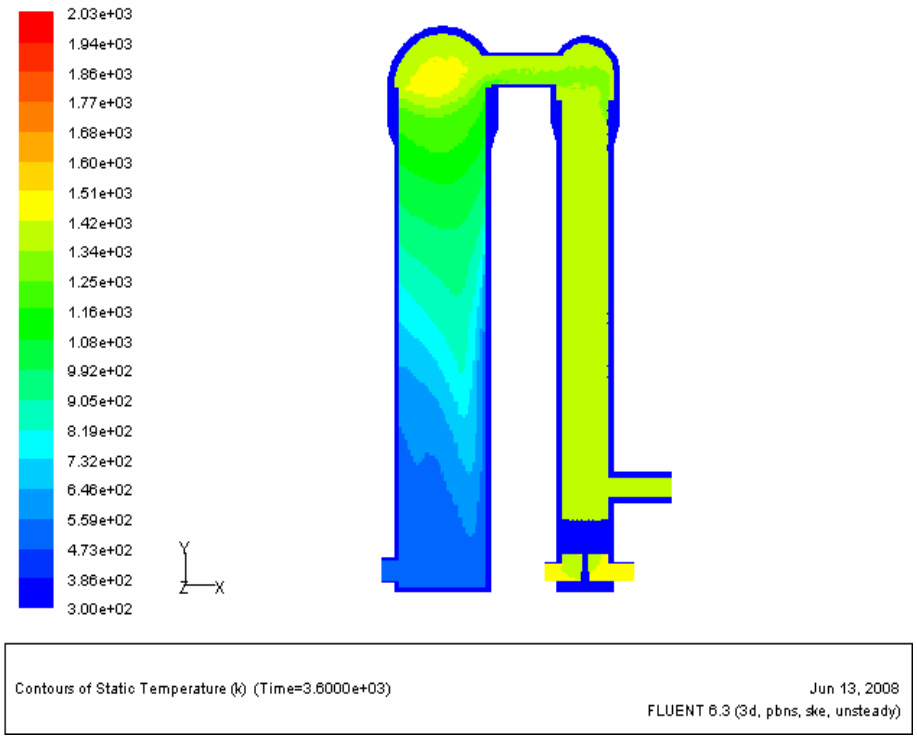

(b) Temperature distribution

Fig. 4-43 Velocity and temperature distributions in the end of on-blast cycle (BFG = 65638.4 Nm^3/h, COG = 1444 Nm^3/h)

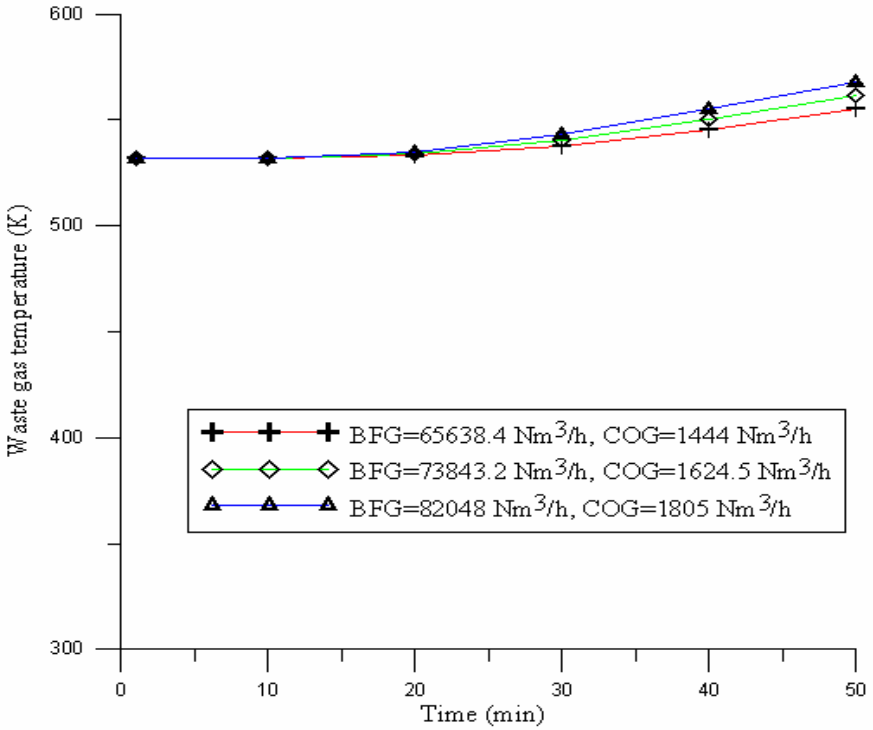

Fig. 4-44 Waste gas temperatures for different volume flow rates of mixed fuel gas

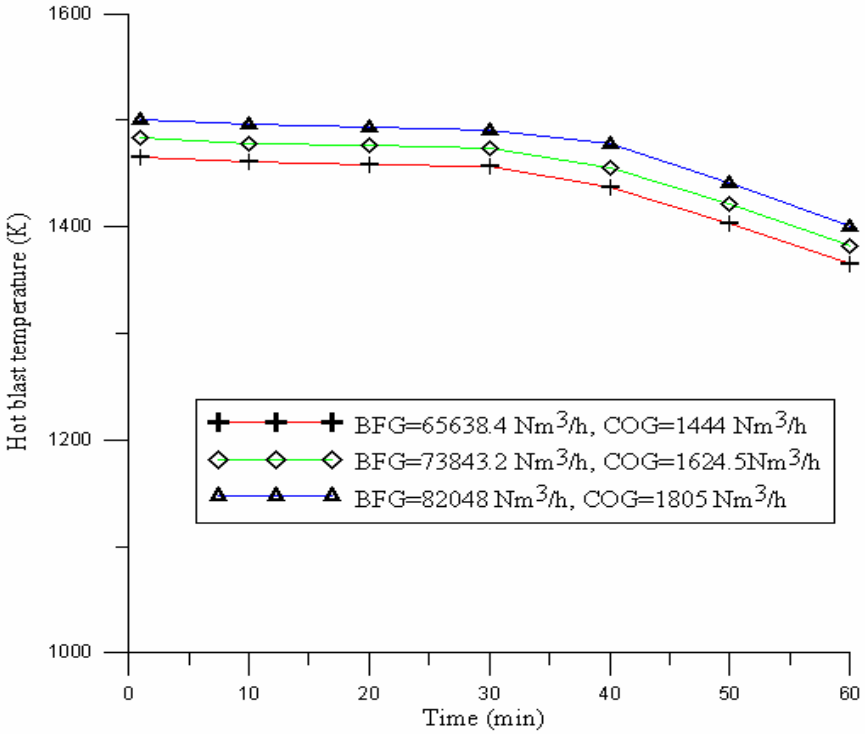

Fig. 4-45 Hot blast temperatures for different volume flow rates of mixed fuel gas

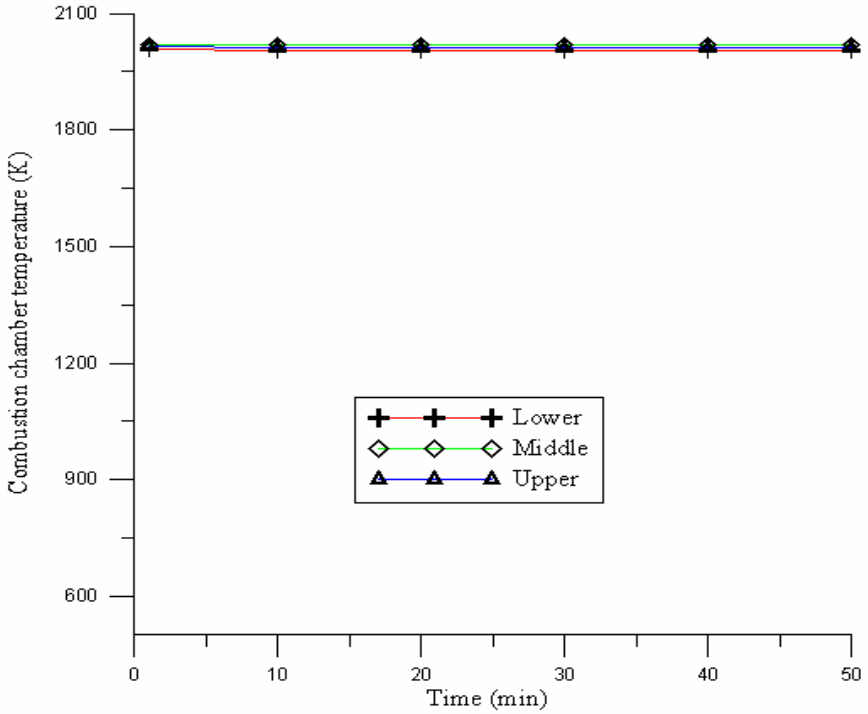

Fig. 4-46 Combustion chamber temperature during on-gas cycle (BFG = 82048 Nm3/h, COG = 1805 Nm3/h)

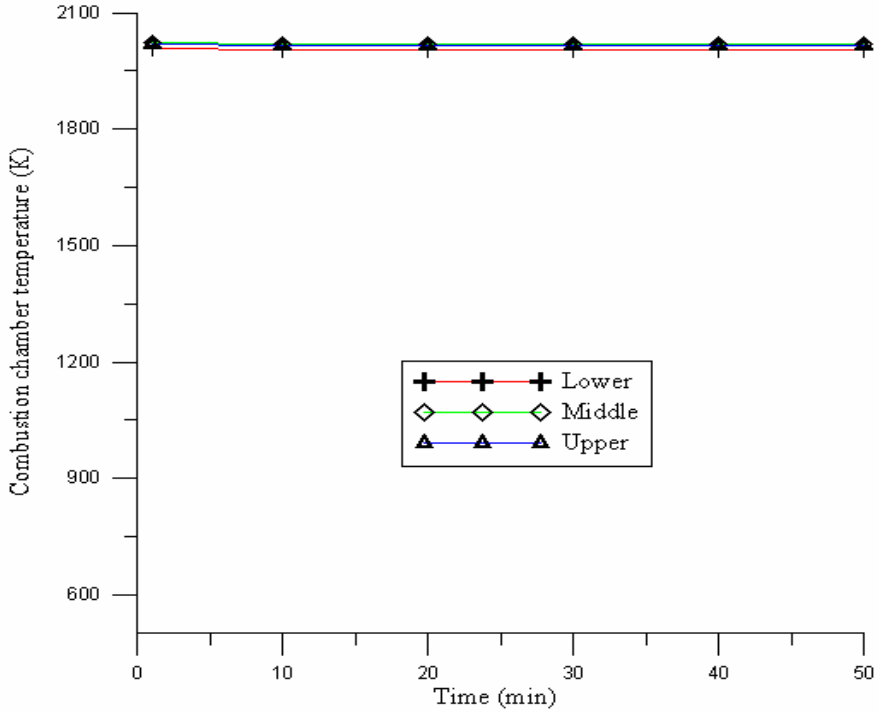

Fig. 4-47 Combustion chamber temperature during on-gas cycle (BFG = 73843.2 Nm3/h, COG = 1624.5 Nm3/h)

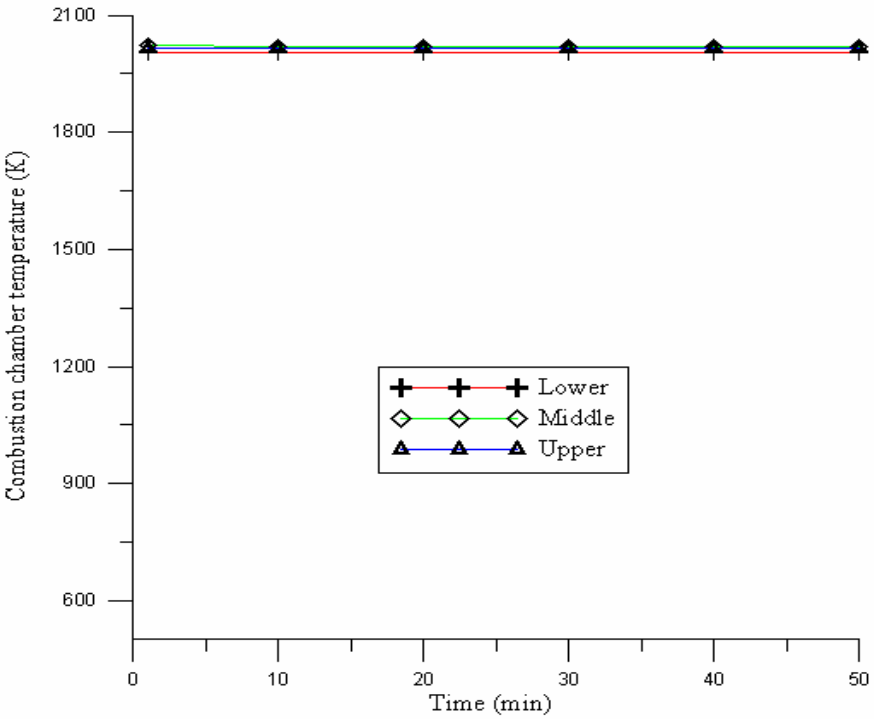

Fig. 4-48 Combustion chamber temperature during on-gas cycle (BFG = 65638.4 Nm3/h, COG = 1444 Nm3/h)

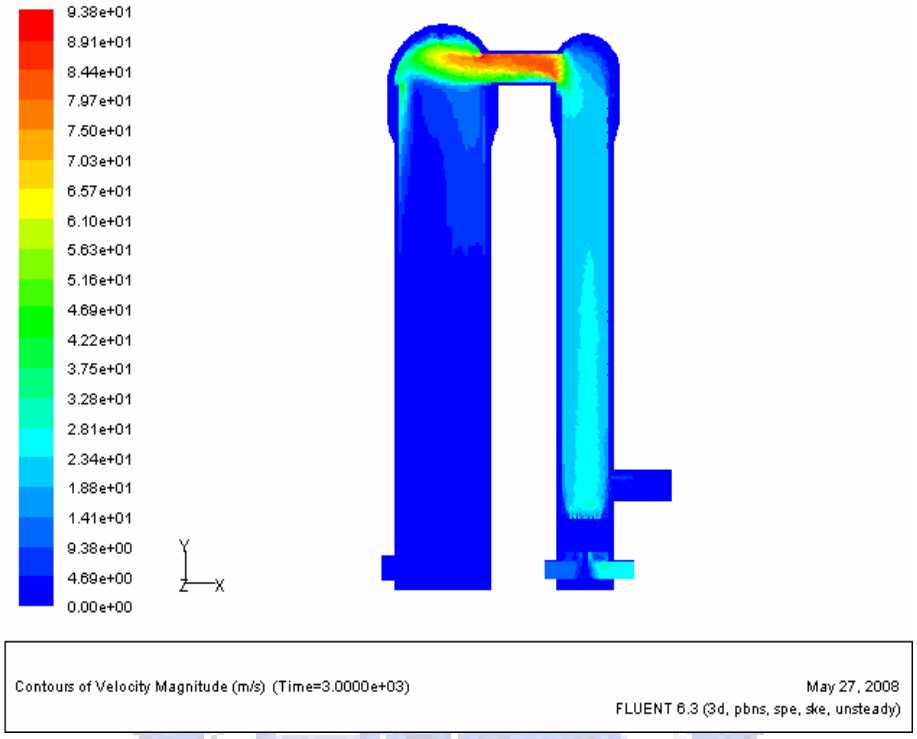

(a) Velocity distribution

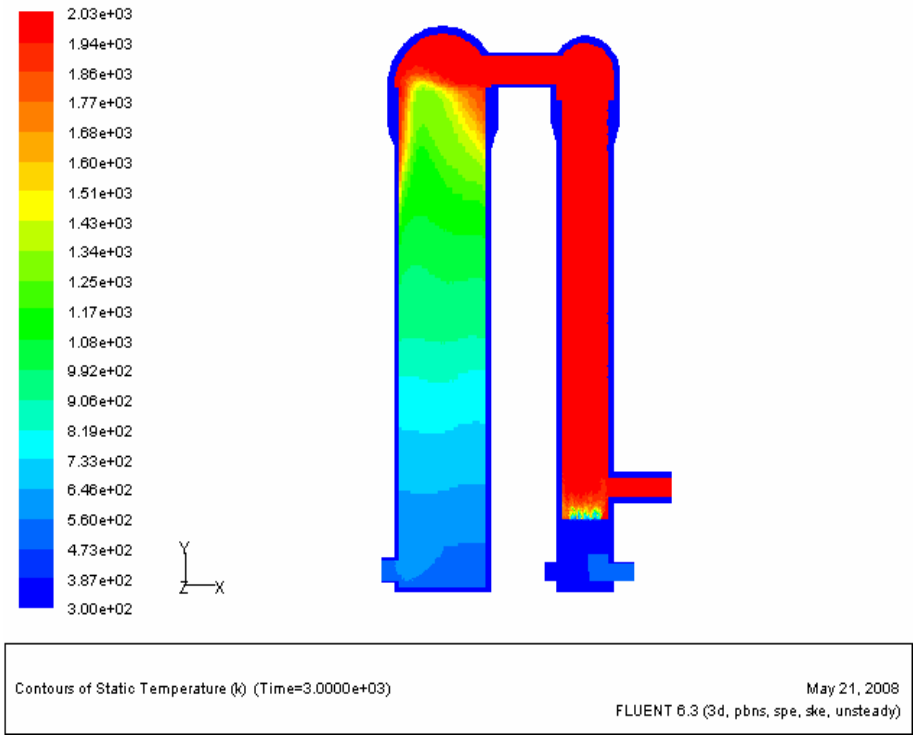

(b) Temperature distribution

Fig. 4-49 Velocity and temperature distributions in the end of on-gas cycle (Excess air ratio = 1.03)

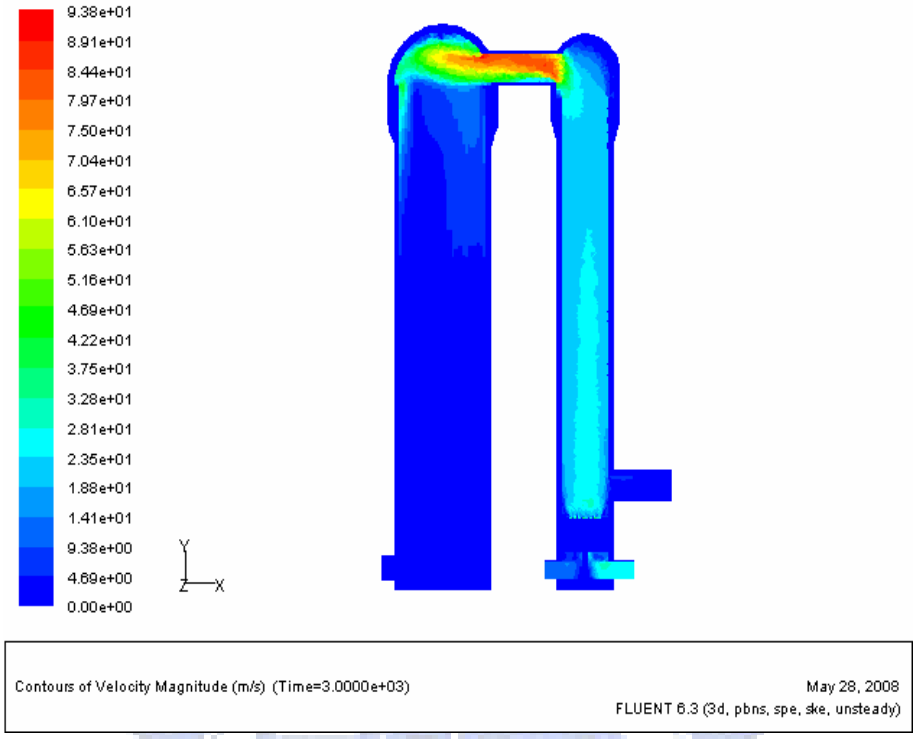

(a) Velocity distribution

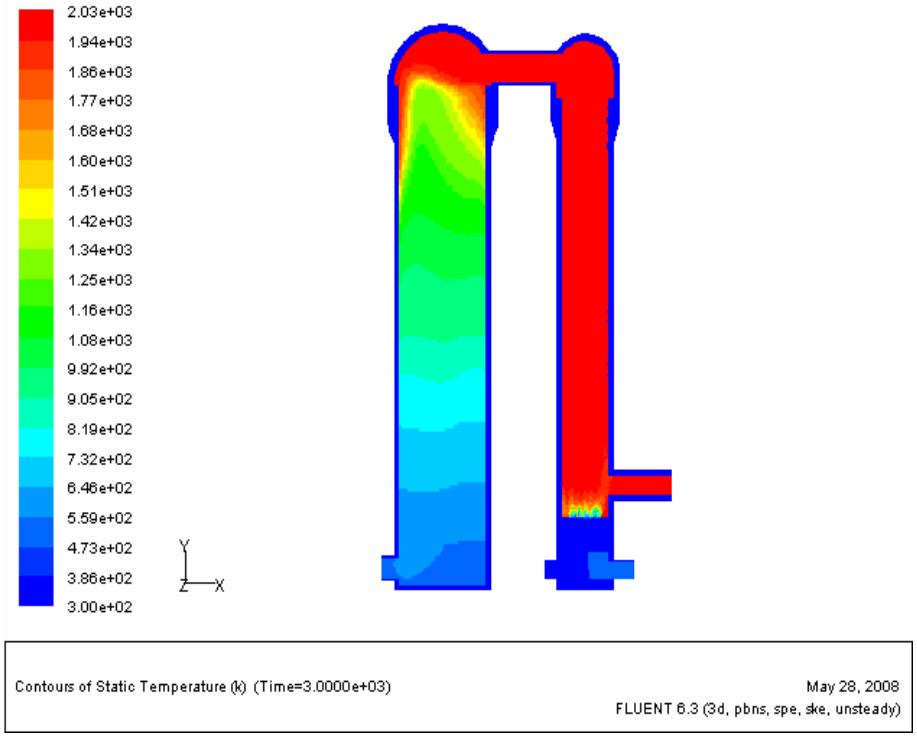

(b) Temperature distribution

Fig. 4-50 Velocity and temperature distributions in the end of on-gas cycle (Excess air ratio = 1.05)

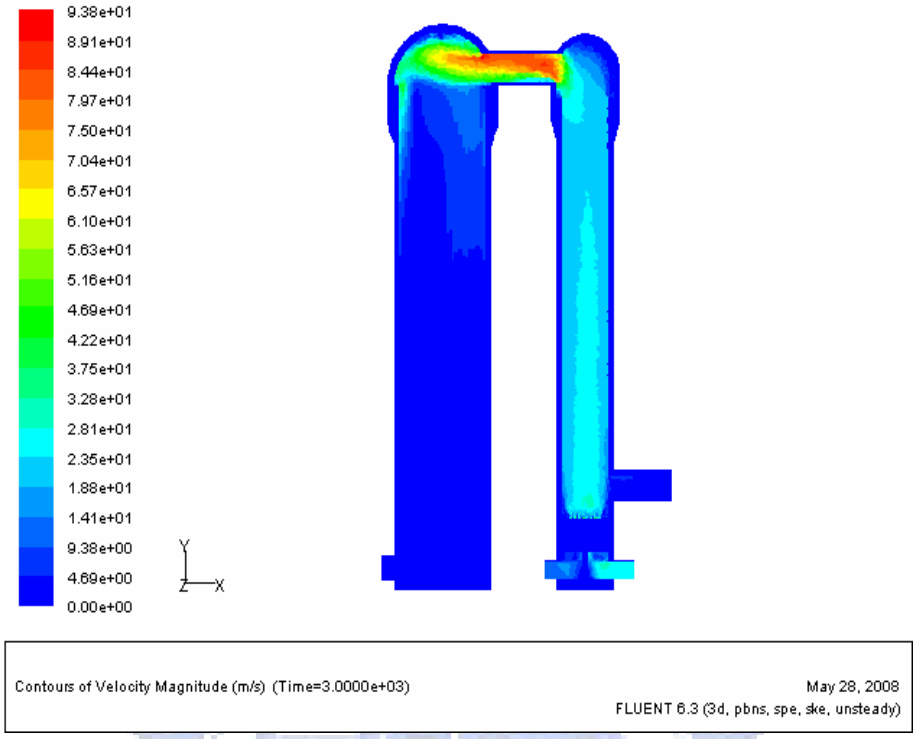

(a) Velocity distribution

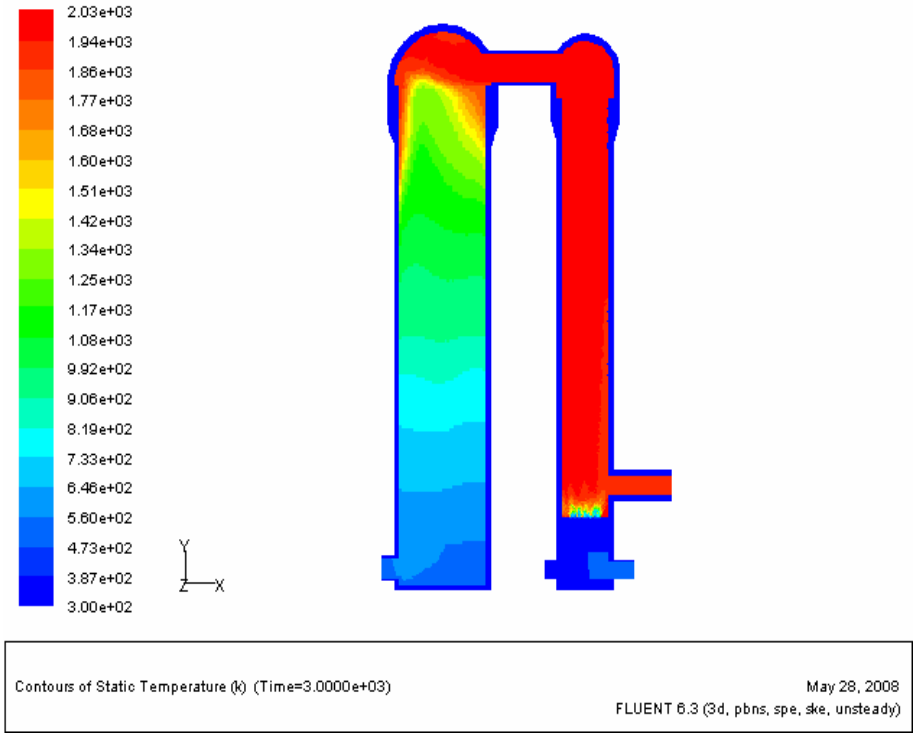

(b) Temperature distribution

Fig. 4-51 Velocity and temperature distributions in the end of on-gas cycle (Excess air ratio = 1.1)

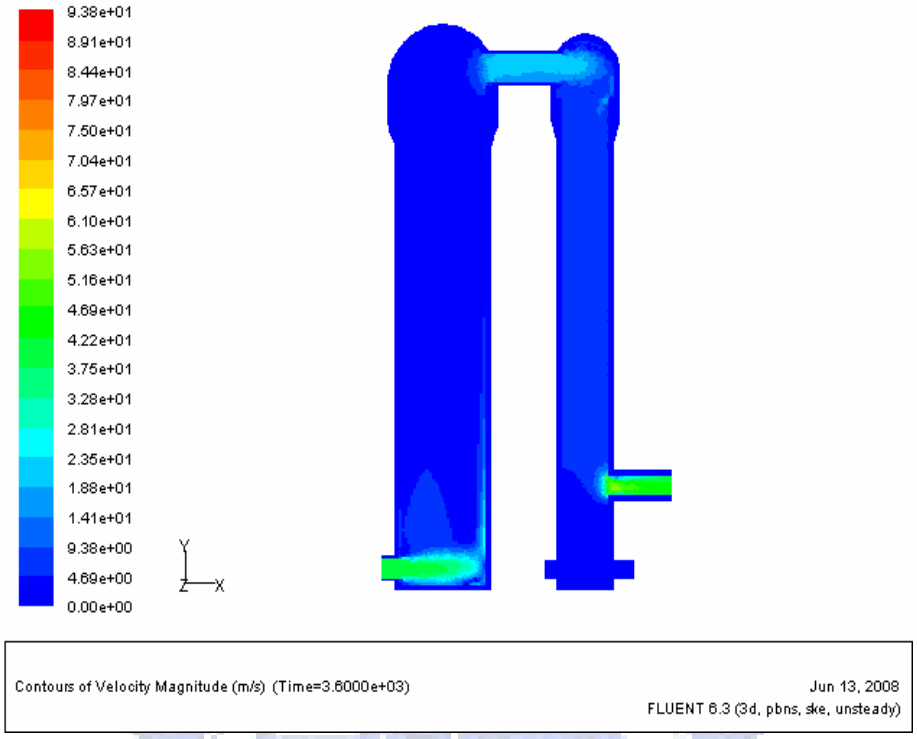

(a) Velocity distribution

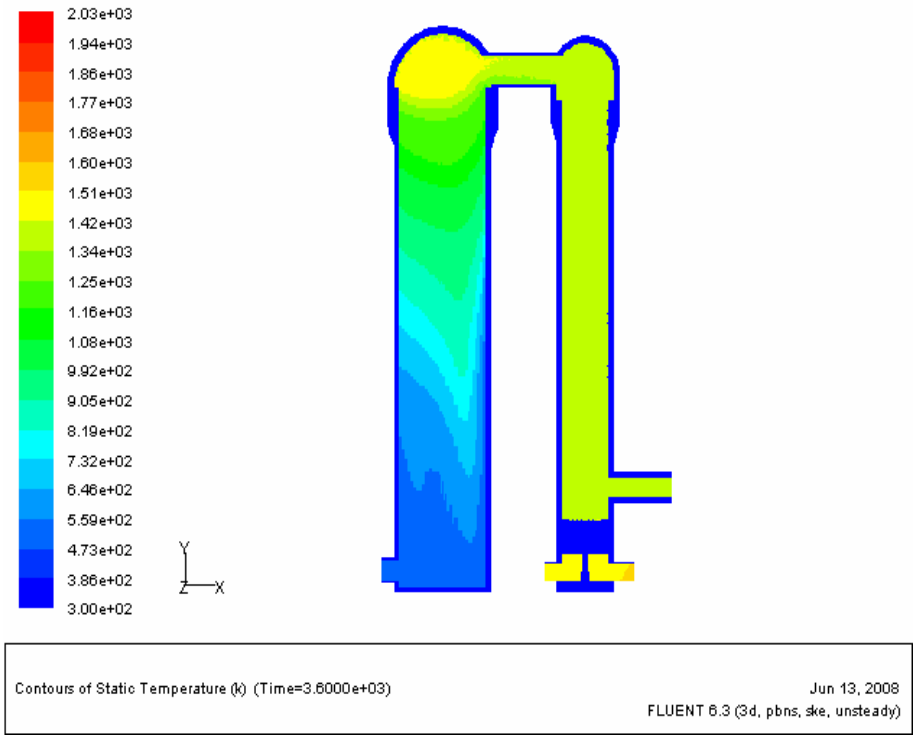

(b) Temperature distribution

Fig. 4-52 Velocity and temperature distributions in the end of on-blast cycle (Excess air ratio = 1.03)

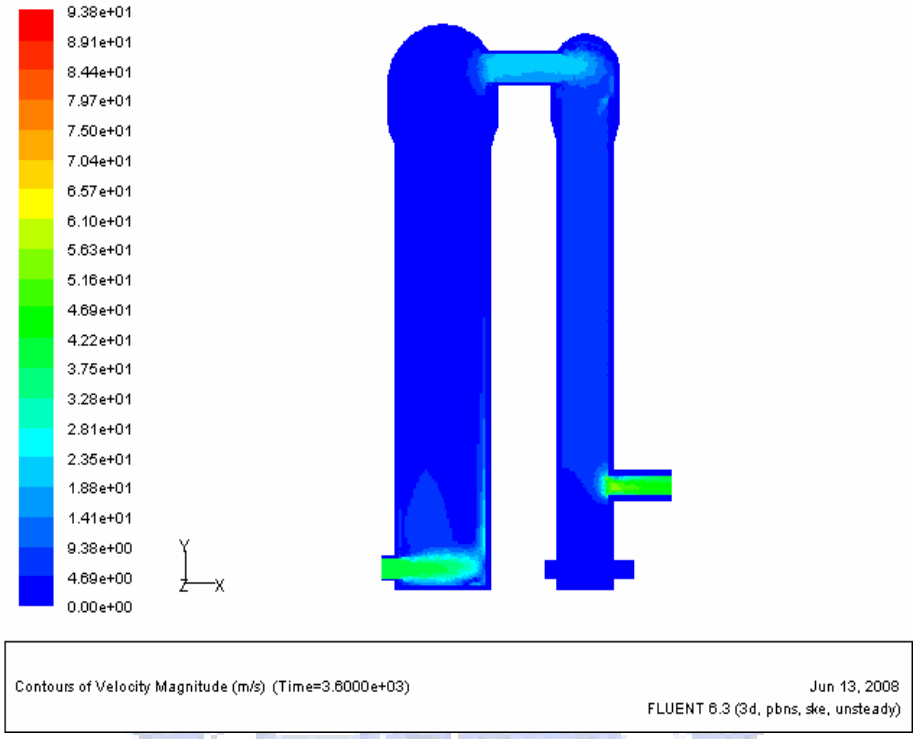

(a) Velocity distribution

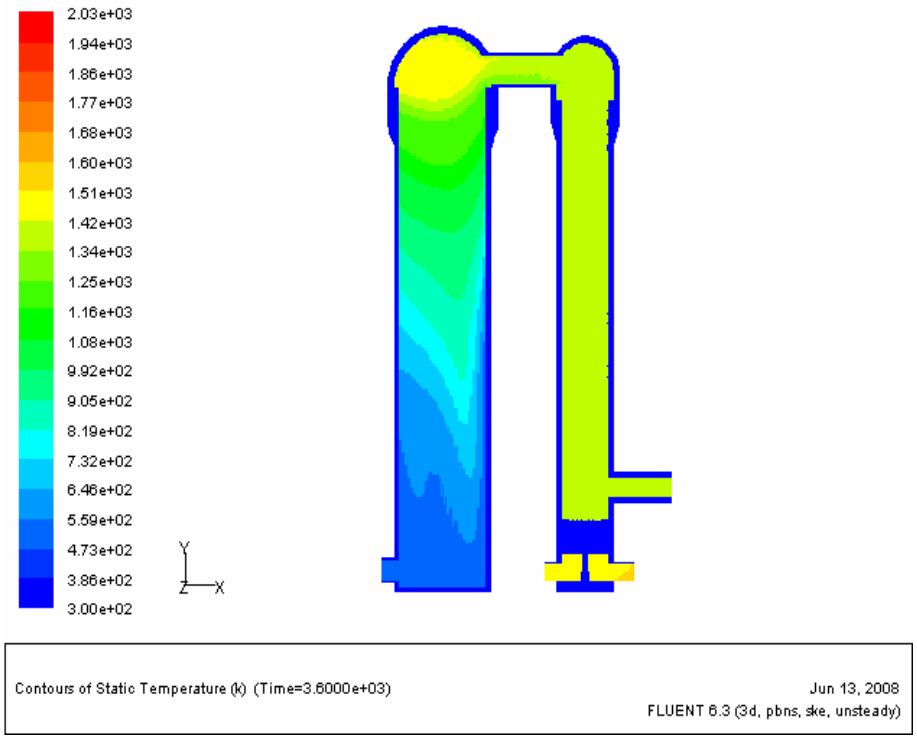

(b) Temperature distribution

Fig. 4-53 Velocity and temperature distributions in the end of on-blast cycle (Excess air ratio = 1.05)

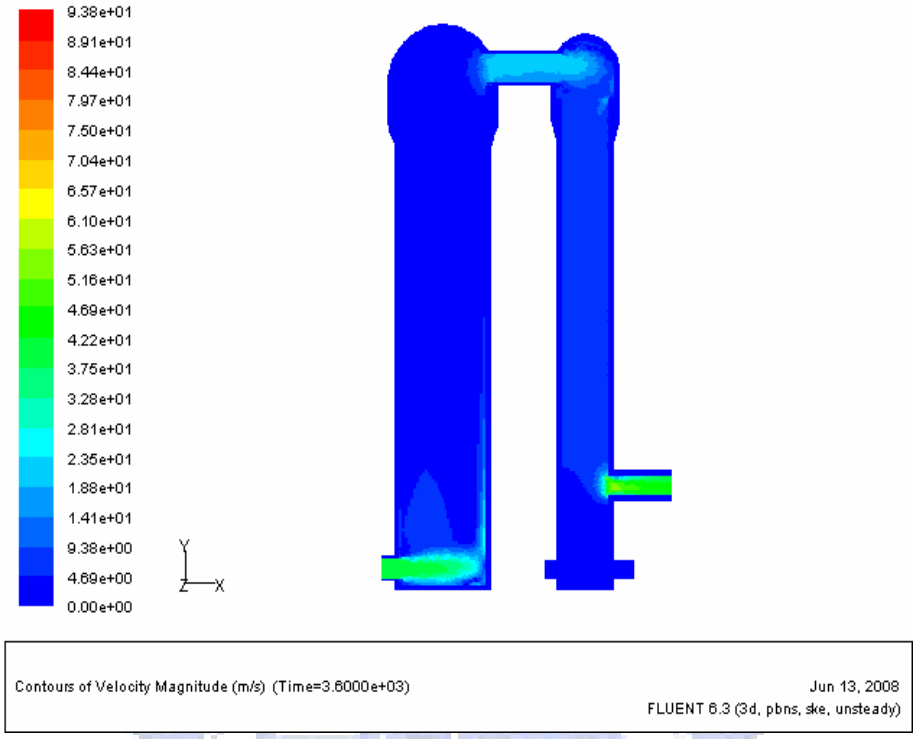

(a) Velocity distribution

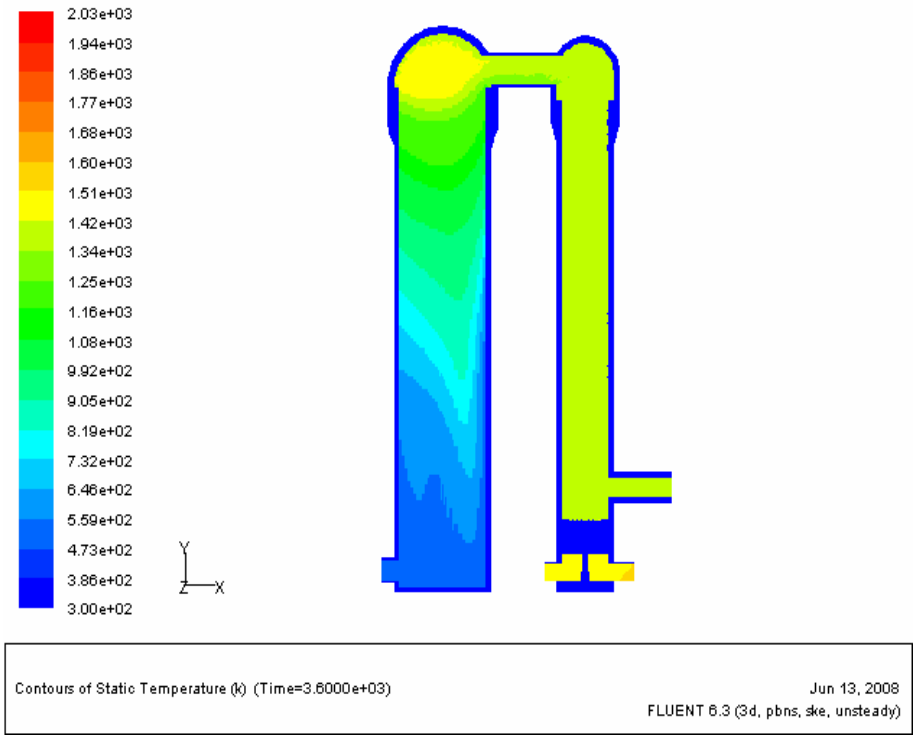

(b) Temperature distribution

Fig. 4-54 Velocity and temperature distributions in the end of on-blast cycle (Excess air ratio = 1.1)

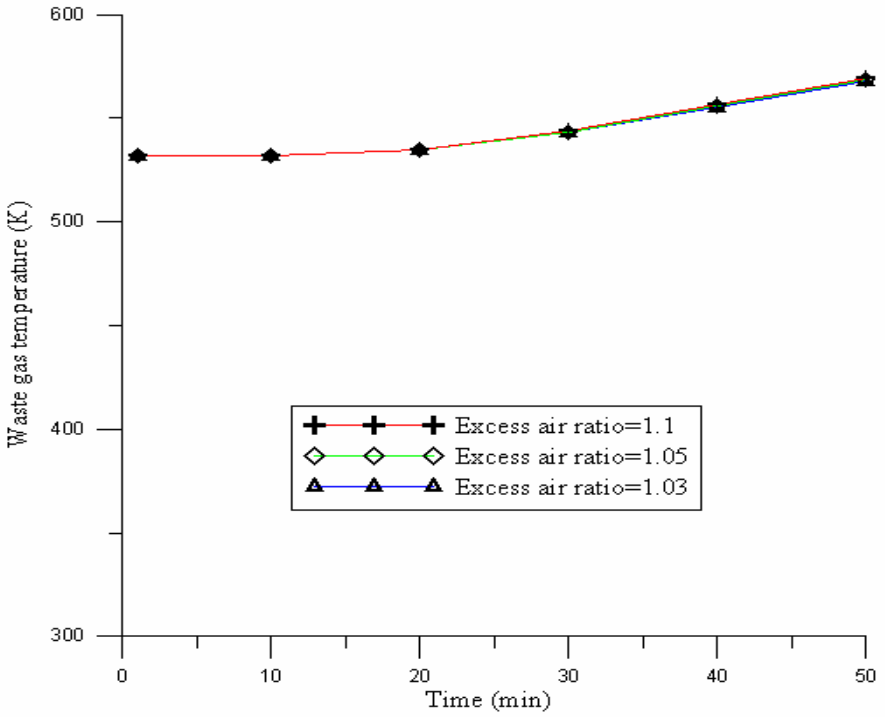

Fig. 4-55 Waste gas temperatures for different excess air ratios

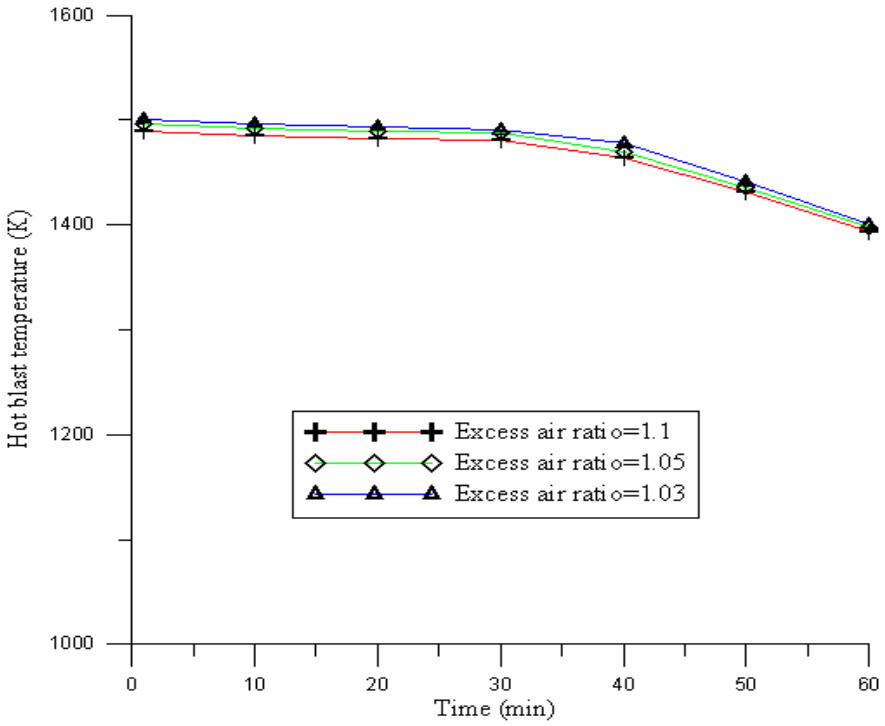

Fig. 4-56 Hot blast temperatures for different excess air ratios

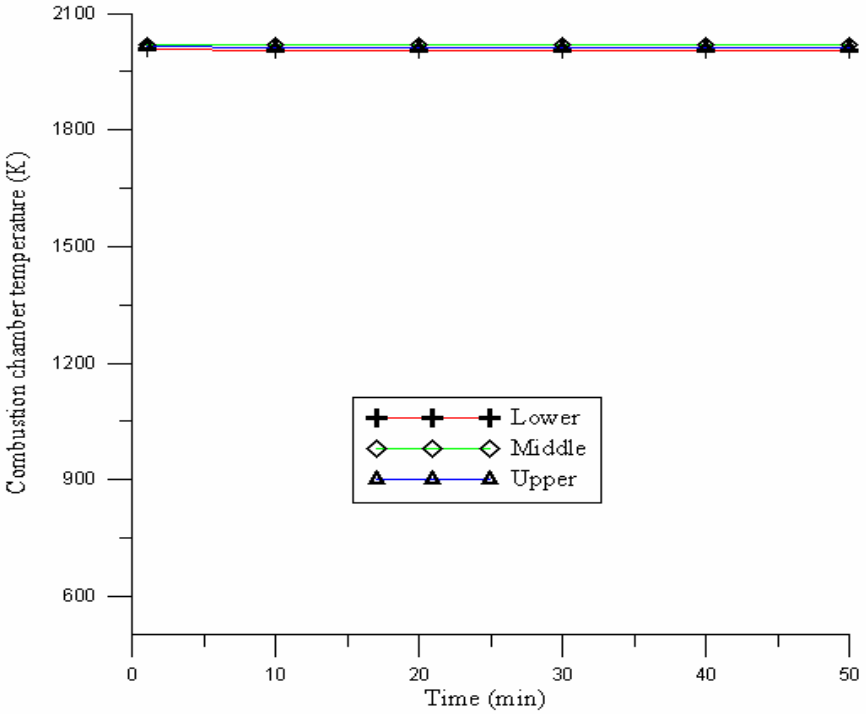

Fig. 4-57 Combustion chamber temperature during on-gas cycle (Excess air ratio = 1.03)

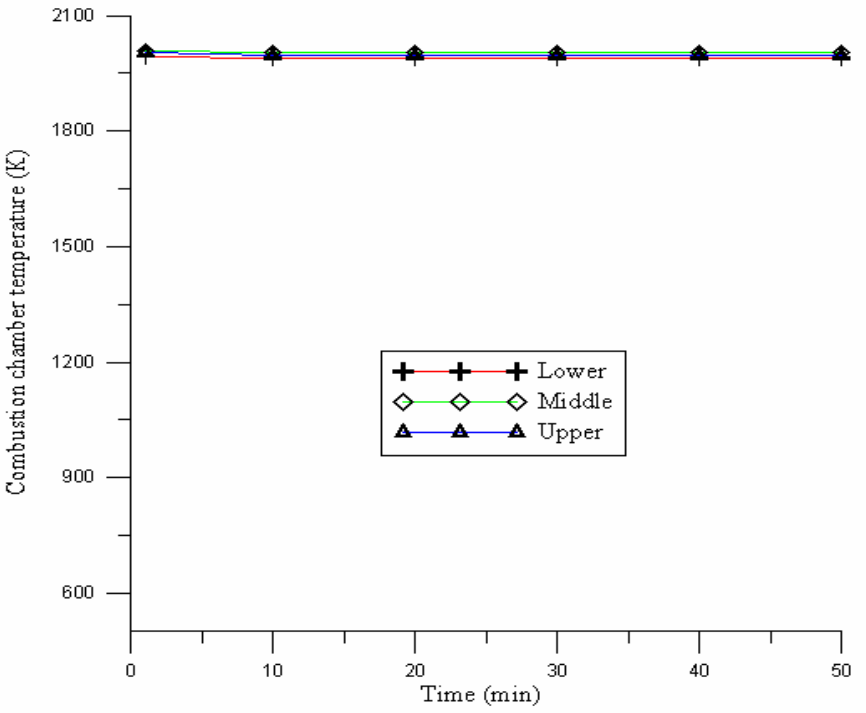

Fig 4-58 Combustion chamber temperature during on-gas cycle (Excess air ratio = 1.05)

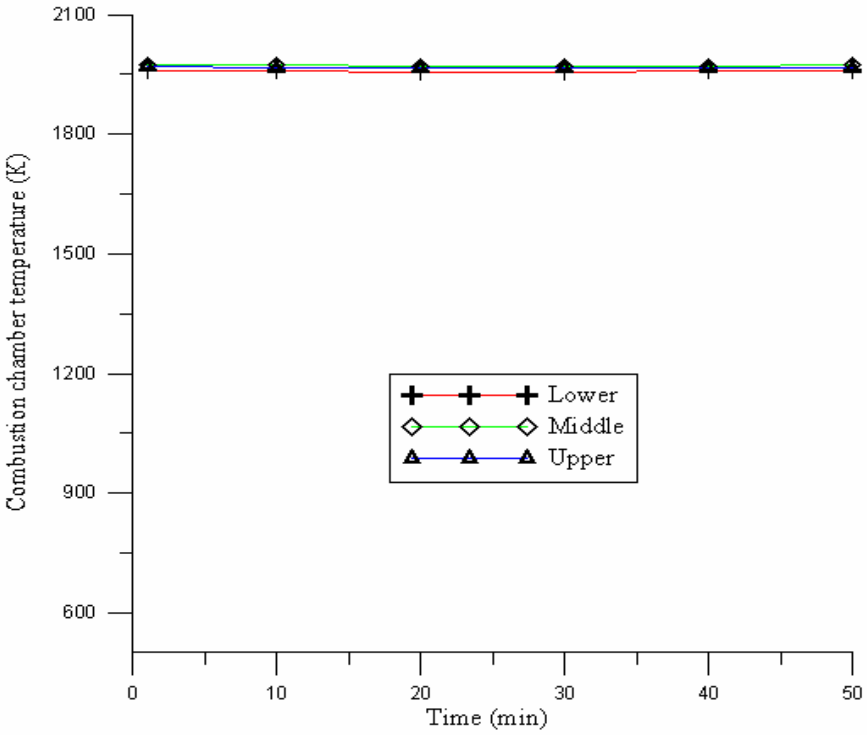

Fig 4-59 Combustion chamber temperature during on-gas cycle (Excess air ratio = 1.1)